Multifractal Analysis of Geomagnetically Induced Currents using Wavelet Leaders

Karlton Edward Wirsing

Dissertation submitted to the faculty of the Virginia Polytechnic Institute and State University in partial fulfillment of the requirements for the degree of

Doctor of Philosophy
In
Electrical Engineering

Lamine M. Mili
C. Robert Clauer
Guoqiang Yu
Vassilis Kekatos
Chang-Tien Lu

February 21, 2020
Falls Church, Virginia

Keywords: Wavelet, Fractal, Wavelet Leader, Multifractal, Geomagnetically Induced Currents

Multifractal Analysis of Geomagnetically Induced Currents

using Wavelet Leaders

Karlton Edward Wirsing

ABSTRACT

The sun is constantly emitting electrons and ions as magnetized plasma, forming the solar wind and carrying with it the sun's rotating magnetic field. The solar wind subsequently interacts with Earth's magnetosphere and the magnetospheres of other planets. Occasionally large amounts of magnetized plasma are released at one time in a Corona mass ejection (CME). When the CME interacts with Earth's magnetic field, it induces perturbations that may have a significant impact on critical infrastructure, for instance, by disturbing communication systems, and inducing currents on pipelines and electric power lines, which in turn may cause increased corrosion or blackouts, among other effects. In this dissertation, we analyze measured electrical signals provided to us by the Finnish Meteorological Institute, which were induced by geomagnetic storms on pipelines located in Finland and recorded in 2003. Specifically, we perform a wavelet leader multifractal analysis of these current signals to generate singularity spectra, and then using the bootstrapping technique, we apply statistical tests to show that these signals exhibit multifractal characteristics. We also performed surrogate testing to show that these characteristics were unique to the signal.

Multifractal Analysis of Geomagnetically Induced Currents

using Wavelet Leaders

Karlton Edward Wirsing

GENERAL AUDIENCE ABSTRACT

Earth's weather affects all of us every day. The solar space environment has weather of its own that affects us as well. Storms of a size that far exceed anything on Earth can impact Earth and affect our infrastructure. One of the most powerful phenomena that occur, called solar corona mass ejections, results when the sun ejects a large amount of plasma. This can interact with the Earth's magnetic field, which in turn induces perturbations that may have a significant impact on critical infrastructure, for instance, by disturbing communication systems, and inducing currents on pipelines and electric power lines. The currents can cause increased corrosion or blackouts, among other effects. In this dissertation, we analyze measured electrical signals provided to us by the Finnish Meteorological Institute, which were induced by geomagnetic storms on pipelines located in Finland and recorded in 2003. Specifically, we perform a statistical analysis of these current signals to decide whether they exhibit multifractal characteristics.

Acknowledgements

As with my master's thesis in Electrical Engineering, many people across the world have helped me with this project. I want to thank my advisor, Dr. Lamine Mili for his feedback and guidance over the years for this project and my committee members for their feedback as well. The data to carry out the analysis of the pipeline current was provided by Dr. Ari Viljanen from Space Research at Finnish Meteorological Institute and Dr. Antti Pulkkinen at NASA Goddard. Special thanks to Dr. Mark Everett, the reviewers at the Journal of Applied Geophysics, Dr. Jenn Gannon, and Dr. Rod Barnes for their review of the paper for publication and their helpful comments and suggestions. Space & Satellite Professionals International awarded a scholarship for one semester of research. The team at the European Space Agency made modifications that I suggested to their rank order software so that it could work with the data that I had so that I could evaluate it.

I would also like to thank my high school electronics teacher, Mr. William Tantorno, for giving me my initial training in electricity and electronics, and who has shared some of my research with his students. He also created the robotics team that I was proud to be a part of in high school that won numerous national awards.

I would like to thank my family for supporting me through all my educational endeavors, as well as for providing me with three important things growing up: an encyclopedia, a library card, and a computer. These things have enabled me to go a long way.

Finally, this dissertation is dedicated to Taz, my Russian Blue companion on this project who sat guard at the door of my computer room numerous nights while I was working on it and stole the hearts of everybody that he encountered. Sadly, due to health issues he was unable to be there when I completed it. You are missed very much. His job was taken over by two Russian Blue rescue cats, Niko and Nika.

Table of Contents

List of Figures

List of Tables

Chapter 1 Introduction

Since the nineteenth century, it has been well known that space weather has an impact on our technological systems, with its effects on the magnetosphere having been monitored since the eighteenth century. Some of these effects include disruption of the telecommunication infrastructure, induced currents on long metallic conductors such as the power grid, pipelines, and railroads, and interactions of charged particles on spacecraft orbiting Earth. Emissions from the sun consisting of a magnetized plasma flowing outwards at supersonic speeds form the solar wind, and extend past Pluto to the heliopause where they are balanced against similar interstellar fluxes. The void that the Earth's magnetic field carves out of the solar atmosphere forms the magnetosphere. Without the solar wind, the magnetosphere would closely resemble a dipole magnet. In the presence of the solar wind, the Earth's magnetosphere forms what appears to be a comet with a long magnetotail. The interactions between the solar wind and the magnetosphere are complex phenomena due to magnetic reconnection that results in exchanges of plasma and energy between the two [1]. Besides these interactions, massive storms can also occur, created by coronal mass ejections. At times a coronal mass ejection is accompanied by a solar flare. Since solar flares are optically observable from Earth, it was often assumed that this was the cause of ground disturbances. However, it is now known that coronal mass ejections are the cause of ground disturbances and solar flares are incidental [2]. They can cause significant changes in the Earth's magnetic field, which in turn generate auroras. The first known instance of space weather effecting technological systems on Earth occurred in 1859 when a solar storm hit the Earth. Its impact generated bright auroras and was correlated to Geomagnetic Induced Current (GIC) signals measured on the telegraph wires of the time [3].

While the heliopause is currently past the orbit of Pluto, that has not always been the case. As the sun orbits the Milky Way, it encounters clouds of varying density that can push the heliopause from where it is now to inside Earth's orbit. At that point interstellar activity has a much greater influence on space weather than it currently does in addition to impacting Earth's atmospheric chemistry. While the solar wind keeps out charged interstellar plasma, neutral hydrogen and helium from interstellar space flows into the inner heliosphere, where it interacts

with the solar wind to create secondary ions. At times during the sun's orbit around the Milky Way, when interstellar neutral hydrogen is dense enough, it can flow into Earth's atmosphere and destroys the ozone in the mesosphere. Since ozone is a greenhouse gas, one hypothesis is that this has been the source of several ice ages in Earth's history. This shows that space weather, and even Earth's weather and climate, can be influenced from phenomena taking place outside the solar system [4].

The interactions of the Earth's magnetosphere with the solar wind induce or disturb various types of currents in the ionosphere and the magnetosphere, among these the ring current, the equatorial electrojet current, and the auroral electrojet current [5]. The ring current around the equator, which consists of a ring of positively charged ions that circulate from east to west and electrons that circulate from west to east, is present in the magnetosphere at a distance of 2 to 5 Earth radii. On the other hand, the equatorial and auroral electrojet currents are present in the ionosphere at an altitude between 100 and 150 km above the surface. In turn, these phenomena induce GIC signals on systems on the ground that consist of long conductors, such as pipelines, power lines, and railroads. On October 10, 2019, NASA launched the Ionospheric Connection Explorer (ICON) spacecraft to explore changes in the ionosphere and its connections to the atmosphere [6]. This and other spacecraft and ground-based observations will increase our knowledge of the Earth-Sun system.

GIC can have impacts on power systems, pipelines, and railroads, all three of which involve long networks of conductors that act as antennas that receive changes in Earth's magnetic field. The impact on power systems are that it pushes the transformer into its saturated region for half of its cycle, which can cause thermal failure. GIC causes corrosion in steel pipelines and can interfere with railroad signals.

There are several indices that measure changes in Earth's magnetic field, which are used to monitor the effects of space weather. The overall measure of the impact of the solar wind on the magnetosphere is given by the K_p index [7]. This index varies on a scale of 0-9 where 0 means calm and 9 means severe geomagnetic storm. This dissertation will use the mean of this index over the course of a day to give a rough indication of the overall state of the magnetosphere. Two others are the auroral electrojet index, which is measured at high latitudes in the auroral region in the northern hemisphere, and the Disturbance Storm Time Index (Dst), which is measured at low latitudes near the equator and that provides an overall measure of the

ring current. The aa index consists of measurements from two observatories on opposites sides of the Earth. Measurements have been kept since 1868, and thus provides a long term measure of the magnetosphere.

The solar wind has multifractal characteristics as reported in [8]. A monofractal object consists of the replication of one of its features across many scales, leading to a self-similarity characteristic. This object consists of either multiple copies or multiple statistical copies of the same feature. Unlike the dimension of most of the usual objects that we are familiar with, the dimension of a fractal is typically not an integer. Many natural phenomena have fractal characteristics. When an object or a signal has a fractal dimension that is not constant over all its range, it is multifractal. In that case, its dimension is a spectrum of values, which has prompted many authors to refer to it as "fractals intertwined with fractals."

Typically, a fractal is a self-similar object since its characteristics are replicated across several scales either exactly or statistically. It is also a function that is irregular in some sense. This excludes trivial self-similarity such as a line made of straight lines. Fractals have had a long history in the geophysical community, particular related to the field of self-organized criticality (SOC) [9].

Fractal signals are highly irregular, which cannot be analyzed using conventional signal processing techniques. They are best analyzed using the wavelet transform, which was first developed by Alfred Haar [10] as an alternative to the Fourier transform [11, 12]. Both transforms decompose a signal into a sum of basis functions. However, unlike the basis functions of the Fourier transform that are defined only in the frequency domain, those of the wavelet transform are defined in both the time and the frequency domain, which enables the retrieval of localized information about the signal. Wavelet transforms have two main advantages over the Fourier transform when applied to fractal signals [13, 14]. Their first advantage stems from their ability to analyze signals that exhibit a time-scale characteristic over a large portion of their range. Their second advantage stems from the numerical stability of the estimated coefficients, which results from the localization of the phase transitions; the latter are spread throughout the Fourier power spectrum. The continuous wavelet transform produces a number of redundant data; the reason is that the transformed values of two different scales that differ slightly are highly correlated. By contrast, the discrete wavelet transform is invertible and uses only discrete values for the scales, typically a power of 2, which allows applications in noise removal and

compression. Daubechies [15-18] expanded the first wavelet transform proposed by Haar by creating a compact transform with minimal overlap of information, known as the Daubechies wavelet family.

The wavelet transform has been used to analyze space weather index data using the wavelet transform and general analysis [19], the Wavelet Transform Modulus Maxima (WTMM) [20-22] and the wavelet leader method [23]. As shown in [24-26], wavelet leaders based on the discrete wavelet transform are powerful tools for revealing multifractal characteristics of signals. Along this line, Wendy and Abry [27] propose to use wavelet leaders along with bootstrapping techniques to estimate confidence intervals via Monte Carlo resampling with replacement [28] of a single instance of a signal and then, by applying hypothesis testing, to decide whether the signal is regular, monofractal, or multifractal. This dissertation will expand on that analysis by also using surrogate data testing to show that the multifractal characteristics are not dependent on the power spectrum of the signal [29] as well as automated range selection.

Weather forecasting has progressed a lot in the last 100 years. Richardson [30] wrote the seminal work “Weather Prediction by Numerical Processes” in 1922 that became the basis for modeling the weather using fluid dynamic equations, which have helped to save lives and prevent property damage. One key problem is that it was found that the accuracy of weather forecasting is sensitive to initial conditions. Specifically, the forecasting errors double every 5 days, limiting the reliability of the forecast. Space weather forecasting has similar goals to weather forecasting. However, the problems are that the processes are more complex and not as well understood, and they occur over much longer distances with much less sensor data. Analyzing the available data from many different locations in numerous different ways including multifractal analysis can help us to understand these processes and how they interact with each other, thereby contributing to advance space weather forecasting. Current algorithms aim at forecasting the properties of the ionosphere, specifically the total electron count, however, magnetospheric properties also need to be analyzed and forecast as well [31].

In this dissertation, we analyze actual GIC signals induced on pipelines, which were recorded in 2003 in Finland. A preliminary fractal analysis of GIC signals were carried out by Pulkin et al. [32, 33] using the S transform. This analysis has prompted us to hypothesize that these signals are multifractal due to the turbulent nature of the interaction of the solar wind with the Earth’s magnetosphere and the secondary interactions of elements of the Earth’s

magnetosphere with the pipelines. To test this hypothesis, we perform a wavelet leader multifractal analysis of these GIC signals and generate singularity spectra, and then using the bootstrapping technique, we apply statistical tests to show that they exhibit multifractal characteristics. Multifractal modelling helps provide signal analysis and information that traditional methods can miss. The uses of this information include information of the dynamics of the magnetosphere, space weather forecasting, impact on critical infrastructure, and impact on the disturbance of communications.

The wavelet leader software was extensively modified to do bulk analysis and to do simultaneous analysis of several parameters. Surrogate analysis was added to the software as describe in Section 4.5 and automated range analysis was added as describe in Section 4.6. The software was also modified to save an entire report of all parameters for each individual dataset analyzed, as well as to put all the parameters in a table so that trends can be analyzed. This includes statistical hypothesis testing on all ranges analyzed so that longer ranges and adjacent ranges can be analyzed as well. The work resulted in the publication of a paper in the Journal of Applied Geophysics [34].

The dissertation is organized as follows. Chapter 2 provides details about space weather, Chapter 3 discusses fractals and multifractals, and Chapter 4 provides details about the methods used in this dissertation. The first part of Chapter 5 describes some numerical results of six GIC signals in Finland recorded in 2003 taken at various mean K_p index values, including three corresponding to the Halloween storm. The second part of Chapter 5 has the results from wavelet leader analysis on each three-hour interval from 2003 correlated to individual K_p index values so that we can see how the multifractal characteristics change as the K_p index value changes. Finally, some conclusions and future work are provided in Chapter 6.

Chapter 2 Space Weather

The definition of weather is as follows: “The state of the atmosphere at a given time and place with respect to variables such as temperature, humidity and wind velocity” [35]. We are most familiar with terrestrial weather that comes from fluid dynamics of the Earth’s atmosphere and the heat from the sun. But as we shall see, the sun’s atmosphere extends throughout the solar system and changes with time, which has an effect on Earth; this is the reason why it is a field of study. The study of space weather has started in the nineteenth century [36], which was initiated in 1847 by John Herschel [37] with the use of the term solar meteorology to refer to observed changes in the sun. Three years later, John Philips [38] coined the term magnetic weather to refer to the changes in the Earth’s magnetic field. The term space weather first appeared in 1957, but it referred to the study of interstellar medium that exists between stars on the scales beyond that of the solar system [39]. In 1958, Eugene Parker [40] proposed the term solar wind to refer to the constant stream of particles that are emitted from the sun. With the launch of the Explorer I probe, the term space weather began to be used in reference to the radiation belts surrounding Earth and their interaction with the sun [41]. The formal definition of space weather was given by Robinson and Behnke [42] as “Space weather refers to conditions on the sun and in the solar wind, magnetosphere, ionosphere, and thermosphere that can influence the performance and reliability of space-borne and ground-based technological systems and can endanger human life or health. Adverse conditions in the space environment can cause disruption of satellite operations, communications, navigation, and electric power distribution grids, leading to a variety of socioeconomic losses.”

In 1964, a space weather bureau was proposed to predict hazards to the astronauts for the upcoming lunar missions [43]. Space weather is a particular concern for manned deep space missions since these are outside of the protection of the Earth’s atmosphere and magnetosphere, which could expose the astronauts to lethal levels of radiation. The Apollo lunar missions occurred during the solar minimum of the 11-year sunspot cycle. However, in August of 1972, the sun had a period of 10 years of increased activity that involved numerous solar flares and a CME that caused a solar proton event and magnetic storm on Earth. This was between the

missions of Apollo 16 (April 16, 1972 – April 27, 1972) and Apollo 17 (December 7, 1972 – December 19, 1972). Had the astronauts been on the moon during this event, NASA would have advised them to take shelter in a crater to try to provide some protection from the radiation [44]; however the amount of radiation that they would have been exposed to would have caused severe radiation sickness and possible death.

2.1 Solar Atmosphere

The solar atmosphere extends from the surface of the sun to beyond the orbit of Pluto and consists of ions and electrons ejected from the sun in a radial pattern due to the sun's rotation. The properties of the solar wind at a distance of 1 AU are given in Table 2-1. At 30 pico Pascals, the solar atmosphere pressure is 2.96 10^{-13} that of Earth at sea level. Compared to the speed of sound in the medium and the flow speed, the speed of the solar wind is Mach 7.5, which is hypersonic. When the solar wind collides with the Earth's magnetic field, it slows to subsonic speeds, which creates shockwaves.

Table 2-1: Solar Atmosphere Properties [45]

Solar Wind near the Orbit of the Earth (1 AU)		Derived Properties	
Proton density	6.6 cm^{-3}	Gas pressure	30 pPa
Electron density	7.1 cm^{-3}	Sound speed	60 $km \cdot s^{-1}$
He^{2+} density	0.25 cm^{-3}	Magnetic pressure	19 pPa
Flow speed (nearly radial)	450 $km \cdot s^{-1}$	Alfvén speed	40 $km \cdot s^{-1}$
Proton temperature	$1.2 \cdot 10^5$ K	Proton gyroradius	80 km
Electron temperature	$1.4 \cdot 10^5$ K	Proton-proton collision time	$4 \cdot 10^6$ s
Magnetic field (induction)	$7 \cdot 10^{-9}$ telsa (T)	Electron-electron collision time	$3 \cdot 10^5$ s
		Time for wind to flow from corona to 1 AU	~4 days = $3.5 \cdot 10^5$ s

2.2 Sunspots

Sunspots are dark areas on the surface of the sun that have been known since at least the 4th century BC. Galileo noted them when he first observed the sun with a telescope. Sunspots can occur in pairs or individually. The structure of a sunspot consists of a dark umbra at the center surrounded by a lighter penumbra. This is due to the fact that the magnetic flux tube that creates a sunspot reduces convection in the photosphere around it, which makes it cooler than the surrounding area, namely 4500 K for the umbra, 5500 K for the penumbra, and 5800 K for the surrounding photosphere [45, 46].

Heinrich Schwabe [47] first noticed a cycle in the number of sunspots of about 10 years, which was later found out to actually be 11 years. Edward Sabine [48] noticed that the magnetic disturbances seemed to occur in an 11 year cycle, which was later correlated to the sunspot cycle. When the number of sunspots is at a minimum in the cycle, this is called solar minimum, and when the number of sunspots is at a maximum, this is called solar maximum. Solar cycles are numbered starting from 1755-1766 solar cycle, which is solar cycle 1. The current cycle is 24 and started on January 4, 2008 [49]. The monthly mean sunspot numbers from January 1749 to present are shown in Figure 2-1. As we are nearing a solar minimum, solar cycle 25 will start in a few years. If we take the Fourier transform of the mean sunspot numbers and filter it with a 6 order Kaiser window, we see a large periodic spike around the 11-year mark as shown in Figure 2-2.

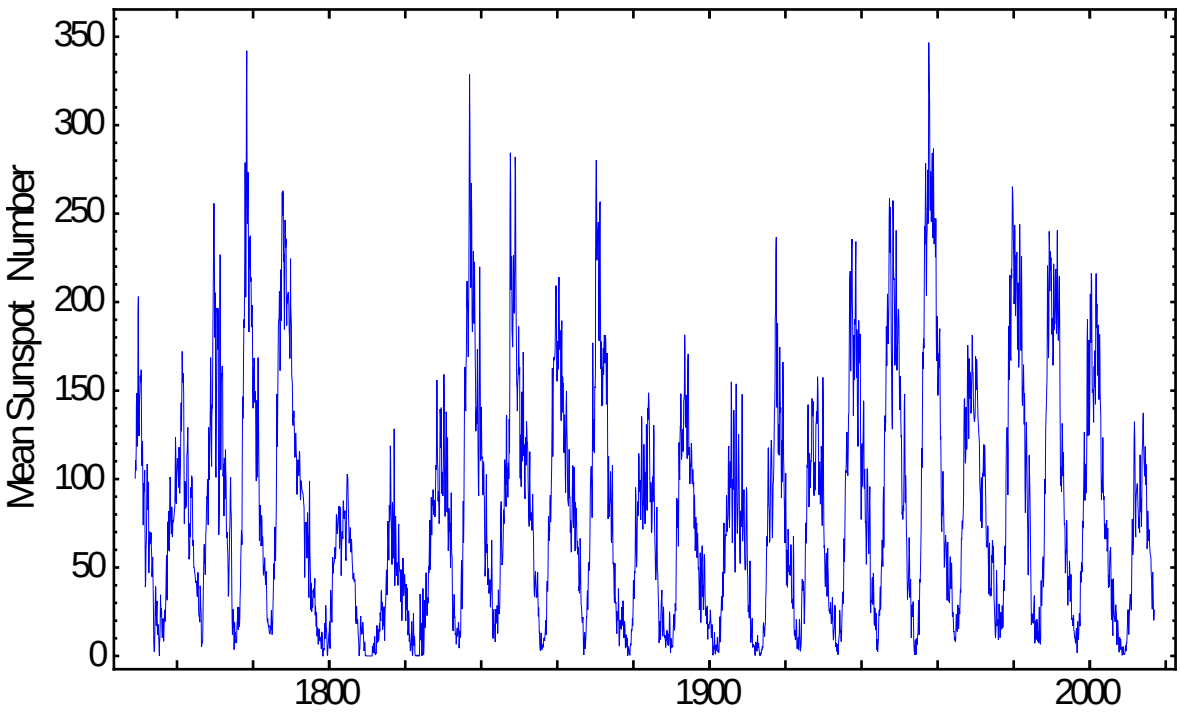

Figure 2-1: Mean sunspot numbers from 1749 to 2017

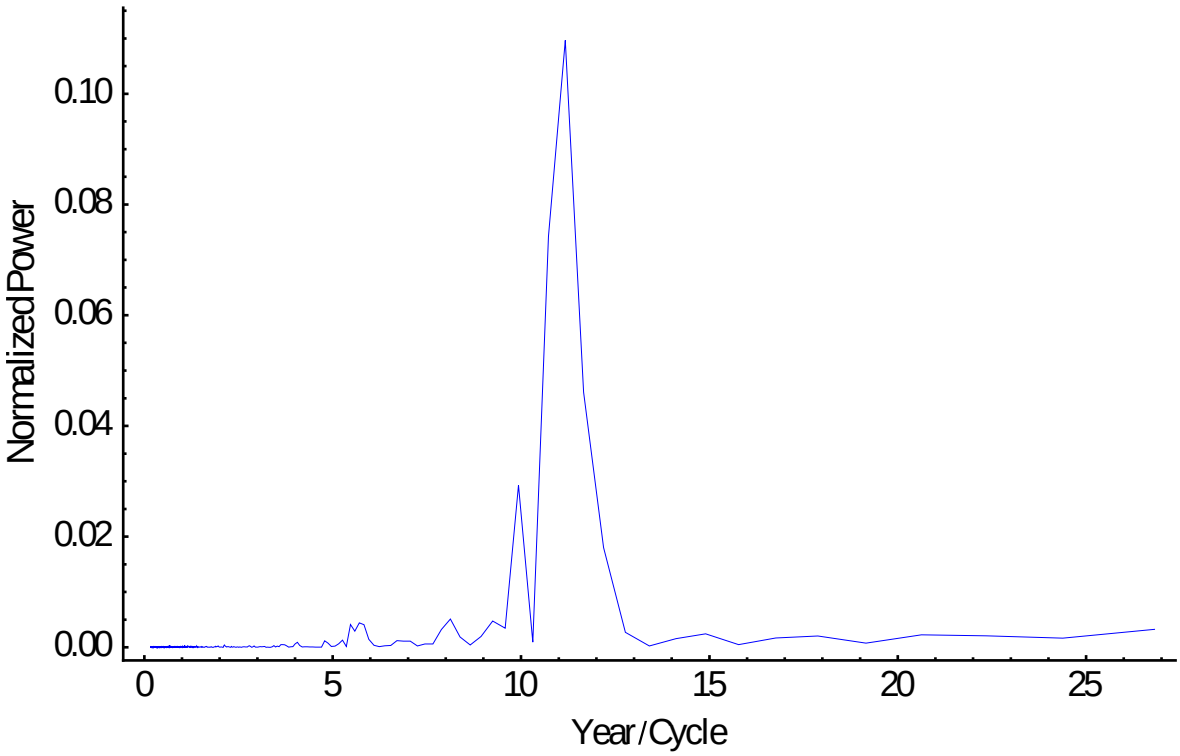

Figure 2-2: Fourier power spectrum analysis of mean sunspot number filtered with a 6 element Kaiser window. Y axis is normalized to fractions of the DC power.

2.3 Extreme Solar Events

The two main solar phenomena that cause significant space weather events are solar flares and corona mass ejections (CME). The first involves large releases of electromagnetic energy and the second causes large amounts of charged particles to be sent into the solar system, where it might collide with the Earth's magnetosphere. These frequently occur together, but can occur separately as well.

Corona mass ejections are defined as "a large eruption of plasma and magnetic field from the Sun" [50]. The average width of a CME is 47° and the median is 43° in solar longitude [51], and spans tens of degrees of latitude as well. The 5% and 95% percentile of the speeds of a CME are 35 and 911 km/s respectively with an average speed of 349 km/s and a median speed of 285 km/s [52]. The energy released from a CME ranges from 10^{30} to 10^{32} erg (10^{15} to 10^{17} Megajoules), with an amount of mass released ranging from 10^{15} to 10^{16} grams [53]. The impact of a CME on the Earth changes the magnetosphere, which changes the various current systems and can induce GIC in terrestrial systems.

Solar flares are different in that their release of energy takes the form of electromagnetic radiation and travels at the speed of light, reaching Earth in 8 minutes [54]. The impact of a flare on Earth is primarily on the ionosphere, impacting radio communications.

It was originally thought that solar flares caused CMEs, but that has turned out not to be the case [2]. While flares can occur with a CME, they are of a secondary phenomena in relation to space weather in that the primary driver of geomagnetic storms are a CME impacting with Earth's magnetosphere [55]. The frequency of solar flares and corona mass ejections vary by the 11-year sunspot cycle. CME's are observed at a frequency of about one a week at solar minimum and an average of 2 to 3 a day at solar maximum [56].

2.4 Earth's Magnetosphere and Ionosphere

The Earth's magnetic field interacts with the charged solar atmosphere to create a cavity around Earth called the magnetosphere. This provides protection from solar wind and creates various current systems and radiation belts. When a solar storm collides with the magnetosphere, this creates changes in these current systems and those changes then induce changes in the

ground. Therefore, most of space weather effects on Earth go through multiple interactions to be observed from the ground that increases complexity of the system.

One of the largest current systems created by this interaction is the equatorial ring current. This consists of positively charged ions that drift westward and electrons that drift eastward. The positive portion of the ring current primarily consists of H^+ and O^+ ions. The H^+ ions come from the solar wind and the ionosphere and the O^+ ions come from the ionosphere [57]. During a geomagnetic storm, the concentration of O^+ ions from the ionosphere in the ring current often increases. As the ring current gets stronger, it weakens Earth's magnetic field.

The ionosphere is formed when radiation from the sun or cosmic sources bombards Earth's neutral atmosphere, creating positively charged ions and free electrons [45]. This layer starts in the mesosphere, goes through the thermosphere, and ends at the beginning of the exosphere. Because it is primarily formed from solar radiation, the structure of it changes from day to night and during solar eclipses. It is divided into 4 layers during the day (F_1, F_2, E, and D). At night, the D layer disappears and the F_1 and F_2 layers combine into a single F layer. The ionosphere is electrically conducting and has various current systems such as the auroral and the equatorial electrojets [58-60]. The ionosphere also reflects shortwave radio waves, making it useful for radio communications [61].

2.5 Indices of Space Weather

There are several indices that can measure changes in the Earth magnetic field, which are used to monitor the effects of space weather. They are the K_p index which provides an overall state of the magnetosphere, the auroral electrojet index, which is measured at high latitudes in the auroral region in the northern hemisphere, the Disturbance Storm Time (Dst) index, which is measured at low latitudes near the equator and provides an overall measure of the ring current, and the amplitude antipodal (aa) index which provides measurements since 1868. The indices are calculated from magnetic observatories around the world that measure changes in the horizontal component of Earth's magnetic field. The locations of these observatories as of 2020 are shown in Figure 2-3.

Figure 2-3: Magnetic Observatory Locations. Green Auroral Indices, Blue K_p Index, Red Dst Index, Black aa and K_p Index. Made with Google Maps 2020 [62].

2.5.1 Dst Index

The Dst index is produced from four observatories, Hermanus, South Africa, Kakioka, Japan, Honolulu, Hawaii, and San Juan, Puerto Rico [63]. It is in units of nanoteslas (nT). Negative Dst values indicate a weakening of the Earth's magnetic field while positive values indicate a strengthening, a property that is used to probe changes in the ring current in the magnetosphere. When a magnetic storm hits, the magnetic field typically weakens and recovers. Details about how the Dst index is calculated are given in [64]. It has been the subject of fractal and multifractal research [23, 65]. The daily mean value for the Dst index for 2003 is shown in Figure 2-4. In it you can see the major disturbances, including the Halloween storm.

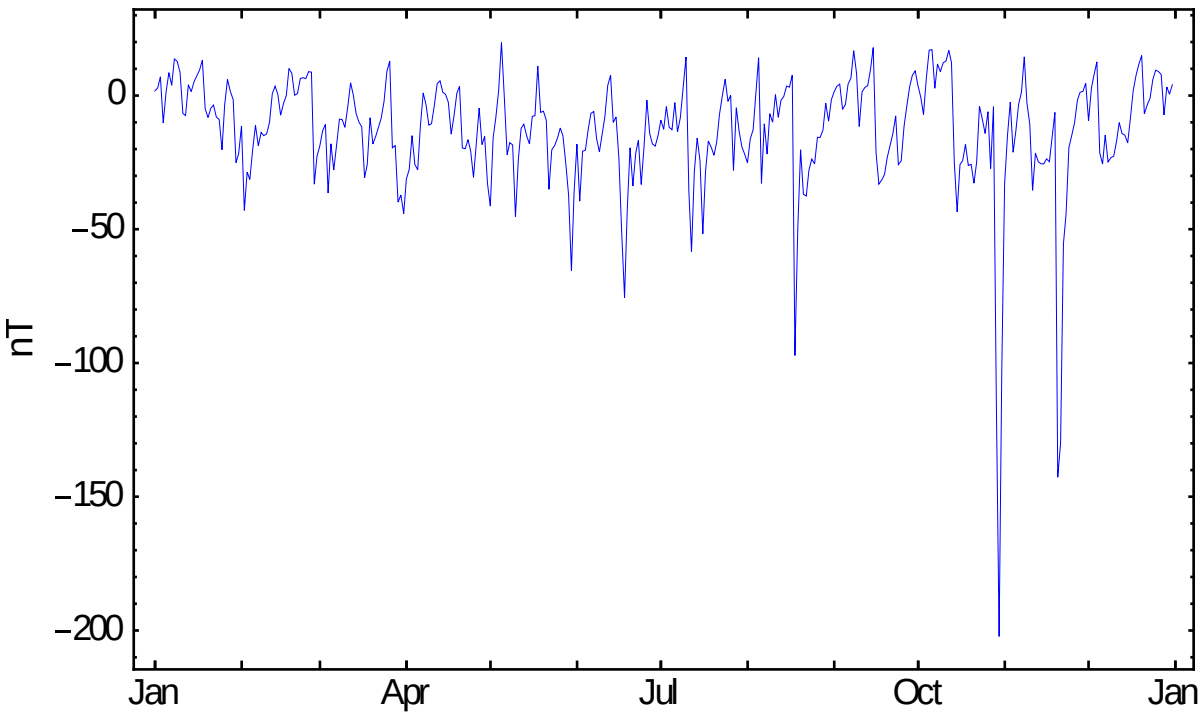

Figure 2-4: Daily mean values of the DST Index for 2003

2.5.2 Auroral Indices

Whereas the Dst index consists of observations near the equator that gives a measure of the ring current, the auroral electrojet index gives a measure of the activity around the north pole at the Earth. "The Auroral electrojet index is derived from geomagnetic variations in the horizontal component observed at selected (10-13) observatories along the auroral zone in the northern hemisphere." [66] This consists of 4 values, AE, AL, AU, and AO. AU is the greatest value and AL is the lowest value. The AE value is the difference between the AU and AL values and the AO value is the mean of the AU and AL values. This was first proposed in 1966 by Davis and Sugiura [67]. The daily mean values of the aurora index for 2003 are given in Figure 2-5. As with the Dst index, the auroral indices are also in units of nanoteslas, but with values of greater magnitude and range. You can also clearly see the disturbance from the Halloween storm. No comparable set of indices are currently calculated for the southern polar region, since most of the area there is either ocean or Antarctica.

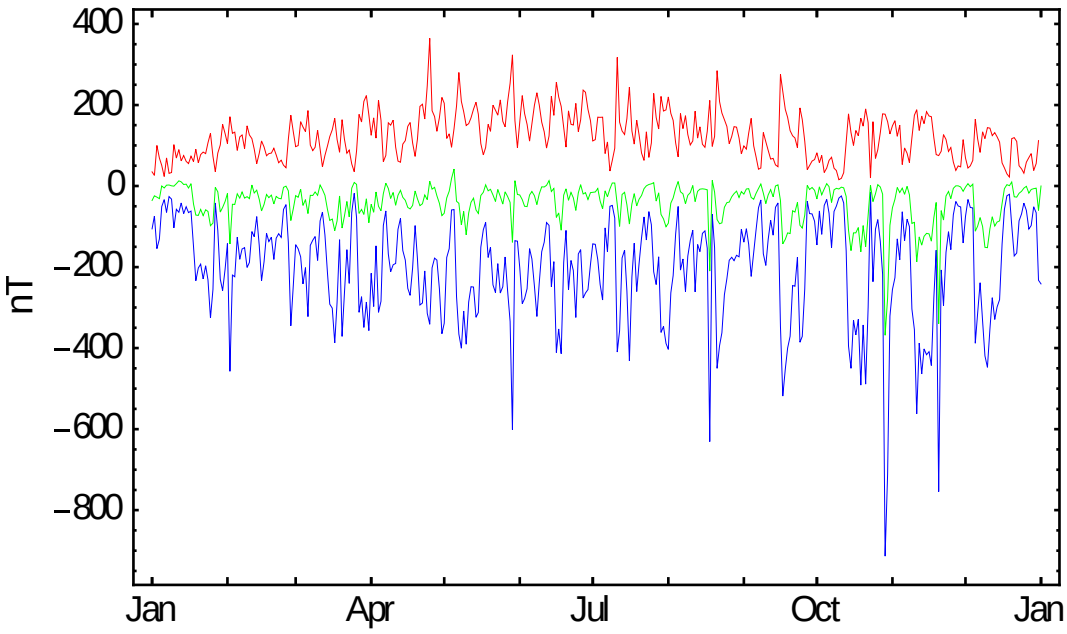

(a)

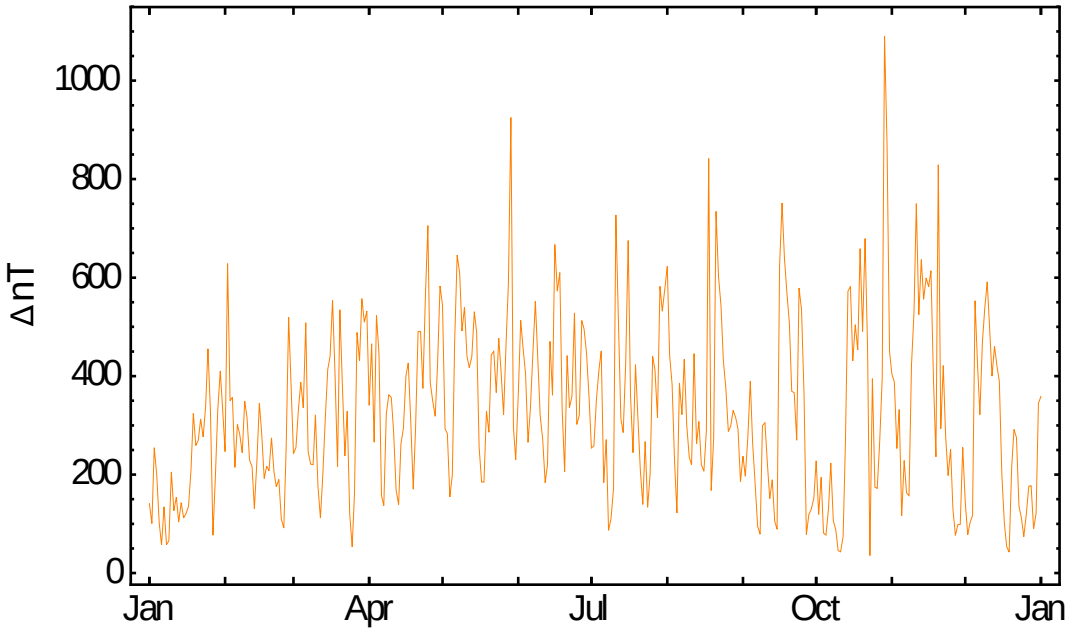

(b)

AU AO AL AE

Figure 2-5: Daily Mean values of the aurora index for 2003. (a) AU, AL, AO (b) AE

2.5.3 K_p Index

The overall measure of the impact of the solar wind on the magnetosphere is given by the K_p index [7]. K stands for the German word Kennziffer which means characteristic digit, and the P stands for planetary. This index varies on a scale of 0-9 where 0 means calm and 9 means severe geomagnetic storm as shown in Table 2-2. The K_p index is produced every 3 hours. The mean daily values for 2003 in Figure 2-6 range from a low of 0.2875 on December 19 to a high of 7.2875 on October 29, with a median of 3.0417.

Table 2-2: K_p index as it relates to geomagnetic activity [68]

K_p	G-scale	Auroral activity
0	G0	Quiet
1	G0	Quiet
2	G0	Quiet
3	G0	Unsettled
4	G0	Active
5	G1	Minor storm
6	G2	Moderate storm
7	G3	Strong storm
8	G4	Severe storm
9	G5	Extreme storm

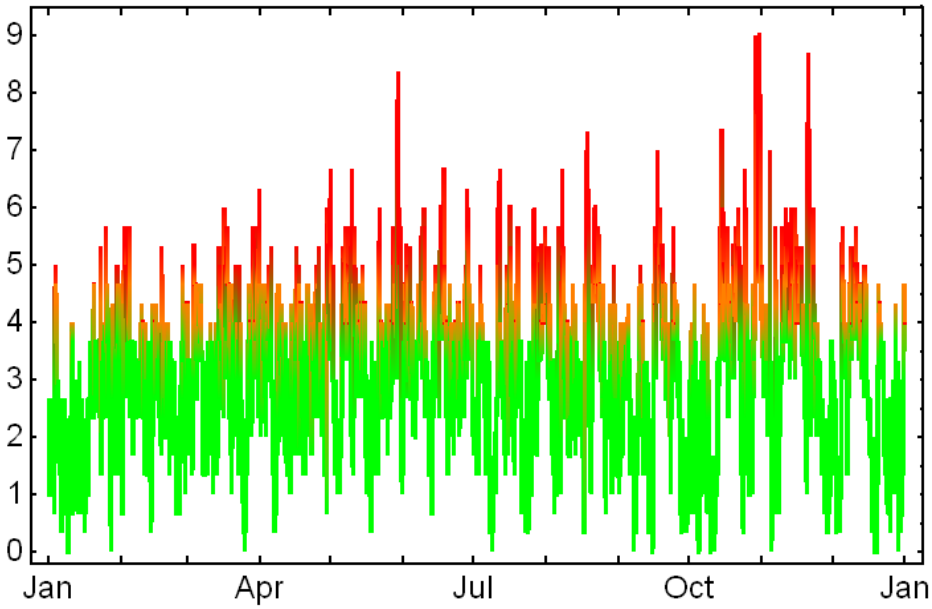

Figure 2-6: K_p index in 3-hour intervals for 2003. Green (<4) means quiet, Orange (4) means Active, Red (>4) means Storm [68].

2.5.4 AA Index

The amplitude antipodal (aa) index consists of the average of the values of two magneto-observatories antipodal to each other, one in England and one in Australia. As with the Dst and auroral indices, it is in nanoteslas as well. The observed values go from 1868 to present, and provide a simple measure of geomagnetic data throughout history that allows us to observe overall trend lines. From Figure 2-7 and as noted in other papers we can see that there is an overall upward trend in geomagnetic disturbances, at least until the peak that occurred in 2003. Since then, there has been a downward trend. It will take several sunspot cycles to determine if this downward trend holds, or if we are just at a local minimum at this point and the upward trend will continue.

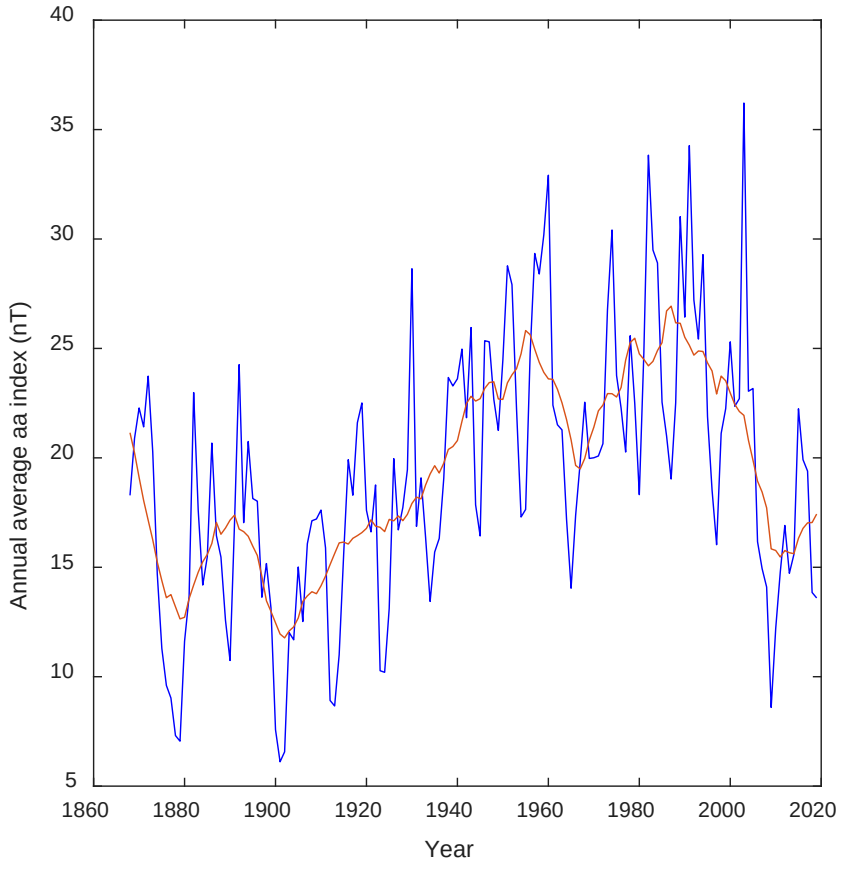

Figure 2-7: Annual average aa index for the years 1868-2019. Blue is the annual average; Red is the 11-year moving average

2.6 Human impact on Space Weather

Just as humans have had an impact on Earth's weather and climate, humans have also had an impact on the space weather surrounding Earth. Nuclear weapons and VLF radio transmissions have affected the ionosphere and magnetosphere [69]. From 1958-1962, the United States and the Soviet Union conducted a series of tests that produced artificial radiation belts, listed in Table 2-3. For reference, the traditional boundary of space, the Kármán Line, is at 62 miles (100 kilometers) above sea level. Above this boundary, the atmosphere is too thin to maintain lift in an airplane or the use of its control surfaces to alter direction. The 1963 Treaty Banning Nuclear Weapon Tests in the Atmosphere, in Outer Space and Under Water currently prohibits tests of this nature in the future among the signatories [70]. Of the declared nuclear powers, China and North Korea are not signatories.

Table 2-3: List of Nuclear explosions that created radiation belts [71]

Explosion	Location	Date	Yield	Altitude (miles)	Altitude (km)
Argus I	South Atlantic	1958	1 kiloton	300	482.8
Argus II	South Atlantic	1958	1 kiloton	300	482.8
Argus III	South Atlantic	1958	1 kiloton	300	482.8
Starfish	Johnson Island, Pacific Ocean	July 09, 1962	1.4 Megatons	248.5	400
USSR	Siberia	October 22, 1962	Several Hundred Kilotons	?	?
USSR	Siberia	October 28, 1962	?	?	?
USSR	Siberia	November 01, 1962	?	?	?

One of the products of the detonation of nuclear weapons is the creation of high energy gamma radiation, consisting of photons. These photons interact with the molecules of the atmosphere to create electrons via Compton scattering. If the nuclear weapon is detonated at a high altitude, the electrons created can form an artificial radiation belt around Earth. Another way that electrons are produced are through neutron decay, either from free neutrons or fission byproducts.

As stated in [71], when these electrons are released, they follow three different paths of motion. These are:

1. "A rapid gyration of the particles around the field line,"
2. "A bouncing back and forth along a field line from one hemisphere to the other"

3. “A slow drift in longitude around the earth.”

Electrons in a natural radiation belt also follow these paths of motion. From this, the nuclear tests helped us to understand the structure and generation of the radiation belts surrounding Earth and other bodies.

VLF are the only radio waves that are capable of penetrating sea water and are used to send low bandwidth messages to submarines. These transmissions can also affect the ionosphere by altering particle trajectories and causing them to be absorbed into the atmosphere rather than remaining in the Van Allen radiation belts through a process called Radiation Belt Remediation. This process extends out to 2.8 Earth radii. Since VLF transmissions predate the space age, it is possible that the Van Allen Radiation belt has never been observed without human alterations of it [72].

2.7 Impact on Terrestrial Systems

Space weather was first recognized to have an impact on human technology in the nineteenth century. The first recorded instance of space weather affecting technology occurred in 1847 when W. H. Barlow [73] noticed that there were deflections of an unknown origin in gauge needles connected to telegraph lines in England that seemed to occur in relation to auroras.

In 1850, the first telegraph cable connected England and France and the first transatlantic cable was laid in 1858 connecting Newfoundland and Ireland. By 1859, over 100,000 miles of telegraph cable was in use. In August and September of that year, it was noticed that the numerous telegraph systems in use all began acting strangely in relation to significant Auroras caused by a solar flare. Some telegraph operators were unable to get any messages through while others were able to operate after disconnecting the batteries, using nothing but GIC [3].

The first recorded instance of a solar storm affecting the power system occurred on March 24, 1940. The previous great storm, which occurred from May 13 to May 16 in 1921, did not have a measurable effect, which could be due to difference in storm magnitude or the fact that the electrical grid was not as developed at that time. The effects of the 1940 storm affected numerous systems that were electrically isolated from each other in the New England States, New York, Eastern Pennsylvania, Minnesota, Quebec, and Ontario at the same time (16:40 UTC). Systems in southern and western states were unaffected. The effects observed fall into

two principle classes of problems: “those in which transformers were thrown out of service by functioning of the protective relays or blowing of fuses and those in which large reactive power-surges were observed.” [74]

As time progressed, the electric grid became larger, more interconnected, and more complex, and space weather began having a larger impact on it. On March 13, 1989, a geomagnetic storm struck Earth and caused the failure of the Hydro-Québec system [75]. A coronal mass ejection impacted the magnetosphere and induced a substorm. Currents generated by this substorm first caused a Static Var Compenstator (SVC) to fail at 02:44:17 EST. This in turn provoked a cascade reaction throughout the power system with multiple SVCs failing until the entire system collapsed at 02:45:49 EST, 1 minute and 32 seconds later. The blackout continued for 9 hours after the 7 SVCs failed [76]. The estimated cost of that failure was 6.5 million Canadian dollars in material damages and net costs of 13.2 million Canadian dollars [77]. Today there are a total of 11 SVCs at the Hydro-Québec system.

The signature of a GIC impact on a power transformer is given in [78]. GICs consist mainly of very low frequency currents, approaching direct current. One possible mitigation procedure is the use of capacitors in series to allow alternating current to pass but block direct current, however in one case that has been shown to actually increase the GIC load on the system [79]. Another possible mitigation procedure is the use of specially designed transformers, where the cores are wound so that the effects of GIC is canceled out. A third is to have a high resistance to ground. These are passive mitigation procedures. Active mitigation procedures would be to create a counter current opposite in magnitude to the GIC to cancel it out.

Similar to a power system, pipeline networks spread out over hundreds of kilometers. They consist of steel with a non-conductive coating and can act like antennas coupling to changes in the magnetic field induced by space weather. Imperfections in the coating may result in corrosion in the pipelines and in holes in the coating to the ground. According to Gummow in [80], one amp of current discharge for a year can result in the loss of 10 kg of steel. One way to mitigate this loss is to maintain a small current from the Earth to the pipeline, between 850 and 1150 mA [81]. One of the main differences between the pipelines and power cables is that power cables have low resistance grounds at the transformers on both ends of the cable, while pipelines are have high resistance paths to the ground through the length of the pipeline [31]. In addition, the infrastructure components that are usually damaged in the power grid are the transformers

located at the ends of the power cable, while for the pipeline, it is the pipeline itself that is damaged.

Another metallic network that extends over large distances is the railroads. The GIC has been known to have an impact on them as well as shown in [82, 83]. The first incident was recorded in 1921 when the effects of a space storm shut down New York Central Railroad below 125th street and provoking a fire in the control tower at 57th Street and Park Avenue. In 2004, out of 3916 anomalies in the equipment used to control the East Siberian railway (latitude 46-51°N, longitude 168-187°E), 20 of them were traced to GIC. The others were caused by various terrestrial factors, such as weather, equipment failure, and vandalism, to name a few. The anomalies triggered "false engagement of railway tracks and the appearance of a red signals instead of a green ones," which results in train delays and with it a large amount of lost revenue. Other railways in Russia have reported similar issues with GIC.

Space weather and cosmic radiation have been known to have an impact on computer systems. Besides the potential for power outages and added signal noise, high energy particles can cause data errors [84]. As supercomputer speed and memory increases there are two effects. One is that the increased surface area of the amount of silicon present increases the probability of the hit by a cosmic ray particle. In addition, as transistors get smaller, the amount of energy needed to flip a bit gets smaller. These two factors cause an increasing number of faults as supercomputer speeds increase. Virginia Polytechnic and State University constructed a supercomputer out of 1,100 Macintosh G3 computers called Big Mac in 2003. This computer did not have error correcting memory to detect and handle faults. Because of this, the computer could not go through a complete startup without crashing because the faults were happening so quickly. Virginia Tech has replaced this system by one that has error-correcting memory, and these faults have not happened since.

According to recently declassified documents, the August 4, 1972 solar storm mentioned in the introduction to this chapter also detonated a large number of mines off the coast of Vietnam that were placed just 3 months earlier [85]. The sea mines were magnetically sensitive, set to detonate "when magnetic variations exceeded preset thresholds for one or more magnetic factors (e.g., amplitude, polarity, rate of change, and/or gradient)." As a result of this, the Navy replaced the magnetic mines with magneto/seismic mines.

Space weather can also affect satellite navigation systems. GPS works by calculating the position of the receiver based on calculated time delays from 4 different GPS satellites. When the total electrons is significantly increased, this creates time delays in the signal by increasing the path length, which can cause an error in the calculated distance by up to 50 meters or event make it impossible to calculate position [86].

The sun is the largest driver of Earth's weather. The total solar output is $4 \cdot 10^{26}$ W with Earth receiving $1.6 \cdot 10^{17}$ W of it ($4 \cdot 10^{-8}$ %) [5]. The energy Earth receives in solar radiation drives all wind and weather systems such as the trade winds, prevailing westerlies, hurricanes, thunderstorms, etc. However, this is not the only impact that the sun has on terrestrial weather; space weather has an impact as well. In one incident, the solar maximum of 1979 brought the Skylab space station to an early reentry. This was due to increased drag on the space station when the outer atmosphere expanded from heating induced by space weather. NOAA criticized NASA for using an inaccurate model to calculate Skylab would reenter. NASA's model showed that the station would reenter the atmosphere in 1983, 4 years later [87].

Chapter 3 Fractals and Multifractals

The concept of fractal was coined by Benoit Mandelbrot [88] in 1975 from the Latin adjective Fractus, which means broken. It turns out that fractals refer to mathematical and natural objects that have been known for a long time, but did not fit in with standard definitions. Early examples are the Peano curve created by Giuseppe Peano in 1890 [89], the Hilbert Curve created by David Hilbert in 1891 [90], and the Koch curve created by David Koch in 1903 [91]. The Koch curve is shown in Figure 3-1.

There is no one universal definition for a fractal. Typically, a fractal is a self-similar object since its characteristics are replicated across several scales either exactly or statistically. It is also a function that is irregular in some sense to exclude trivial self-similarity such as a line, which is made of straight lines. The full set of characteristics are given in [92]. Fractals are usually defined by three properties, namely dimension, lacunarity, and porosity, with dimension being the most common one.

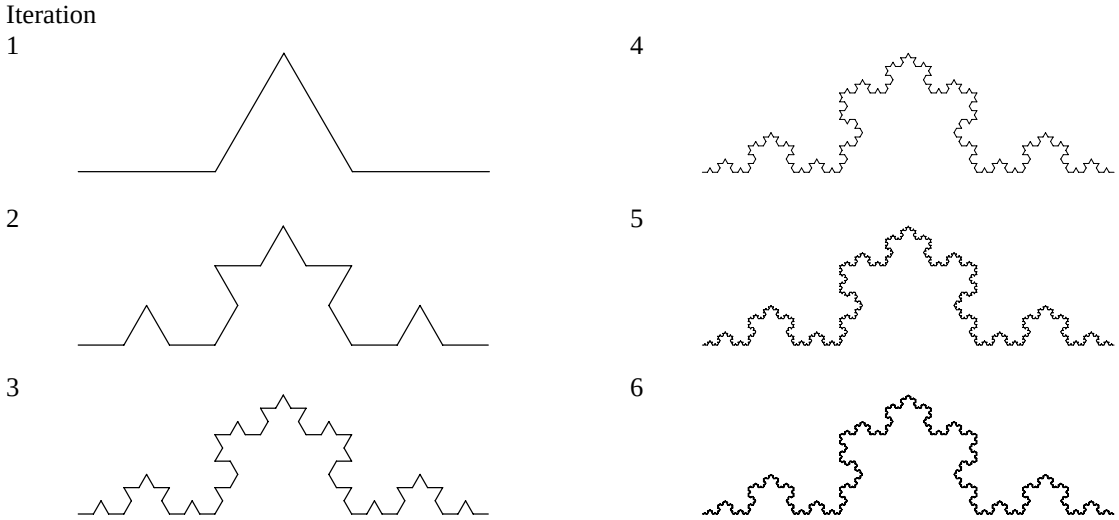

Figure 3-1: Koch Curve. Similarity Dimension Log(4) / Log(3) ≈ 1.26185

3.1 Dimensions of a Set

According to [93], there are several different definitions for dimension of a set. The most basic dimension of a set is the one that is defined as its degrees of freedom. Let us provide a few examples to clarify this concept. The function, y = f(x), of one dependent variable, y, and one independent variable, x, defines a set consisting of a collection of one-dimensional points in $\mathbb{R}^1$. The equation of a circle, $x^2 + y^2 = r^2$, of two independent variables, x and y, defines a two-dimensional set in $\mathbb{R}^2$. The equation of a sphere, $x^2 + y^2 + z^2 = r^2$, of three independent variables, x, y, and z, defines a three-dimensional set in $\mathbb{R}^3$. These are well-behaved mathematical objects, but many objects are not. For instance, objects such as the Koch curve have infinite length but zero area. Others like the Cantor set are uncountable but have zero length. The Weierstrass function is "continuous everywhere but differentiable nowhere". These pathological functions require refinements of the concept of dimension and of other properties.

The Hausdorff dimension generalizes the usual dimension seen before to cover both well-behaved as well as pathological objects. The Hausdorff dimension of a set F is defined in [92] as

$$\mathcal{H}_\delta^s(F) = \inf\{\textstyle\sum_{i=1}^{\infty}|U_i|^s : \{U_i\} \text{ is a } \delta - \text{cover of } F\}, \tag{3.1}$$

$$\mathcal{H}^s(F) = \lim_{\delta\to 0} \mathcal{H}_\delta^s(F), \tag{3.2}$$

where s is a non-negative integer. In other words, for a given s, the $\mathcal{H}^s(F)$ is equal to the limit as $\mathcal{H}$cover of F tends to zero of the infimum of the summation of the different covers raised to the s power. When s is less than or greater than the Hausdorff dimension of the set, then $\mathcal{H}^s(F)$ is equal to infinite or to zero, respectively. The Hausdorff dimension of the set is the finite value of $\mathcal{H}^s(F)$ when it transitions from infinity to zero.

Conceptually, if we measure the area of a square with a finite line, the measure will be infinite. This is the case because the line has folded around an infinite number of times to completely cover the square. On the other hand, if we measure the same area with a cube, that measure will be zero. Only if we measure a square with a two-dimensional object, for example using another square, then we get a non-zero and finite positive dimension. In general, we have to measure an object with another one of the same dimension to get a meaningful value.

The most common way to estimate the Hausdorff dimension is to use what is known as box counting. Specifically, we superimpose a grid of boxes over a given graph. A box is filled if one of more points in the set is contained within the box. The relationship between the number of

boxes and its side length is given by

$$N = r^{-D}, \tag{3.3}$$

where N is the number of boxes, r is side length, and D is what is known as the box counting dimension. Solving for D, we get

$$D = -\frac{\log N}{\log r}. \tag{3.4}$$

The box side length is plotted against the number of boxes on a log/log scale. The slope of the line gives an approximation of the Hausdorff dimension. An example of box counting for the Koch curve in Figure 3-1 is shown in Figure 3-2. The slope of line in Figure 3-3 for side lengths of 10^{-4} to 0.1 is approximately 1.2778, which is a relative error of 1.2658% from the theoretical Hausdorff dimension for the Koch curve.

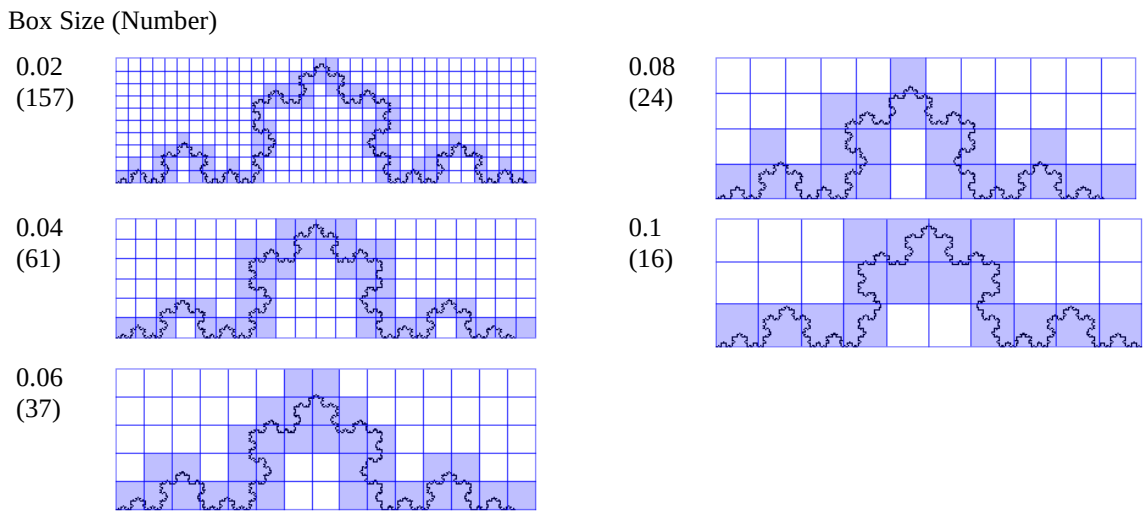

Figure 3-2: Example of the box counting of the Koch curve.

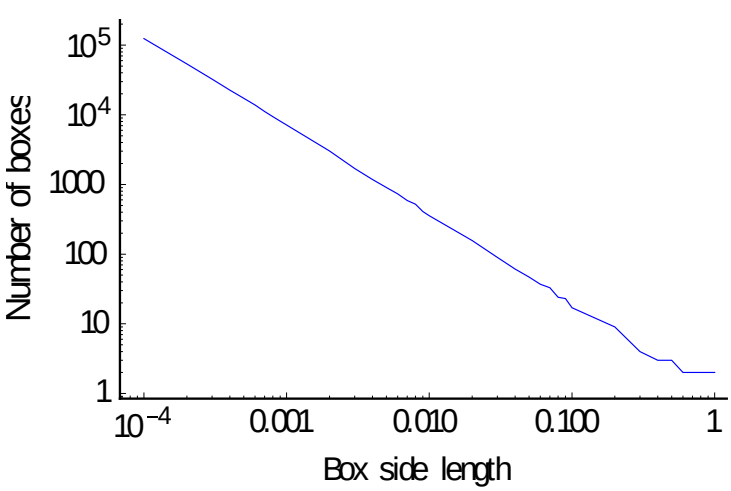

Figure 3-3: Box counting graph of the Koch curve at level 8.

3.2 Hölder Exponent

Let $f(x)$ be a locally bounded function such that $f(x) \in C^{\alpha}(x_0)$, where $C, \alpha \epsilon \mathbb{R}$, $C > 0$, $\alpha \geq 0$, that is, there exists a polynomial function P(x) of degree less than α satisfying the following condition [94]:

$$|f(x) - P(x - x_0)| \leq C|x - x_0|^{\alpha}, \tag{3.5}$$

Note that when α = 1, $f(x)$ belongs to the Lipschitz class of functions. The Hölder exponent, $h_f(x_0)$ of $f(x)$ at x_0 is is defined as

$$h_f(x_0) = \sup\{\alpha : f \epsilon C^{\alpha}(x_0)\}. \tag{3.6}$$

Essentially, it describes how the individual points are related to one another. Let us now define the concept of singularity. For fractal signals, the Hölder exponent takes values between 0 and 1, that is, $0 < h_f(x_0) < 1$; it measures the strength of the singularities present in the function $f(x)$.

3.3 Definition of Singularity in Mathematics

A singularity in mathematics is defined as a point of a function that is not well behaved in some sense, either that it is undefined or undifferentiable [95]. Two examples that are relevant to multifractal analysis are cusp singularities and oscillating singularities as shown in Figure 3-4. Cusp singularities of a function $f(t)$ is a collection of points such that for $0 < h < 1$, we have

$$f(t) = A + B|t - t_0|^h, \tag{3.7}$$

and oscillating singularities (also known as chirp singularities) of a function $f(t)$ is a collection of points such that for $0 < h < 1$, we have

$$f(t) = A + B|t - t_0|^h \sin\left(|t - t_0|^{-\beta}\right). \tag{3.8}$$

According to [96], "singularities and irregular structures often carry the most important information in signals." This is due to the fact that they represent changes to one or more of the properties of the signal.

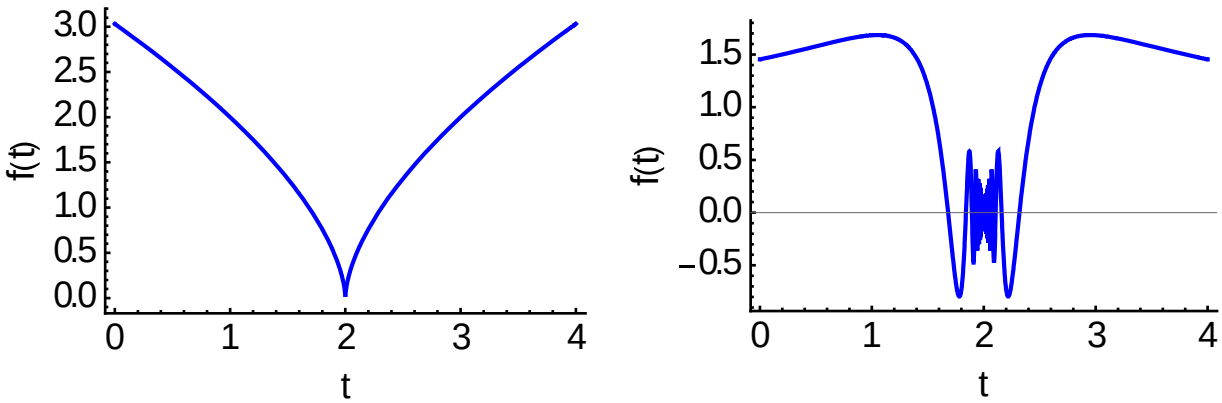

(a) (b)

Figure 3-4: Cusp (a) vs Oscillating (b) Singularities. Parameters are t_0 = 2, h = 0.6, β = 1, A = 0, B = 2

3.4 Introduction to Multifractals

Fractal signals that most people are familiar with have one Hausdorff dimension. As we discussed in the introduction, natural objects often have more than one dimension, termed multifractals, thus, enabling more accurate modelling of natural phenomenon [97].

The Hölder exponent is one of the keys to defining a multifractal. Let $f(x)$ be a locally bounded function such that $f(x) \in C^{\alpha}(x_0)$, where $C, \alpha \in \mathbb{R}$, $C > 0$, $\alpha \geq 0$, that is, there exists a polynomial function P(x) of degree less than α satisfying the following condition [94]:

$$|f(x) - P(x - x_0)| \leq C|x - x_0|^{\alpha}, \tag{3.9}$$

Note that when α = 1, $f(x)$ belongs to the Lipschitz class of functions. The Hölder exponent, $h_f(x_0)$ of $f(x)$ at x_0 is is defined as

$$h_f(x_0) = \sup\{\alpha : f \in C^{\alpha}(x_0)\}. \tag{3.10}$$

Essentially, it describes how the individual points are related to one another. Let us now define the concept of singularity. For fractal signals, the Hölder exponent takes values between 0 and 1, that is, $0 < h_f(x_0) < 1$; it measures the strength of the singularities present in the function $f(x)$.

There are two main related functions in multifractal analysis. These are the scaling exponents $\zeta(q)$, which is also referred to as τ(q) or $\beta(q)$, and the singularity spectrum, $f(\alpha)$, which is also referred to as $D(h)$ [24]. Note that $f(\alpha)$ is different from the function $f(t)$ defined in the previous section. These functions have equivalents in thermodynamics, such as "energy (α), free energy (τ/q), entropy (f), and temperature (1/q)" [98].

The partition function in multifractal/thermodynamic analysis is given by

$$\Gamma(q,\tau) = \sum_{i=1}^{N} \frac{p_i^q}{l_i^\tau}, \tag{3.11}$$

and performs a similar function to the box counting function in monofractal analysis. This partition function is of order unity only when

$$\tau = (1-q)D_q, \tag{3.12}$$

which is similar to the formal definition of the Hausdorff dimension given earlier. D_0 is the Hausdorff dimension, forming one of many dimensions of the set [99].

The moment sum is defined as

$$M_r(q) = \sum \mu(C)^q, \mu(C) > 0, \tag{3.13}$$

where $\mu(C)$ is the measure of the box or cube with side length r that covers the signal. The scaling exponents are calculated from the moment sum in (3.13) as

$$\beta(q) = \lim_{r\to 0} -\frac{\log M_r(q)}{\log r}. \tag{3.14}$$

The singularity spectrum is taken as the Legendre transform of the scaling exponent equation, which is defined as

$$f(\alpha) = \inf_{-\infty<q<\infty} \{\beta(q) + \alpha q\}, \tag{3.15}$$

and where α is the Hölder exponent.

From (3.12), the related function $D(q)$ is calculated as

$$D(q) = \begin{cases} \frac{\beta(q)}{1-q} & q \neq 1 \\ \lim_{q\to 1} \frac{\beta(q)}{1-q} & q = 1 \end{cases} . \tag{3.16}$$

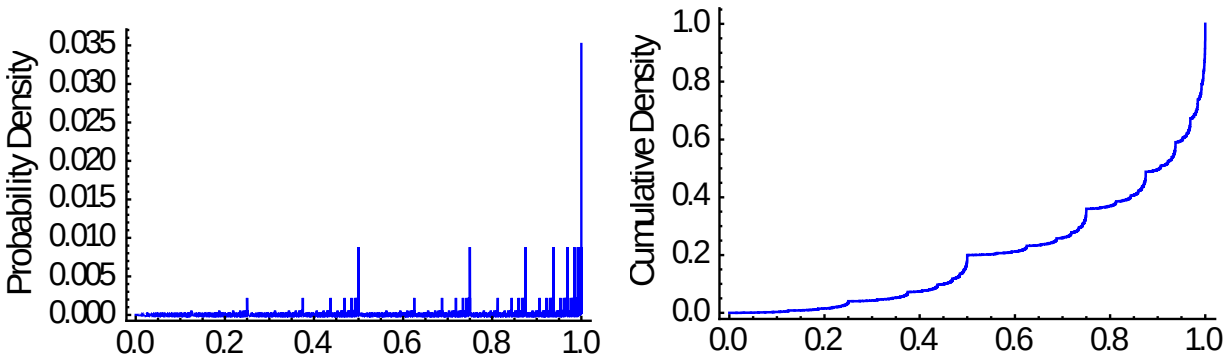

(a) (b)

Figure 3-5: Probability Density Function (PDF) (a) and Cumulative Density Function (CDF) (b) for the 20/80 Binomial Cascade.

A classic example of a multifractal is given as the distribution of gold in a rock. For this example, 80% of the gold is in half the rock and 20% is in the other. In each of those halves, you can divide half of that so that 80% in that half is in a half and 20% in the other. In the ideal case, this is repeated ad infinitum; however, in nature this only occurs for a finite number of iterations. The PDF and CDF of this are shown in Figure 3-5 for 15 iterations of this process. Lines that are the same height in the PDF have the same Hölder exponent. As we can see this consists of many intertwined fractals, which is the key characteristic of a multifractal.

The numbers and values of the intervals follow a binomial expansion, and this will be helpful to generate the singularity spectrum for this function. Longer proofs are given in [92, 98]. In this case p is $0 < p < 0.5$, so that $p < 1 - p$ and b_{total} is the number of total segments, in this case 2. The moment sums of this function are given by

$$M_{b^{-k}}(q) = \sum_{i=0}^{k} \binom{k}{i} \mathrm{p}^{qi}(1-\mathrm{p})^{q(k-i)} \ , \tag{3.17}$$

while the scaling exponents are derived from (3.17) as

$$\beta(q) = \lim_{r\to 0} -\frac{\log M_r(q)}{\log r} = \lim_{k\to\infty} -\frac{\log M_{b^{-k}}(q)}{\log b^{-k}} = \frac{\log(p^q+(1-p)^q)}{\log b_{total}} = \frac{\log(0.2^q+0.8^q)}{\log 2}, \tag{3.18}$$

with r being the segment length, in this case b^{-k}.

From (3.18), we can calculate $f(\alpha)$ by taking the Legendre transform, that is,

$$f(\alpha) = -\frac{4(\alpha-\alpha_{max})(\alpha-\alpha_{min})}{(\alpha_{max}-\alpha_{min})^2}, \alpha_{min} \le \alpha \le \alpha_{max} \ . \tag{3.19}$$

Here, α_{min} and α_{max} are given by

$$\alpha_{min} = -\frac{\log(1-p)}{\log b_{total}} = -\frac{\log 0.8}{\log 2} \approx 0.3219, \tag{3.20}$$

$$\alpha_{max} = -\frac{\log p}{\log b_{total}} = -\frac{\log 0.2}{\log 2} \approx 2.3219, \tag{3.21}$$

which are derived from

$$\alpha_{n,b} = -\frac{\log \mathrm{p}^{\mathrm{n}-b}(1-\mathrm{p})^{b}}{\log {b_{total}}^{n}}. \tag{3.22}$$

The scaling exponents and singularity spectrum for this is shown in Figure 3-6.

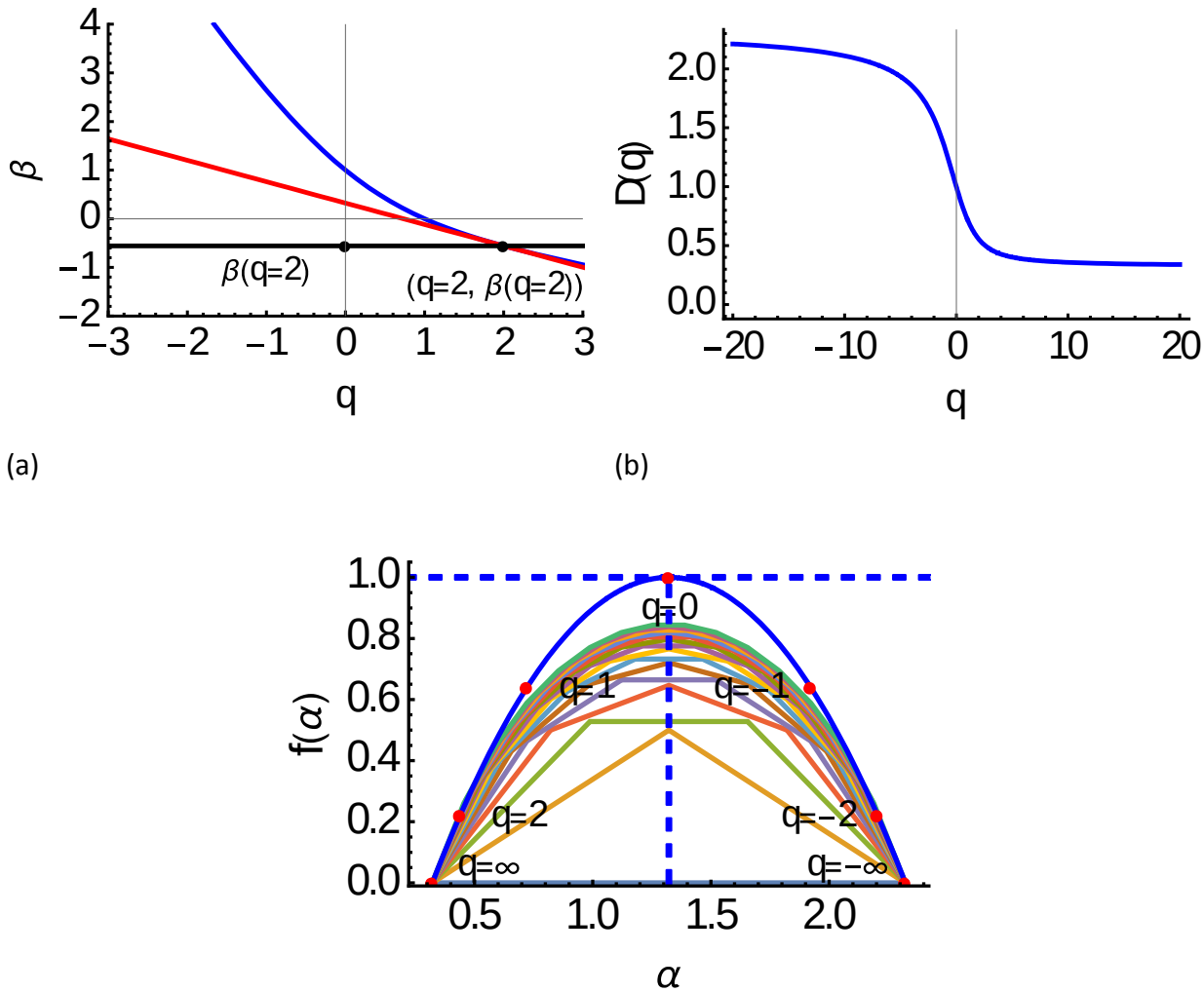

Figure 3-6: Scaling exponents (a), dimensions (b), and multifractal spectrum (c) for 20/80 Binomial Cascade. Theoretical multifractal spectrum is given in blue. Multifractal spectrum for the first 15 iterations is shown. The apex of the theoretical multifractal spectrum which is the intersection of the 2 dashed blue lines is (-log(0.2*0.8)/(2 log 2), 1) or (1.321928,1). Corresponding q values from -2 to 2 are shown.

The singularity spectrum usually cannot be determined directly [100]. This is due to the fact that the singularities are often correlated, making their identification a difficult task due to machine and data precision. In order to calculate the singularity spectrum, Frisch and Parisi [101] created the structure function, which are defined in integral form as

$$\langle (\delta v(l))^p \rangle \sim \int d\mu(h) l^{(ph+3-d(h))}. \tag{3.23}$$

There are several different ways to determine the structure functions and the singularity spectrum of a signal; in this dissertation, we shall use the discrete wavelet transform and the wavelet leader method.

Chapter 4 Methods

The wavelet transform presents an alternative to the Fourier transform and windowed Fourier transform for signal analysis. The main difference is that it involves the convolution of the signal to be analyzed with small signals called wavelets that are scaled in both time and frequency. When they are scaled, wavelets have short duration for high frequency signals and long duration for low frequency signals, maintaining the same Q as defined by

$$Q \equiv \frac{\Delta f}{f_0}, \tag{4.1}$$

where f_0 is the center frequency of the wavelet and Δf is the difference of the minimum and maximum frequencies of the filter; the reader is referred to [102] and [103] for further details. Since the basis functions of the Fourier transform are global in scope, localized information is spread throughout the transformed data, making it difficult to extract [94].

4.1 Continuous Wavelet Transform

The continuous wavelet transform was developed by Morlet and Grossman in 1984 [104]. It is an integration transform that involves the convolution of data series and the complex conjugate of a wavelet function for many time shifts and scales. Specifically, we have

$$\mathrm{CWT}\{f(t), a, b\} = \int_{-\infty}^{\infty} f(t)\psi_{a,b}^{*}(t)dt, \tag{4.2}$$

with the equation for the wavelet function given by

$$\psi_{a,b}(t) = \frac{1}{\sqrt{|a|}}\psi\left(\frac{t-b}{a}\right), a, b \in R, a \neq 0, \tag{4.3}$$

with a corresponding to the scale and b corresponding to the location.

Typically, a wavelet function satisfies the following conditions. The first condition is that it has finite energy, that is,

$$\int |\psi(t)|^2 dt < \infty. \tag{4.4}$$

Any wavelet function should satisfy this condition. This excludes functions such as the sine and the cosine functions of the Fourier transform. The second condition is referred to as the admissibility condition; it states that the Fourier transform of the wavelet function has no DC component, that is,

$$\widetilde{\psi}(\omega) = 0 \text{ when } \omega = 0. \tag{4.5}$$

Some wavelets do violate this condition.

The third condition is that the wavelet function has zero mean, that is,

$$\int \psi(t)\, dt = 0. \tag{4.6}$$

Consequently, such function must oscillate, and thus is a "wavelet" [105]. The fourth condition is that a wavelet function has an effective support. This means that this function is equal to zero or approach it outside of an effective range, which is a corollary of the first condition that it has limited energy.

The continuous wavelet transform involves the convolution of the signal to be analyzed with the wavelet function for many time shifts and scales. This shows how the signal changes at different time scales, at the cost of computational complexity, both in performance and memory.

4.2 Discrete Wavelet Transform

The continuous wavelet transform results in redundant information about the signal being analyzed since the analysis of the latter at different time scales are highly correlated. To remove this redundancy, Daubechies [15-18] developed in 1988 the discrete wavelet transform; the latter differs from the continuous wavelet transform in that only distinct scales are used, typically a power of two, and two functions are used instead of one. The discrete wavelet functions satisfy the conditions of the continuous wavelets with the added requirements of compact support, vanishing moments, and orthogonality. Compact support means that the wavelet function is defined by a finite series of coefficients and is equal to zero outside of a finite range. From these coefficients, we can implement the discrete wavelet transform as a finite impulse response filter.

In addition to the wavelet function, denoted by the Greek letter psi (ψ), a scaling function, denoted by the Greek letter phi (ϕ) is used. The difference between the two is that while the wavelet function has no DC frequency component, the scaling function does. This ensures that the transform terminates in a finite number of steps and the signal can be reconstructed with an inverse transform. The filter coefficients of the scaling filter are the wavelet coefficients in reverse order with the sign alternating. As an example, the scaling filter coefficients for the Daubechies 2 wavelet are $\left\{\frac{1+\sqrt{3}}{2\sqrt{2}}, \frac{3+\sqrt{3}}{2\sqrt{2}}, \frac{3-\sqrt{3}}{2\sqrt{2}}, \frac{1-\sqrt{3}}{2\sqrt{2}}\right\}$, and the wavelet filter coefficients are

$\left\{\frac{1-\sqrt{3}}{2\sqrt{2}}, \frac{-3+\sqrt{3}}{2\sqrt{2}}, \frac{3+\sqrt{3}}{2\sqrt{2}}, \frac{-1-\sqrt{3}}{2\sqrt{2}}\right\}$. In symbolic terms this is {a, b, c, d} and {d, -c, b, -a}. The frequency responses of these two filters are symmetric around π/2 as shown in Figure 4-1.

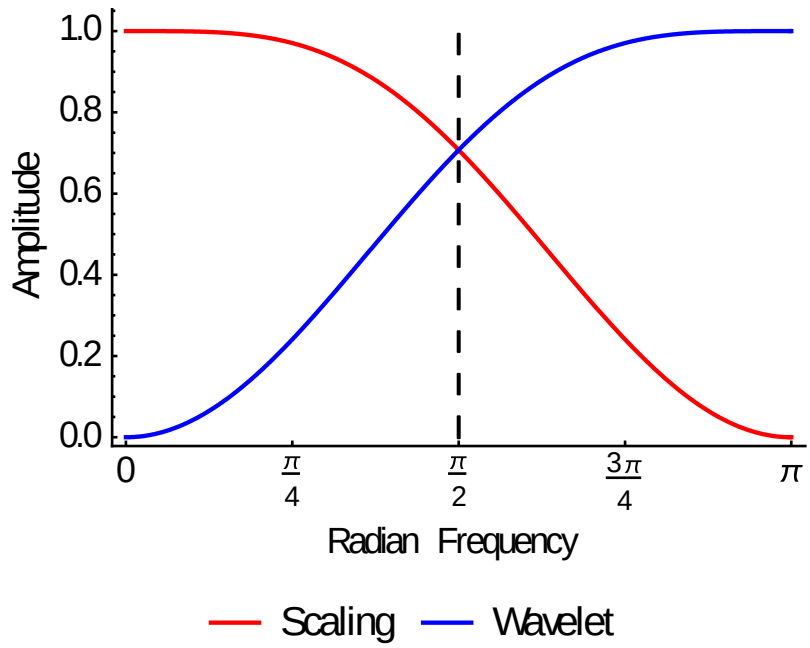

Figure 4-1: Frequency response of Scaling function (Red) and Wavelet function (Blue) for Daubechies level 2 wavelet.

In 2012 [106], the Daubechies wavelet coefficients were shown to be related to Pascal's triangle. The output of the discrete wavelet transform of a signal creates several sets of detail coefficients that are the outputs from the wavelet filter and one set of coarse coefficients that is the final output from the scaling filter.

We will now define the concepts of vanishing moments and orthogonality that are useful in multifractal analysis.

1) *Vanishing moments:* These are the *k*-th moments of a wavelet function that are equal to zero, that is,

$$\int x^k \psi(x) dx = 0. \tag{4.7}$$

Vanishing moments are needed for multifractal analysis as (3.9) shows. They can only suppress polynomial trends for data points that are not at the edge of the dataset. Since the latter data points have no polynomial suppression, they are usually excluded from the analysis. Other possibilities are that these points are extrapolated so that polynomial suppression can be applied.

2) *Orthogonality:* It is defined as the integral of the product of the scaling and wavelet

functions are equal to zero, that is,

$$\int \phi(x)\psi(x)dx = 0. \tag{4.8}$$

This ensures that the wavelet transform of the signal is represented in the most compact form possible.

The discrete wavelet transform can be used to detect both multifractal and monofractal functions. The pyramid transform gives both information both localized in time and at several different orders of magnitude [107]. This replicates in the wavelet domain the scaling information needed for fractal and multifractal analysis. In addition, the algorithm is robust in that it can handle both polynomial trends and noise.

4.3 Multifractal Analysis with Wavelets

There are several different ways to do multifractal analysis with the wavelet transform. Originally the continuous wavelet transform was used in the Wavelet Transform Modulus Maxima [96]. Later the wavelet leader method was developed using the discrete wavelet transform [26]. The main advantages of the wavelet leader method over conventional methods are (i) faster computation; (ii) easier handling of both positive and negative q values; and (iii) effective processing of both oscillating and cusp singularities.

Wavelet leaders use the discrete wavelet transform to calculate the structure functions of the data. Their basis is the dyadic cube [26], which is a covering from the box counting and is defined as

$$\lambda = \left[\frac{k_1}{2^j}, \frac{k_1+1}{2^j}\right) \times \ldots \times \left[\frac{k_d}{2^j}, \frac{k_d+1}{2^j}\right), \tag{4.9}$$

where $k = (k_1, \ldots, k_d) \in \mathbb{Z}^d$, and d is the topographical dimension of the set. Wavelet leaders are based on the dyadic cube that has the same center as (4.9), but are three times wider since we have

$$\lambda = \left[\frac{k_1-1}{2^j}, \frac{k_1+2}{2^j}\right) \times \ldots \times \left[\frac{k_d-1}{2^j}, \frac{k_d+2}{2^j}\right), \tag{4.10}$$

$$h_\mu(x_0) = \lim_{j\to+\infty} \inf\left(\frac{\log(\mu[3\lambda_j(x_0)])}{\log(2^{-j})}\right), \tag{4.11}$$

where μ is a nonnegative measure defined on $\mathbb{R}^d$. These cubes enable the analysis of negative moments. The structure functions are calculated from several moments (q) and several levels (j)

of the detail coefficients from the discrete wavelet transform of the data to be analyzed.

The wavelet coefficients often have small magnitudes, which can cause numerical instabilities for negative and fractional q values. The wavelet leaders use two methods to overcome this. The first method consists in calculating the wavelet leaders from the detail coefficients. For the first level, they are calculated as the supremum of the absolute value of the detail coefficients and its two neighbors as follows:

$$L(1,k) = \sup\{|d_{1,k-1}|, |d_{1,k}|, |d_{1,k+1}|\}, \tag{4.12}$$

while excluding the coefficients at the edges. Here, k is the index of the detail coefficient. For the subsequent levels, they are calculated as the supremum of the detail coefficients at the level of the detail coefficients and the two neighboring leaders from the previous level as follows:

$$L(j,k) = \sup\{L(j-1, 2(k-1)+1), |d_{j,k}|, L(j-1, 2(k-1)+2)\}, \tag{4.13}$$

where j is the level of the detail coefficients.

To enhance the numerical stability of the calculation, the second method excludes leader values that are less than a certain threshold, ε, say $\varepsilon = 10^{-10}$, from the calculation of the structure functions. This is carried out as follows. First, the following functions are evaluated:

$$LQ_X(q,j,k) = \begin{cases} 0 & L_X(j,k) \le \varepsilon \\ L_X(j,k)^q & L_X(j,k) > \varepsilon \end{cases} . \tag{4.14}$$

Then the structure functions are expressed as

$$S^L(j,q) = \frac{1}{n_j}\sum_{k=1}^{n_j} LQ_X(q,j,k) = F_q |2^j|^{\zeta(q)} , \tag{4.15}$$

where n_j is the number of leaders at that level. S^L are calculated over several levels (j) and several moments (q).

As [108] stated, we can derive the scaling function from the log cumulants by rewriting equation (4.15) as

$$\mathbb{E}L_X(j,\cdot)^q = F_q 2^{j\zeta(q)} , \tag{4.16}$$

If (4.16) is finite, then

$$\ln \mathbb{E}e^{q \ln L_X(j,\cdot)} = \sum_{p=1}^{\infty} C^L(j,p)\left(\frac{q^p}{p!}\right) \tag{4.17}$$

where $C^L(j,p)$ are the cumulants order $p \ge 1$ of $\ln L_X(j,\cdot)$. This yields:

$$\zeta(q) = \sum_{p=1}^{\infty} c_p \frac{q^p}{p!}. \tag{4.18}$$

The singularity spectrum relates the Hausdorff dimension, $D(h)$, to the Holder exponent,

h, which is calculated by taking the Legendre transform of the scaling exponents function, $\zeta(q)$, yielding the following dual equations:

$$D(h) = 1 + \min_q [qh - \zeta(q)], \tag{4.19}$$

and

$$\zeta(q) = 1 + \min_q [qh - D(h)]. \tag{4.20}$$

The Legendre transform is difficult to apply to actual data. An alternative way that avoids calculating the Legendre transform is to infer the singularity spectrum from the log-cumulants. This is done as follows [108]. The estimators of $\hat{\zeta}(q)$ and of the cumulant coefficients, $\hat{c}_p$, are respectively given by

$$\hat{\zeta}(q) = \sum_{j=j_1}^{j_2} w_j \log_2 S^L(j,q), \tag{4.21}$$

and

$$\hat{c}_p = (\log_2 e) \sum_{j=j_1}^{j_2} w_j \hat{C}^L(j,p) \ . \tag{4.22}$$

The estimators of $D(h)$ and h given by (4.19) expressed in terms of q are given by

$$\widehat{D}(q) = \sum_{j=j_1}^{j_2} w_j U^L(j,q), \tag{4.23}$$

and

$$\hat{h}(q) = \sum_{j=j_1}^{j_2} w_j V^L(j,q). \tag{4.24}$$

They are derived from

$$U^L(j,q) = \sum_{k=1}^{n_j} R_X^q(j,k) \log_2 R_X^q(j,k) + \log_2 n_j, \tag{4.25}$$

$$V^L(j,q) = \sum_{k=1}^{n_j} R_X^q(j,k) \log_2 L_X(j,k), \tag{4.26}$$

and

$$R_X^q(j,k) = \frac{L_X(j,k)^q}{\sum_{k=1}^{n_j} L_X(j,k)^q} \ , \tag{4.27}$$

where w are the weights assigned as the confidence given to each wavelet level. These weights must satisfy the following equations:

$$\sum_{j=j_1}^{j_2} j w_j \equiv 1, \tag{4.28}$$

and

$$\sum_{j=j_1}^{j_2} w_j \equiv 0. \tag{4.29}$$

yielding the following solutions:

$$w_j = b_j \left((V_0 j - V_1) / \left(V_0 V_2 - {V_1}^2 \right) \right), \tag{4.30}$$

and

$$V_i = \sum_{j=j_1}^{j_2} j^i b_j \, , i = 0,1,2. \tag{4.31}$$

Here, b represents the confidence given to each cumulant or structure function. For an unweighted fit, set $b_j = 1$ for all j. For a weighted fit, set $b_j = 1/n_j$, where n_j is the number of wavelet coefficient at the level j. For a weighted fit with the estimated variance set $b_j = 1$ / variance of the bootstrap estimates for j.

4.4 Bootstrapping

Usually when analyzing datasets, we have only one realization of a signal to analyze. To address this problem, we resort to bootstrapping, which is a technique to obtain statistical information from one dataset by resampling it with replacement multiple times. Each resampling forms a new dataset, from which statistical information is estimated. In the case of wavelet leaders, bootstrapping techniques can be utilized to estimate confidence intervals of the singularity spectrum and to which statistical hypothesis testing is applied to decide whether the signal is multifractal or not. Standard resampling only works if the sample is uncorrelated. Since each wavelet coefficient has a short-term statistical correlation over the support of the wavelet function, block resampling is used, where the block size is the support of the wavelet, which is twice the number of the vanishing moments for the Daubechies wavelet family. This was first proposed and implemented by Wendt, Abry, and Jaffard for the wavelet leader method in [108].

The number of samples for the discrete wavelet transform decreases by a factor of 2 for each level. Therefore, an optimal block size can be defined, whose size depends on the number of samples at each level, which are referred to as time/scale blocks. Wendt, Abry, and Jaffard [108] found that this choice had little impact on the estimators. In this dissertation we are going to be using the ordinary bootstrap.

Along with the bootstrap method, various statistical models can be utilized for statistical hypothesis testing. Wendt, Abry, and Jaffard [108] found that the percentile method gave reasonable performance of the estimator with low computing time; therefore, it will be used for hypothesis testing in this dissertation. In other papers, this would be referred to as a median

based estimator. The advantage of the percentile method is that it does not require the application of the double bootstrap, which we find advantageous when doing analysis of multiple datasets.

4.5 Surrogate data analysis

In order to properly analyze multifractal signals, analysis of surrogates also need to be performed. Two different ways to do this are the shuffled data point test and the Iterative Amplitude Adjusted Fourier Transform (IAAFT) test. A list of the complete surrogate data tests is given in [29]. The shuffle data point test involves creating numerous new signals by shuffling the order of the points of the original signal. This creates a set of signals with the same amplitudes. The IAAFT test involves creating numerous new signals with the same Fourier power spectrum as the original. These tests destroy any correlation between the points, removing any non-linear artifacts in the signal. From this, we can statistically test the collections of signals to see if the multifractal characteristics change, in this dissertation the cumulants. If they do change, we know that the multifractal characteristics are unique to the signal. If not, then they are dependent on the Fourier power spectrum or the points themselves. Figure 4-2 shows the results of the IAAFT on one instance of the pipeline data. As you can see, the Fourier power spectrum of the generated signal is approximately the same as that of the original signal.

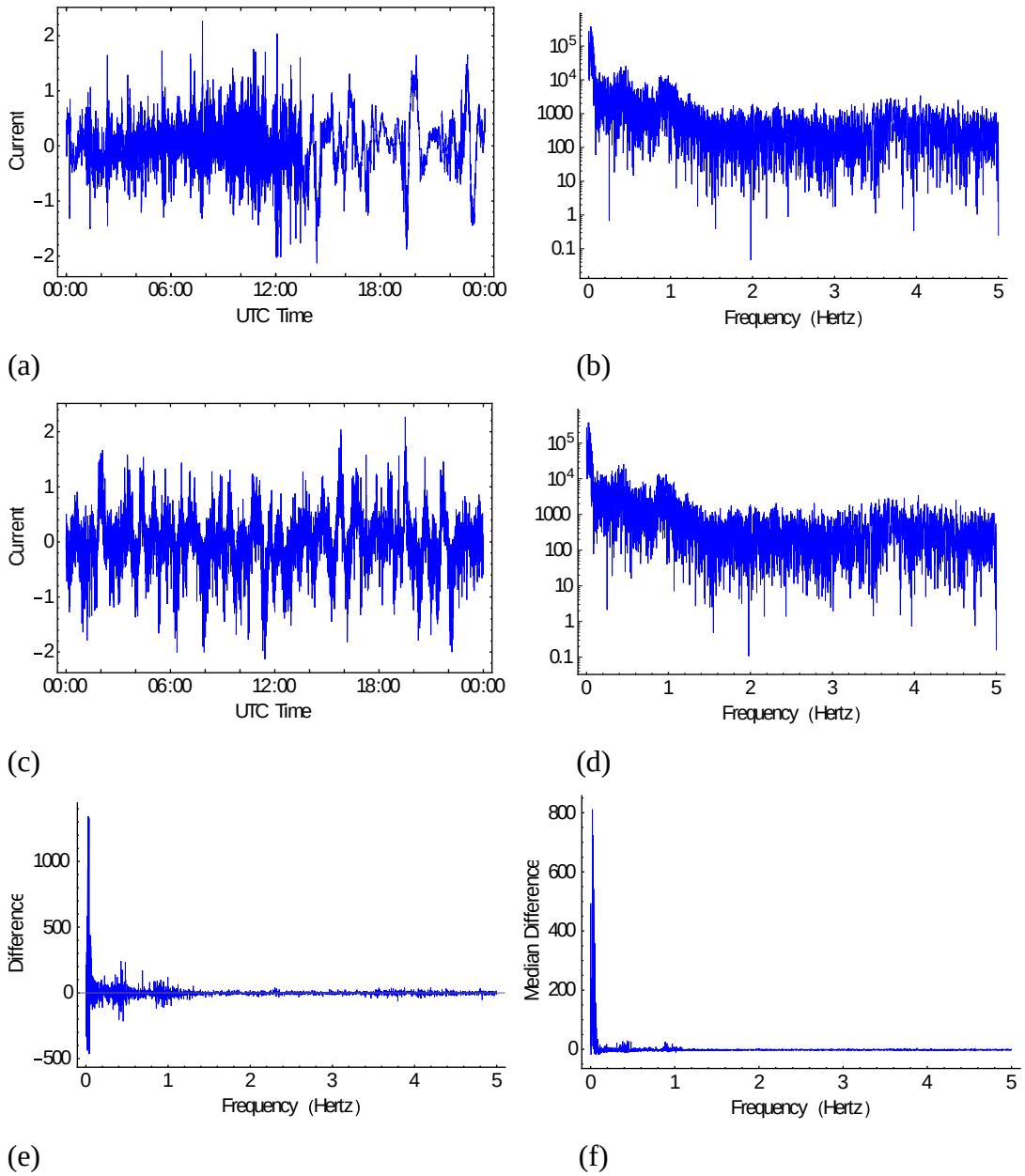

Figure 4-2: Demonstration of IAAFT. (a) Original signal, May 6, 2003 pipeline data. (b) Fourier power spectrum of original signal. (c) One instance of the IAAFT signal. Fourier power spectrum of the IAAFT signal. (e) Difference of the Fourier power spectrum of the original signal with the IAAFT signal. (f) Median difference of the Fourier power spectrum of the original signal with 200 IAAFT signals.

4.6 Automated Range Selection

With the wavelet leader method, the minimum and maximum scales (j_1 and j_2) are selected to determine the singularity spectrum. Often this is performed by selecting the scales

that visually gives the straightest line on a log-log scale. This can yield imprecise results while also being time consuming when analyzing many datasets. We automate the calculations across numerous scales and select the one that minimizes the sum of the squared residuals of the difference between the fitted line and the actual data of the cumulants and the q-functions over at least 3 scales [109]. This creates a metric that is represented by lambda (λ), with larger values yielding a better fit of the data. Automated range selection coupled with bootstrap analysis is used to provide an overview of multifractality of all the wavelet levels. Usually in this dissertation, the range with the greatest lambda is used, but at other times, other levels with lambda values near the maximum provide a better multifractal spectrum and they are used instead.

In the course of the data analysis for the pipeline datasets, a few of them result in NaN (Not a number) for some of the cumulants. This occurred when the numeric results of the calculations exceeded the maximum magnitude for a floating-point number. The algorithm was modified to select the largest lambda among the wavelet levels that had the largest number of valid cumulants.

4.7 Tests for Statistical Stationarity

The Unit root test can be used to test the signal for statistical stationary. The Mathematica program performs the unit root test using either the Dickey Fuller or Phillips Perron test. Using all available tests with multiple different parameters, the pipeline data presented in this dissertation indicated stationarity with a maximum value of $2 \cdot 10^{-9}$ for the tests performed. The Augmented Dickey Fuller test in Matlab also indicated stationarity of the data.

4.8 Alternate Tests for Multifractal Spectrum

MultiFractal Detrended Fluctuation Analysis (MFDFA) provides an alternate way to compute the multifractal spectrum, and is used here to provide some confirmation of the multifractal nature of the signals. Automated range selection, bootstrapping, and statistical hypothesis testing are not currently developed for it as they are for the wavelet leader method.

The parameters of the MFDFA algorithm are the scaling levels, the q values, and the degree of the polynomial used for detrended, denoted by M. This dissertation uses the Beyond Scaling Laws MATLAB scripts developed in [110] to do the analysis. The levels that are used in this dissertation for MFDFA analysis are the same levels that the wavelet leader automated range analysis algorithm for comparison purposes.

Chapter 5 Results and Discussion

The data that we used to carry out the analysis was provided to us by Space Research at Finnish Meteorological Institute and NASA Goddard. Details of the data collection are provided in [111, 112]. The data sets provided are samples recorded every 10 seconds of the electrical current flowing on the pipeline. The GIC collector for the pipeline is located in Mäntsälä, Finland. The dataset has 257 full days of data for 2003. At sampling every 10 seconds, we have a maximum frequency resolution of 5 hertz. From the power spectrum information given in Table 5-1, we can see that 50% of the signal energy for 50% of the signals is at 0.0602 hertz or less, with 50% of the signal energy for all of the signals at 1.6539 hertz or less, which makes these extremely low frequency signals. At 5 hertz, a signal has a wavelength of approximately 60,000 kilometers. To put things in perspective, Earth has a diameter of 12,742 km. This is why networks of extremely long conductors usually pick up these signals.

Table 5-1: Frequency Power Spectrum information about pipeline data, Kaiser Window Filtering (6th order)

Percent Signal Energy	**Frequency (Hertz)**				
		Quartile			
	Min	**25%**	**50%**	**75%**	**Max**
10%	0.0000	0.0020	0.0058	0.0116	0.2373
20%	0.0000	0.0058	0.0127	0.0208	0.8854
30%	0.0000	0.0139	0.0220	0.0336	1.4120
40%	0.0012	0.0240	0.0359	0.0616	1.5764
50%	0.0012	0.0347	0.0602	0.1293	1.6539
60%	0.0012	0.0521	0.1111	0.2752	1.9120
70%	0.0012	0.1007	0.2731	0.5498	2.4572
80%	0.0023	0.2260	0.6389	1.2306	3.5625
90%	0.0023	0.8643	1.4803	2.3634	4.3160
100%	5.0000	5.0000	5.0000	5.0000	5.0000

Table 5-2 shows how the various scales of the wavelet transform relate to the time scales of the data. The maximum number of scales for a dataset is calculated as $\lfloor \log_2 n/(m+1) \rfloor$, where n is the number of samples and m is the wavelet support, which for the Daubechies wavelet is equal to twice the number of vanishing moments. The number of samples for the pipeline data is 8640. Using the Daubechies wavelet with three vanishing moments yields a

maximum level of ten for the pipeline. These levels are the detail coefficient levels; the final level of coarse coefficients of the discrete wavelet transform is ignored.

Table 5-2: Time equivalents of the wavelet scales used for the analysis

Level	Time Scales for 10-second Sampling
0 (Raw Data)	10 seconds
1	20 seconds
2	40 seconds
3	1 minute 20 seconds
4	2 minute 40 seconds
5	5 minutes 20 seconds
6	10 minutes 40 seconds
7	21 minutes 20 seconds
8	42 minutes 40 seconds
9	1 Hour 25 minutes 20 seconds
10	2 Hours 50 minutes 40 seconds

5.1 Individual Days

The data for the individual days was analyzed using the Daubechies wavelet with three vanishing moments that have an effective support of six. A bootstrapping is applied to the wavelet transform coefficients to estimate confidence intervals for the cumulant scaling functions and the singularity spectrum. Two thousand resamples were used for the bootstrap. The percentile statistical model was used with the ordinary bootstrap. The q values for the datasets were set from -7 to 7 by 0.1.

The overall classification of the range with the largest lambda value for the datasets is given in Table 5-3. From this, we see that 67.70% were classified as a multifractal and 31.13% were classified as a monofractal. As was stated in [113], the information for most multifractal classifications can be done with the first three cumulants. This was true for this dataset; however, there were a minority of signals that would have been missed if the other cumulants were not calculated. The distribution of multifractal classifications is show in Table 5-4. For the percentile method, 10 of the datasets (3.89%) required the other cumulants for analysis. Table 5-5 has the results of the automated range selection for the data sets. 107 of the datasets (67.70%) had a length of either 3 or 4, which meets the definition of multifractal which requires that dimension

needs to hold over several levels, not all levels. However, there are quite a few datasets that have much longer lengths where the multifractality holds. There are also a number of datasets that have separate ranges that the automated range selection algorithm has identified as exhibiting strong multifractal characteristics, rather than just a single range. The distribution of the cumulants is given in Figure 5-1 with the statistics given in Table 5-6. The surrogate results in Table 5-7 show that all analyzed datasets differ in at least one cumulant with 91.83% differing in all cumulants for the shuffle test, and 57.20% different in all cumulants for the IAFFT test. What this shows is that the multifractal characteristics are independent of the individual values or the frequency spectrum.

Table 5-3: Overall classification

Classification	Number	Percentage
None	3	1.17%
Monofractal	80	31.13%
Multifractal	174	67.70%

Table 5-4: Multifractal classification

Cumulants						
c_1	c_2	c_3	c_4	c_5	Number	Percentage
1	0	0	0	1	8	3.11%
1	0	0	1	0	4	1.56%
1	0	0	1	1	1	0.39%
1	0	1	0	0	6	2.33%
1	0	1	0	1	1	0.39%
1	0	1	1	0	2	0.78%
1	0	1	1	1	0	0.00%
1	1	0	0	0	59	22.96%
1	1	0	0	1	10	3.89%
1	1	0	1	0	39	15.18%
1	1	0	1	1	7	2.72%
1	1	1	0	0	6	2.33%
1	1	1	0	1	10	3.89%
1	1	1	1	0	8	3.11%
1	1	1	1	1	13	5.06%

Table 5-5: Automated range selection results

Length	Number	
3	97	37.74%
4	74	28.79%
5	40	15.56%
6	25	9.73%
7	13	5.06%
8	8	3.11%
9	0	0.00%

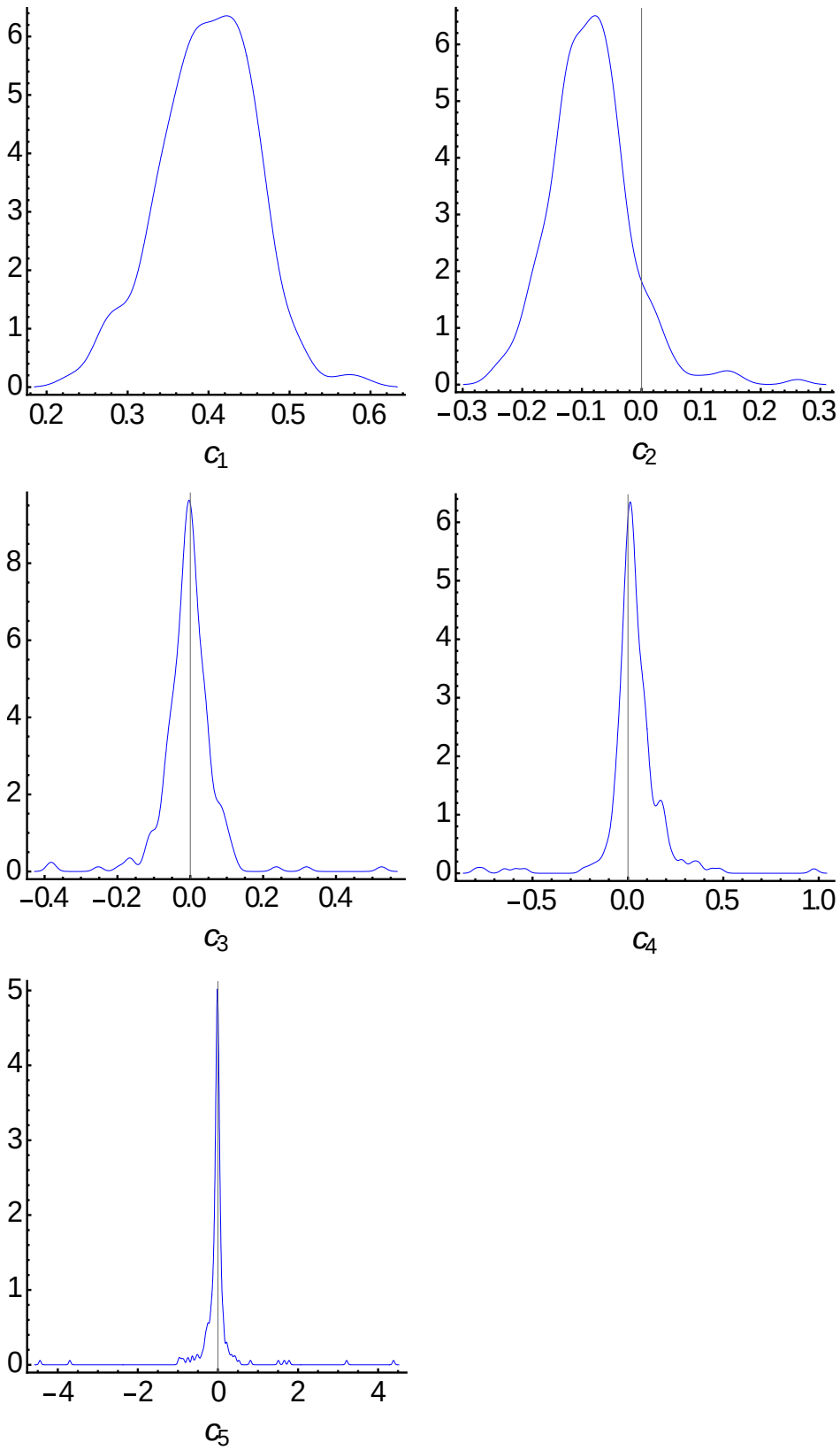

Figure 5-1: Distribution of cumulant values for pipeline data for 2003

Table 5-6: Cumulant Statistics

Cumulants	Maximum Value of PDF	Mean	Var	Min	25%	Median	75%	Max	Range
c_1	0.4225	0.3987	0.0036	0.2299	0.3607	0.4022	0.4406	0.5908	0.3609
c_2	-0.0784	-0.0848	0.0047	-0.2506	-0.1269	-0.0876	-0.0481	0.2617	0.5122
c_3	-0.0039	-0.0052	0.0056	-0.3844	-0.0348	-0.0035	0.0234	0.5249	0.9092
c_4	0.0101	0.0325	0.0224	-0.7964	-0.0133	0.0228	0.0799	0.9752	1.7716
c_5	-0.0154	-0.0341	0.3219	-4.4447	-0.0906	-0.0173	0.0288	4.3873	8.8319

Table 5-7: Overall surrogate results

Different Cumulants	Shuffle Number	Percent	IAAFT Number	Percent
0	0	0.00%	2	0.78%
1	0	0.00%	5	1.95%
2	0	0.00%	13	5.06%
3	3	1.17%	50	19.46%
4	16	6.23%	69	26.85%
5	238	92.61%	118	45.91%

5.1.1 December 19, 2003

The values for the K_p index for the December 19, 2003 is shown in Figure 5-2, with a mean K_p index value of 0.35, which is the minimum value for 2003. From this, we can see this is a relatively quiet period in the sun's interaction with Earth's magnetosphere. The recorded GIC on the pipeline in Figure 5-3 shows minimal current, with a minimum value of -0.74 amps and a maximum value of 0.89 amps. In Table 5-8, there were two adjacent ranges with the largest lambda value, one from 6-9 that was a multifractal and one from 4-6 that was a monofractal. The cumulant graphs in Figures 5-5 and 5-8 shows the fit of those ranges. The scaling exponents and singularity spectrum in Figure 5-4 and the statistical tests in Table 5-9 show that levels 4-6 has monofractal characteristics and the scaling exponents and singularity spectrum for levels 6-9 in Figure 5-9 shows multifractal characteristics. The IAAFT and shuffle surrogate tests in Figure 5-6 and Figure 5-10, and Tables 5-10 to 5-13 show significant differences in the cumulant characteristics for both ranges, indicating that the cumulants characteristics are unique to this signal. MFDFA analysis in Figure 5-7 for levels 4-6 shows a different spectrum than the one for

the wavelet leader and in Figure 5-11, shows one that is similar in structure for levels 6-9, but is shifted with the apex of the parabola at -0.2 rather than at 0.4 for the wavelet leader method.

Table 5-8: Lambda values and classifications for all ranges for December 19, 2003 pipeline data.

j_1	j_2	Length	λ	Classification	r_1	r_2	r_3	r_4	r_5
6	9	4	372.838	Multifractal	1	1	0	0	0
4	6	3	370.713	Monofractal	1	0	0	0	0
5	8	4	368.309	Multifractal	1	1	0	0	0
5	9	5	365.806	Multifractal	1	1	0	1	0
6	8	3	358.189	Monofractal	1	0	0	0	0
4	7	4	355.979	Multifractal	1	1	0	0	0
4	9	6	353.684	Multifractal	1	1	0	1	0
3	5	3	350.672	Multifractal	1	1	0	0	0
5	7	3	346.882	Monofractal	1	0	0	0	0
7	9	3	345.791	Multifractal	1	1	0	0	0
2	9	8	339.954	Multifractal	1	1	1	1	1
3	6	4	337.691	Multifractal	1	1	0	0	0
4	8	5	336.537	Multifractal	1	1	0	1	0
2	8	7	327.312	Multifractal	1	1	0	1	1
3	9	7	326.583	Multifractal	1	1	1	1	1
2	7	6	298.686	Multifractal	1	1	0	1	0
3	8	6	285.811	Multifractal	1	1	0	1	1
1	9	9	285.175	Multifractal	1	1	0	1	1
2	6	5	281.502	Multifractal	1	1	0	1	0
1	8	8	268.182	Multifractal	1	1	0	1	1
2	5	4	258.952	Multifractal	1	1	0	1	0
1	7	7	256.513	Multifractal	1	1	0	1	0
1	6	6	252.110	Multifractal	1	1	0	1	0
1	5	5	242.520	Multifractal	1	1	0	1	0
1	4	4	229.276	Multifractal	1	1	1	1	0
2	4	3	227.520	Multifractal	1	1	0	0	0
3	7	5	211.242	Multifractal	1	1	0	1	0
1	3	3	209.673	Multifractal	1	1	1	0	0
1	10	10	87.926	Monofractal	1	0	0	0	0
2	10	9	87.677	Monofractal	1	0	0	0	0
3	10	8	87.338	Monofractal	1	0	0	0	0
4	10	7	85.845	Monofractal	1	0	0	0	0
5	10	6	84.362	Monofractal	1	0	0	0	0
8	10	3	83.972	Monofractal	1	0	0	0	0
6	10	5	83.572	Monofractal	1	0	0	0	0
7	10	4	82.346	Monofractal	1	0	0	0	0

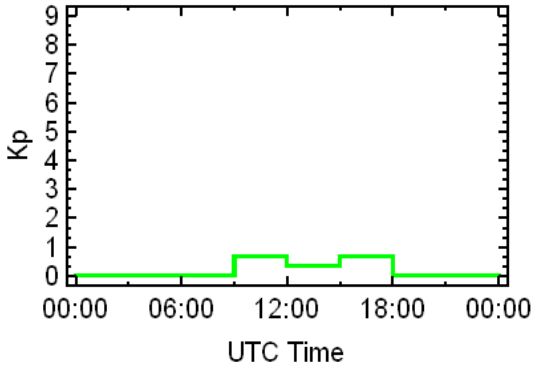

Figure 5-2: K_p index for December 19, 2003.

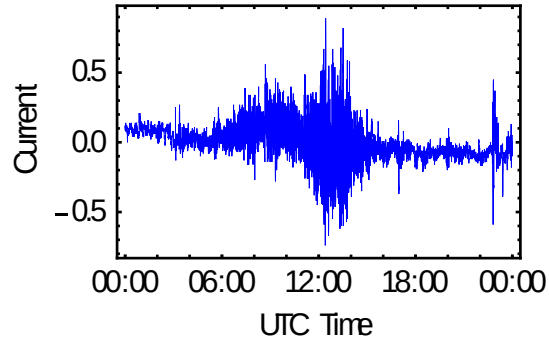

Figure 5-3: Pipeline data for December 19, 2003.

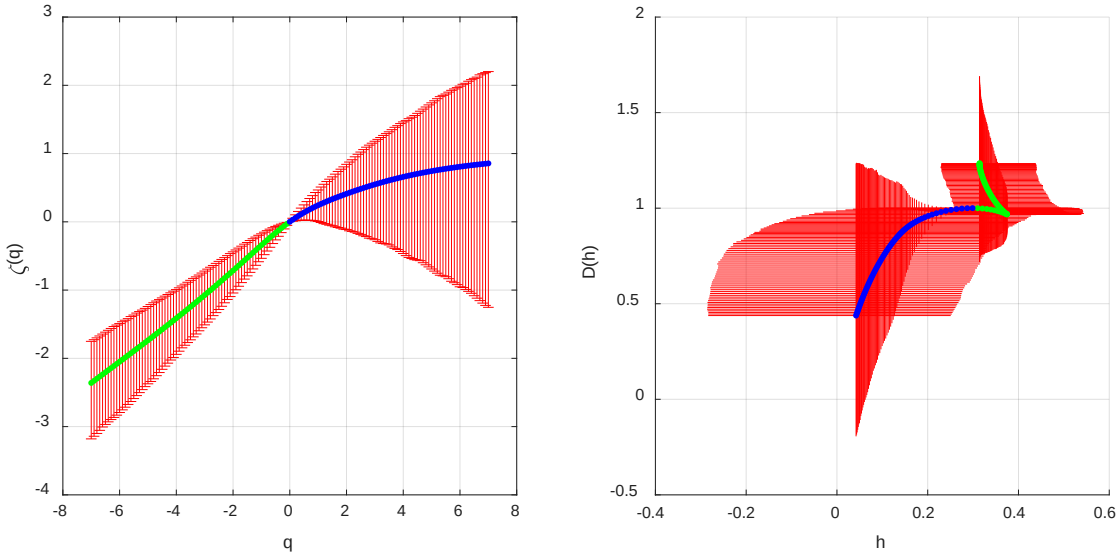

(a) (b)

Figure 5-4: (a) Scaling exponents, and (b) singularity spectrum for December 19, 2003 pipeline data for levels 4-6. Positive q values are blue, negative q values are green.

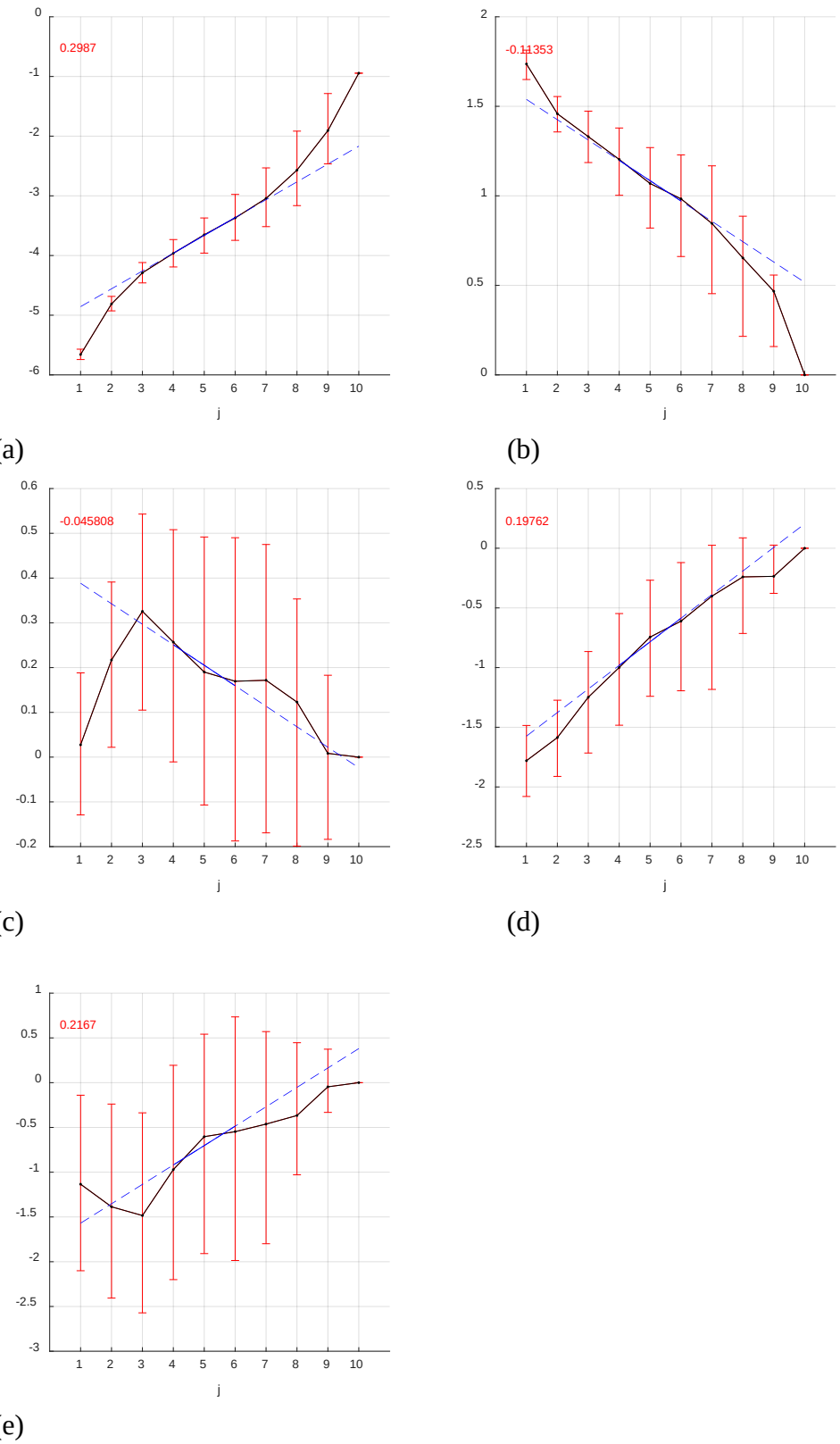

Figure 5-5: Cumulant graphs for levels 4-6 for the December 19, 2003 pipeline data. (a) c_1 (b) c_2 (c) c_3 (d) c_4 (e) c_5

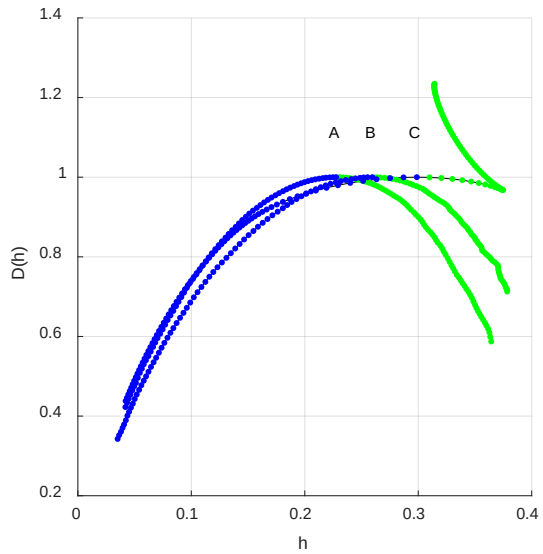

Figure 5-6: Median (a) shuffled and (b) IAAFT surrogate singularity spectrum graphs for December 19, 2003 pipeline data with the (c) singularity spectrum of the original signal for comparison for levels 4-6. Positive q values are blue, negative q values are green.

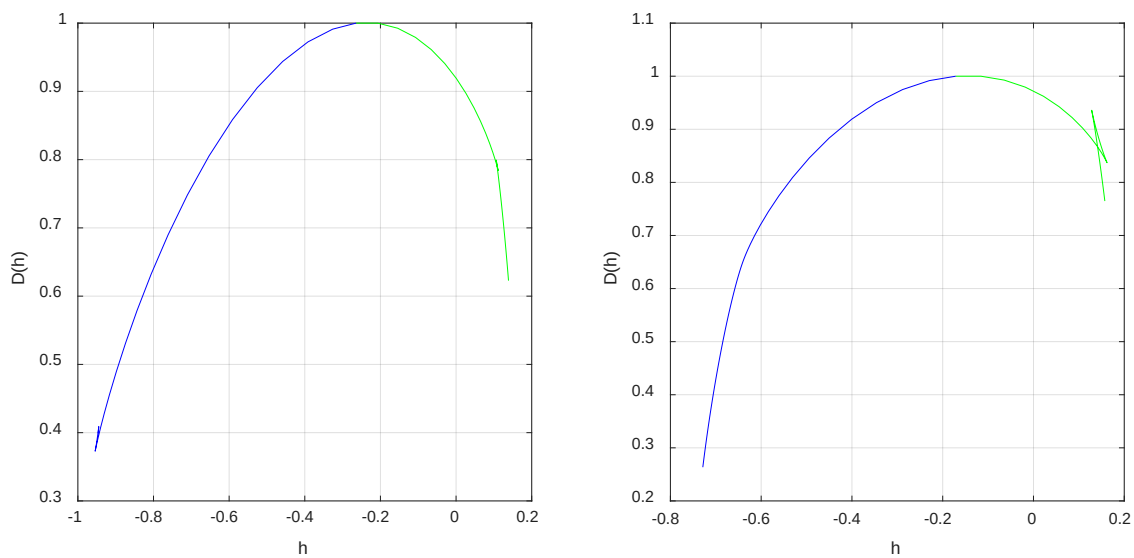

(a) (b)

Figure 5-7: Singularity spectrum generated by MFDFA for levels 4-6 of the December 19, 2003 pipeline data. (a) M = 2 (b) M = 3

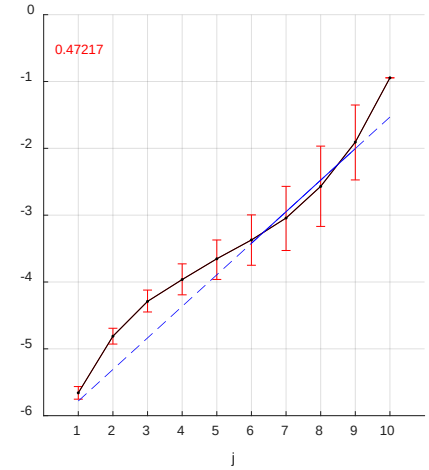

(a)

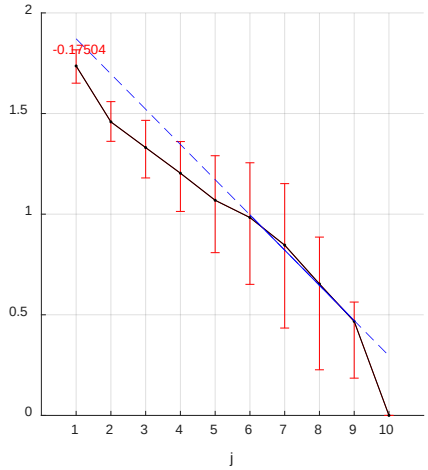

(b)

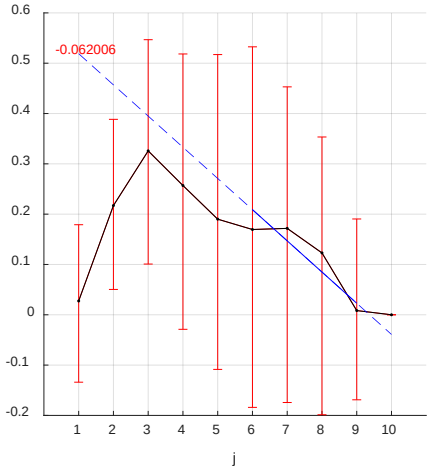

(c)

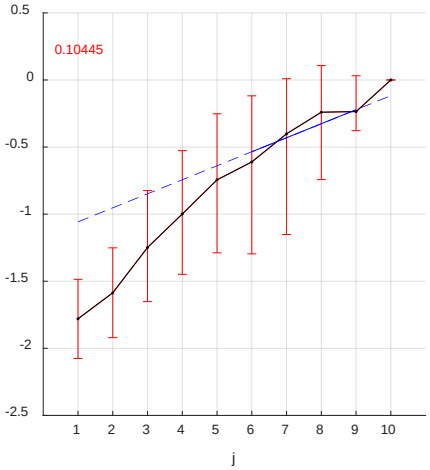

(d)

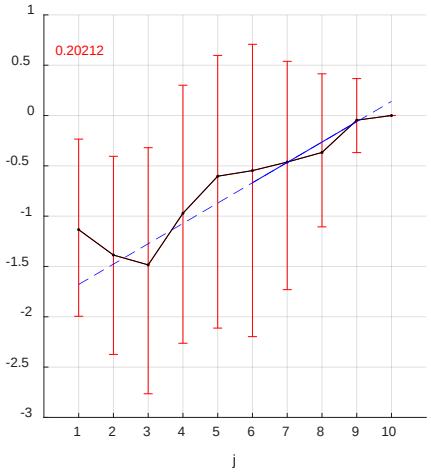

(e)

Figure 5-8: Cumulant graphs for December 19, 2003 pipeline data for levels 6-9. (a) c_1 (b) c_2 (c) c_3 (d) c_4 (e) c_5

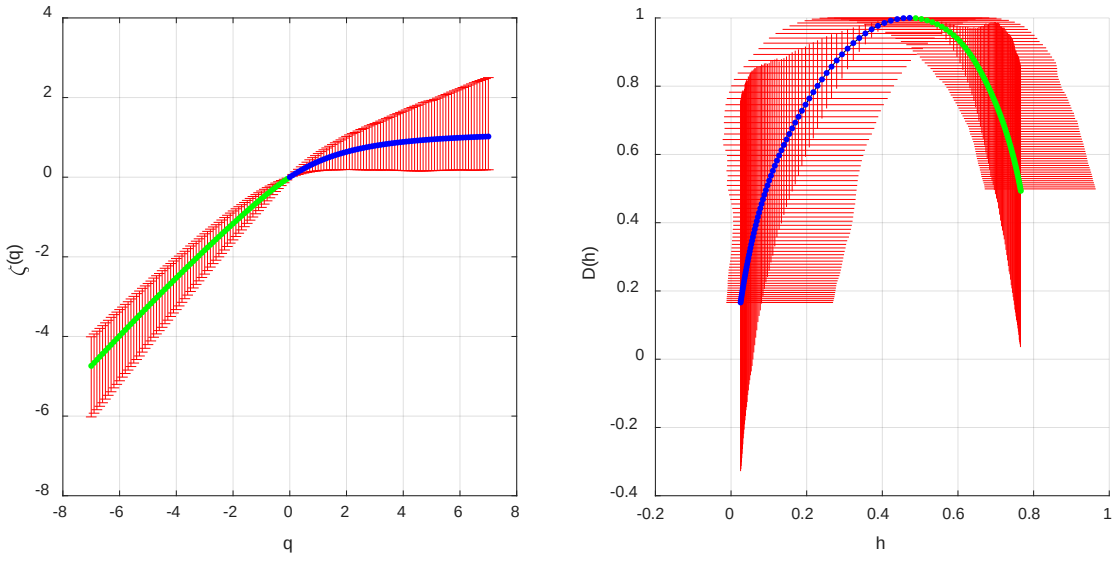

(a) (b)

Figure 5-9: (a) Scaling exponents, and (b) singularity spectrum for December 19, 2003 pipeline data for levels 6-9. Positive q values are blue, negative q values are green.

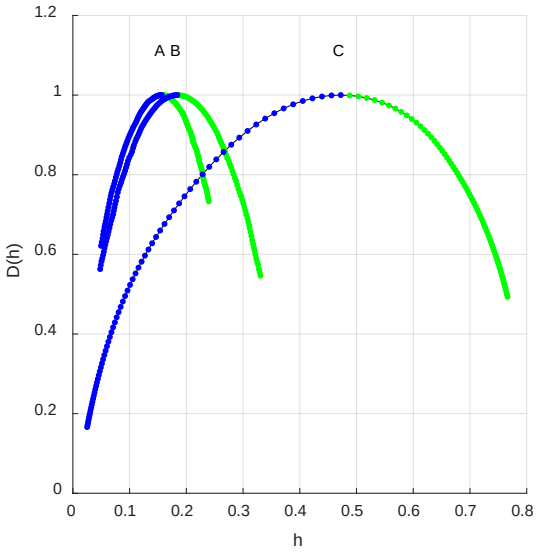

Figure 5-10: Median (a) shuffled and (b) IAAFT surrogate singularity spectrum graphs for December 19, 2003 pipeline data with the (c) singularity spectrum of the original signal for comparison for levels 6-9. Positive q values are blue, negative q values are green.

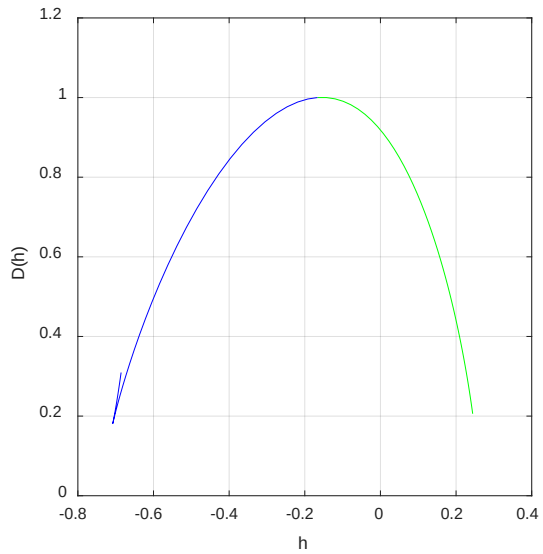

Figure 5-11: Singularity spectrum generated by MFDFA for levels 6-9 of the December 19, 2003 pipeline data. M = 3

Table 5-9: Cumulant values for the December 19, 2003 pipeline data

	Levels 4-6				Levels 6-9			
Cumulant	**Value**	**STD**	**P-Value**	**Reject**	**Value**	**STD**	**P-Value**	**Reject**
c_1	0.30	0.13	0.018	1	0.47	0.13	0.002	1
c_2	-0.11	0.10	0.230	0	-0.18	0.07	0.002	1
c_3	-0.05	0.12	0.701	0	-0.06	0.07	0.539	0
c_4	0.20	0.22	0.344	0	0.10	0.11	0.188	0
c_5	0.22	0.55	0.643	0	0.20	0.23	0.492	0

Table 5-10: Shuffle cumulant values for the December 19, 2003 pipeline data for levels 4-6

Cumulant	**Actual Value**	**Mean Shuffle Value**	**STD**	**Δ Value**	**Greater**		**Equal**		**Less**		**P-Value**	**Reject**
c_1	0.30	0.23	0.01	0.07	0	0.00%	0	0.00%	200	100.00%	0.000	1
c_2	-0.11	-0.03	0.01	-0.08	200	100.00%	0	0.00%	0	0.00%	0.000	1
c_3	-0.05	0.00	0.00	-0.05	200	100.00%	0	0.00%	0	0.00%	0.000	1
c_4	0.20	0.00	0.00	0.20	0	0.00%	0	0.00%	200	100.00%	0.000	1
c_5	0.22	0.00	0.00	0.22	0	0.00%	0	0.00%	200	100.00%	0.000	1
Total Rejection: 5		100.00%										

Table 5-11: IAAFT cumulant values for December 19, 2003 pipeline data for levels 4-6

Cumulant	**Actual Value**	**Mean IAAFT Value**	**STD**	**Δ Value**	**Greater**		**Equal**		**Less**		**P-Value**	**Reject**
c_1	0.30	0.26	0.02	0.04	1	0.50%	0	0.00%	199	99.50%	0.005	1
c_2	-0.11	-0.04	0.01	-0.07	200	100.00%	0	0.00%	0	0.00%	0.000	1
c_3	-0.05	-0.01	0.00	-0.04	200	100.00%	0	0.00%	0	0.00%	0.000	1
c_4	0.20	0.00	0.00	0.20	0	0.00%	0	0.00%	200	100.00%	0.000	1
c_5	0.22	0.00	0.00	0.22	0	0.00%	0	0.00%	200	100.00%	0.000	1
Total Rejection: 5		100.00%										

Table 5-12: Shuffle cumulant values for the December 19, 2003 pipeline data for levels 6-9

Cumulant	Actual Value	Mean Shuffle Value	STD	Δ Value	Greater		Equal		Less		P-Value	Reject
c_1	0.47	0.11	0.16	0.36	0	0.00%	0	0.00%	200	100.00%	0.000	1
c_2	-0.18	-0.01	-0.02	-0.17	200	100.00%	0	0.00%	0	0.00%	0.000	1
c_3	-0.06	0.00	0.00	-0.06	200	100.00%	0	0.00%	0	0.00%	0.000	1
c_4	0.10	0.00	0.00	0.10	0	0.00%	0	0.00%	200	100.00%	0.000	1
c_5	0.20	0.00	0.00	0.20	0	0.00%	0	0.00%	200	100.00%	0.000	1
Total Rejection: 5		100.00%										

Table 5-13: IAAFT cumulant values for the December 19, 2003 pipeline data for levels 6-9

Cumulant	Actual Value	Mean IAAFT Value	STD	Δ Value	Greater		Equal		Less		P-Value	Reject
c_1	0.47	0.19	0.03	0.28	0	0.00%	0	0.00%	200	100.00%	0.000	1
c_2	-0.18	-0.02	0.01	-0.16	200	100.00%	0	0.00%	0	0.00%	0.000	1
c_3	-0.06	0.00	0.00	-0.06	200	100.00%	0	0.00%	0	0.00%	0.000	1
c_4	0.10	0.00	0.00	0.10	0	0.00%	0	0.00%	200	100.00%	0.000	1
c_5	0.20	0.00	0.00	0.20	0	0.00%	0	0.00%	200	100.00%	0.000	1
Total Rejection: 5		100.00%										

5.1.2 April 19, 2003

The mean K_p index value for the day is 2.25, which is the 25th percentile of the total K_p index for 2003. The three-hour values are given in Figure 5-12. The pipeline data in Figure 5-13 shows a moderate increase in current from the December 19, 2003 data, with a minimum current of -1.41 amps and a maximum current of 1.78 amps. The automated range selection algorithm had the largest lambda value (365.819) for levels 2-7 as shown in Table 5-14 with the tightness of the fit of the cumulant values shown in Figure 5-15. The statistical tests in Table 5-15 and the graphs in Figure 5-14 show that this signal has multifractal characteristics as well. The surrogate analysis in Figure 5-16 shows that the singularity spectrum is closer to the original signal than the December 19, 2003 signal, however the statistical analysis in Tables 5-16 and 5-17 shows that all cumulants have different statistical values from the original signal. Figure 5-20 shows the MFDFA for the selected ranges, which is different in that the singularity spectrum is centered around -0.1 rather than 0.4 and it is more skewed with a knot around the apex.

Levels 3-8 had a lambda value of 364.264 that is near what levels 2-7 had and is presented here as well for analysis. The statistical tests in Table 5-15 show that this range also had multifractal characteristics with the tightness of fit given in Figure 5-18. The singularity spectrum and scaling exponents for this range are in Figure 5-17 which shows an elongation of the spectrum corresponding to the negative q values similar to that for levels 2-7, with a slight irregularity. The surrogate analysis in Figure 5-19 shows clear differences in the singularity spectrum between the signal and the median shuffled and IAAFT signals. The statistical tests for

the surrogate signals in Tables 5-18 and 5-19 show that the statistical hypothesis is rejected for all cumulants for levels 3-8. The MFDFA analysis has a singularity spectrum centered at 0 rather than at -0.1, which is similar to levels 2-7. It is skewed as well, but it does not have a knot around the apex.

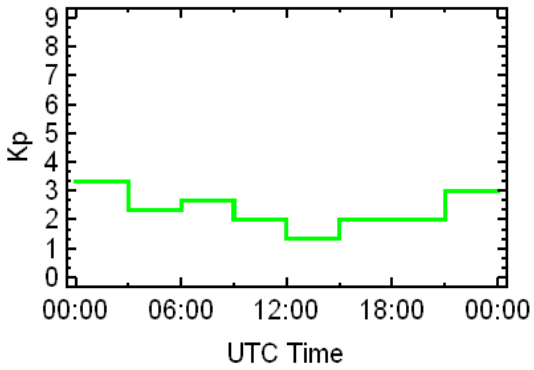

Figure 5-12: K_p index for April 19, 2003.

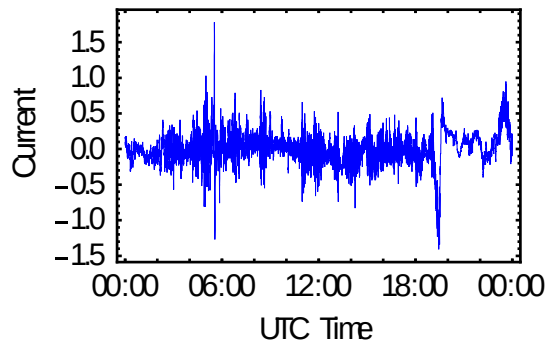

Figure 5-13: Pipeline data for April 19, 2003.

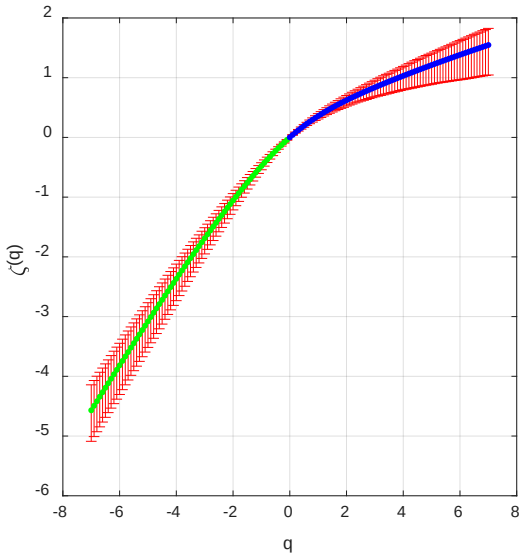

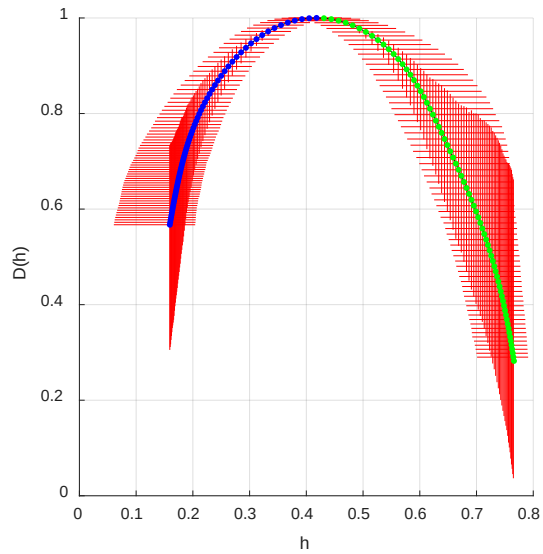

(a) (b)

Figure 5-14: (a) Scaling exponents and (b) singularity spectrum for the April 19, 2003 pipeline data for levels 2-7. Positive q values are blue, negative q values are green.

Table 5-14: Lambda values and classifications for all ranges for April 19, 2003 pipeline data.

j_1	j_2	Length	λ	Classification	r_1	r_2	r_3	r_4	r_5
2	7	6	365.819	Multifractal	1	1	0	1	0
3	8	6	364.264	Multifractal	1	1	0	1	1
6	8	3	364.247	Monofractal	1	0	0	0	0
4	7	4	361.484	Multifractal	1	1	0	0	0
4	6	3	360.594	Multifractal	1	1	0	0	0
2	8	7	358.388	Multifractal	1	1	0	1	1
2	6	5	354.905	Multifractal	1	1	0	0	0
3	7	5	350.321	Multifractal	1	1	0	0	0
5	8	4	346.736	Multifractal	1	1	0	0	0
3	6	4	336.762	Multifractal	1	1	0	0	0
5	7	3	331.425	Monofractal	1	0	0	0	0
6	9	4	326.833	Multifractal	1	1	1	0	1
4	8	5	326.360	Multifractal	1	1	0	1	0
3	5	3	321.129	Multifractal	1	1	0	0	0
7	9	3	317.870	Multifractal	1	1	1	0	0
2	5	4	314.335	Multifractal	1	1	0	0	0
1	8	8	297.108	Multifractal	1	1	0	1	1
2	9	8	296.706	Multifractal	1	1	1	1	1
1	7	7	292.352	Multifractal	1	1	0	1	0
3	9	7	286.926	Multifractal	1	1	1	1	1
5	9	5	286.906	Multifractal	1	1	1	0	1
1	9	9	285.812	Multifractal	1	1	1	1	1
1	6	6	276.335	Multifractal	1	1	0	0	0
4	9	6	255.798	Multifractal	1	1	1	0	1
1	3	3	255.685	Multifractal	1	1	0	0	0
1	5	5	242.335	Multifractal	1	1	0	0	0
2	4	3	233.356	Multifractal	1	1	0	0	0
1	4	4	212.752	Multifractal	1	1	0	0	0
6	10	5	128.266	Monofractal	1	0	0	0	0
5	10	6	127.834	Monofractal	1	0	0	0	0
7	10	4	127.547	Monofractal	1	0	0	0	0
4	10	7	124.544	Monofractal	1	0	0	0	0
8	10	3	123.659	Monofractal	1	0	0	0	0
2	10	9	123.104	Monofractal	1	0	0	0	0
1	10	10	122.310	Monofractal	1	0	0	0	0
3	10	8	122.008	Monofractal	1	0	0	0	0

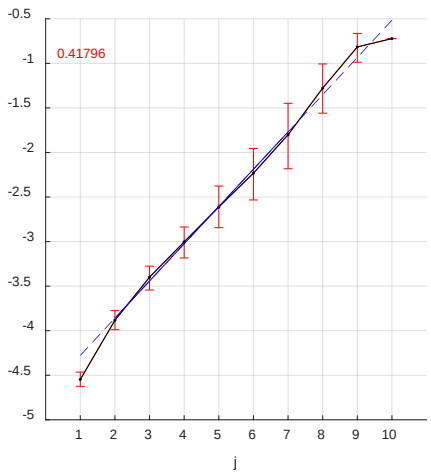

(a)

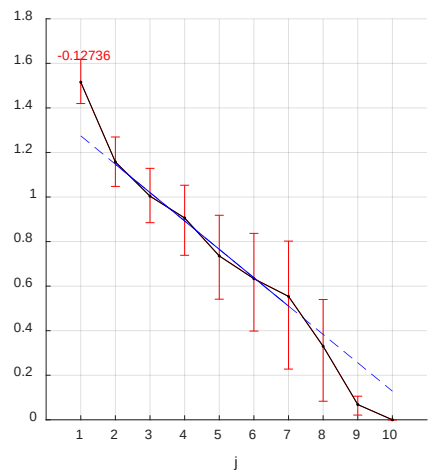

(b)

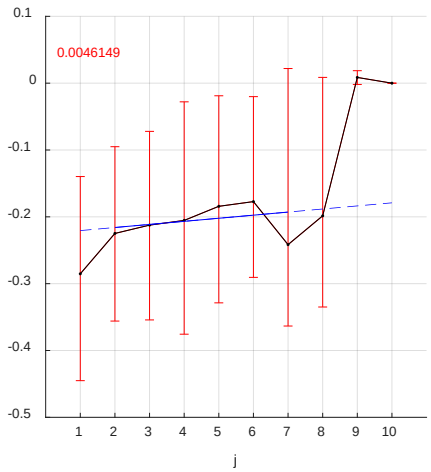

(c)

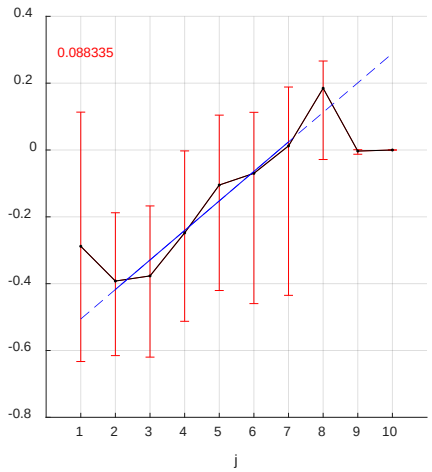

(d)

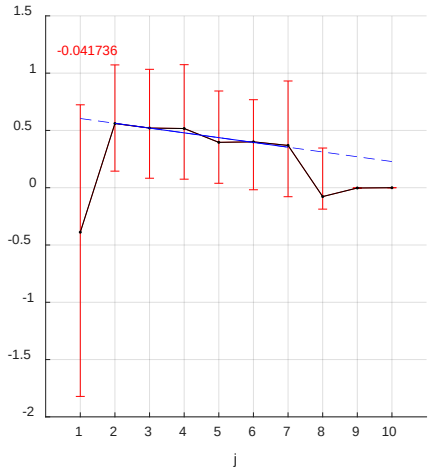

(e)

Figure 5-15: Cumulant graphs for levels 2-7 for the April 19, 2003 pipeline data. (a) c_1 (b) c_2 (c) c_3 (d) c_4 (e) c_5

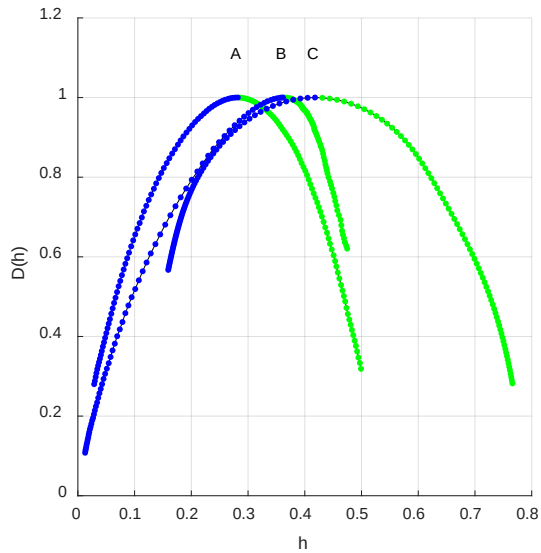

Figure 5-16: Median (a) shuffled and (b) IAAFT surrogate singularity spectrum graphs for the April 19, 2003 pipeline data with the (c) singularity spectrum of the original signal for comparison for levels 2-7. Positive q values are blue, negative q values are green.

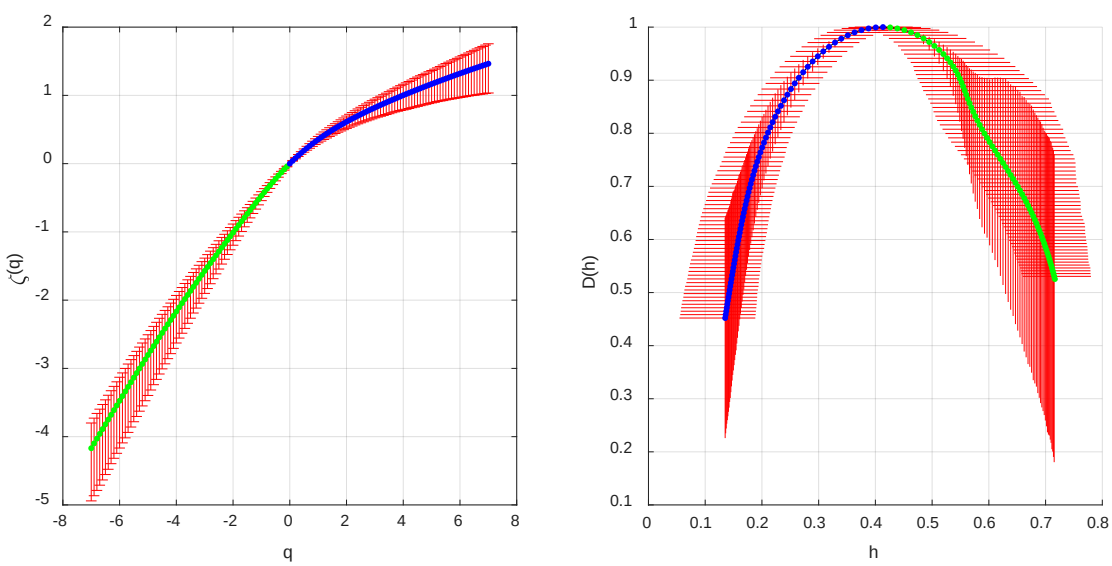

(a) (b)

Figure 5-17: (a) Scaling exponents and (b) singularity spectrum for the April 19, 2003 pipeline data for levels 3-8. Positive q values are blue, negative q values are green.

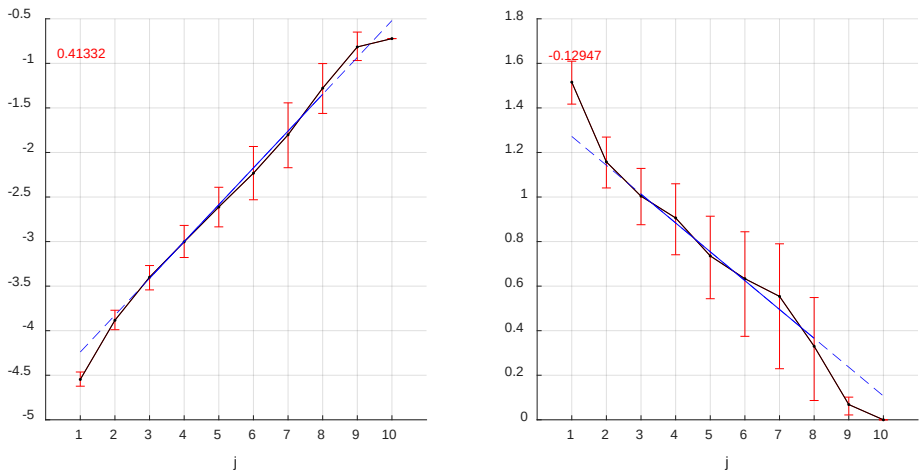

(a)

(b)

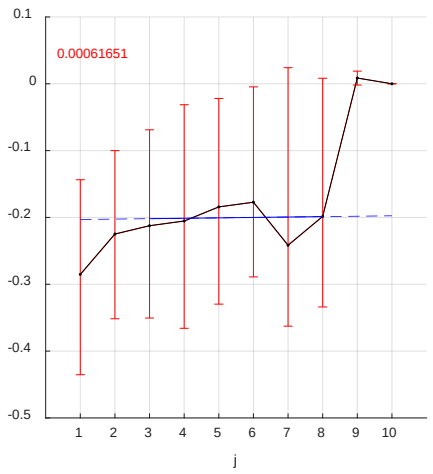

(c)

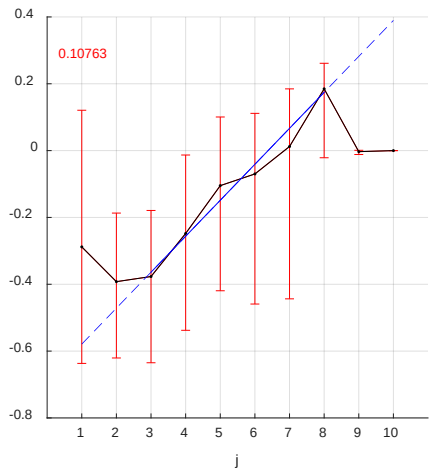

(d)

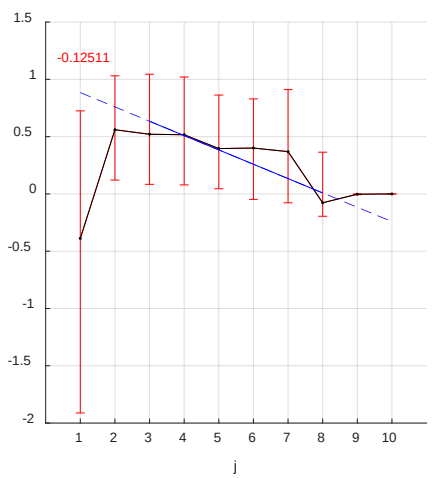

(e)

Figure 5-18: Cumulant graphs for levels 3-8 for the April 19, 2003 pipeline data. (a) c_1 (b) c_2 (c) c_3 (d) c_4 (e) c_5

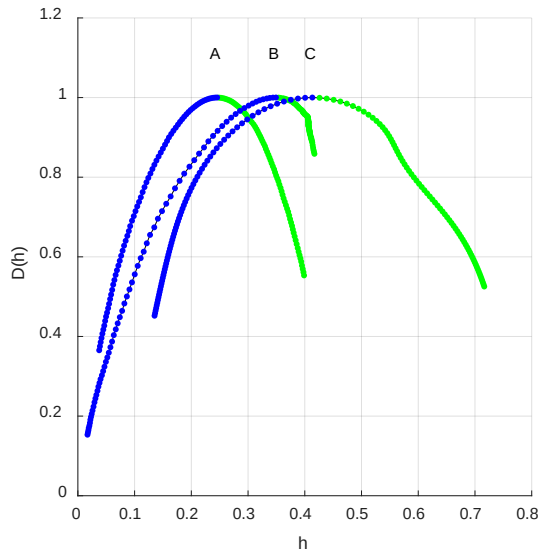

Figure 5-19: Median (a) shuffled and (b) IAAFT surrogate singularity spectrum graphs for the April 19, 2003 pipeline data with the (c) singularity spectrum of the original signal for comparison for levels 3-8. Positive q values are blue, negative q values are green.

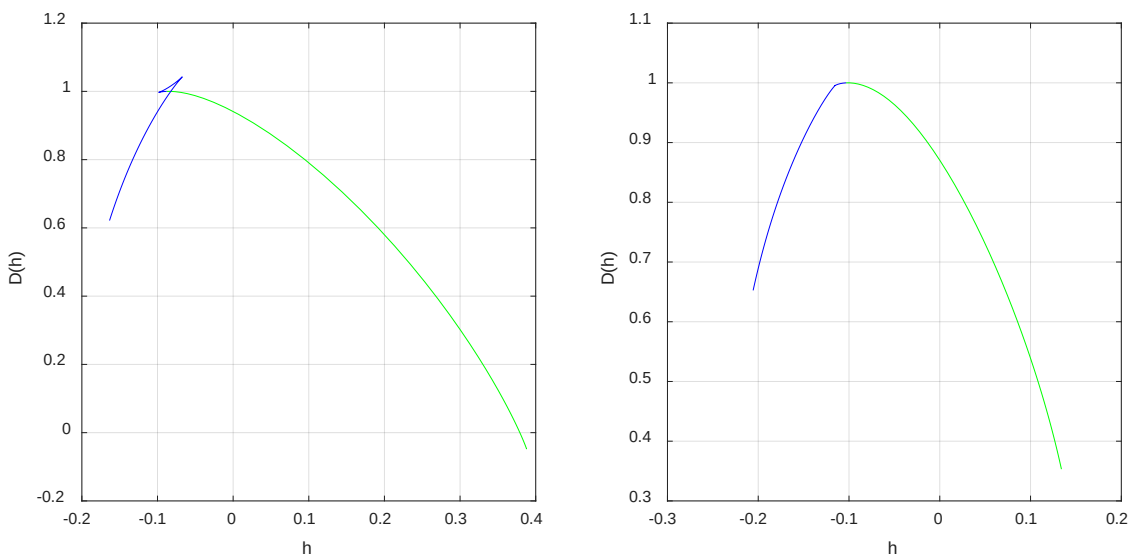

(a) (b)

Figure 5-20: Singularity spectrum generated by MFDFA for (a) M=0 levels 2-7 and (b) M=0, levels 3-8 of the April 19, 2003 pipeline data.

Table 5-15: Cumulant values for the April 19, 2003 pipeline data

	Levels 2-7				Levels 3-8			
Cumulant	**Value**	**STD**	**P-Value**	**Reject**	**Value**	**STD**	**P-Value**	**Reject**
c_1	0.42	0.03	0.002	1	0.41	0.03	0.002	1
c_2	-0.13	0.03	0.002	1	-0.13	0.03	0.002	1
c_3	0.00	0.02	0.609	0	0.00	0.02	0.687	0
c_4	0.09	0.04	0.062	1	0.11	0.03	0.008	1
c_5	-0.04	0.07	0.406	0	-0.13	0.06	0.068	1

Table 5-16: Shuffle cumulant values for the April 19, 2003 pipeline data for levels 2-7

		Mean										
	Actual	**Shuffle**		**Δ**							**P-**	
Cumulant	**Value**	**Value**	**STD**	**Value**	**Greater**		**Equal**		**Less**		**Value**	**Reject**
c_1	0.42	0.28	0.01	0.14	0	0.00%	0	0.00%	200	100.00%	0.000	1
c_2	-0.13	-0.04	0.00	-0.09	200	100.00%	0	0.00%	0	0.00%	0.000	1
c_3	0.00	-0.01	0.00	0.01	0	0.00%	0	0.00%	200	100.00%	0.000	1
c_4	0.09	0.00	0.00	0.09	0	0.00%	0	0.00%	200	100.00%	0.000	1
c_5	-0.04	0.00	0.00	-0.04	200	100.00%	0	0.00%	0	0.00%	0.000	1
Total Rejection:	5	100.00%										

Table 5-17: IAAFT cumulant values for the April 19, 2003 pipeline data for levels 2-7

		Mean										
	Actual	**IAAFT**		**Δ**							**P-**	
Cumulant	**Value**	**Value**	**STD**	**Value**	**Greater**		**Equal**		**Less**		**Value**	**Reject**
c_1	0.42	0.36	0.02	0.06	0	0.00%	0	0.00%	200	100.00%	0.000	1
c_2	-0.13	-0.04	0.01	-0.09	200	100.00%	0	0.00%	0	0.00%	0.000	1
c_3	0.00	-0.03	0.01	0.03	0	0.00%	0	0.00%	200	100.00%	0.000	1
c_4	0.09	-0.02	0.01	0.11	0	0.00%	0	0.00%	200	100.00%	0.000	1
c_5	-0.04	0.01	0.01	-0.05	200	100.00%	0	0.00%	0	0.00%	0.000	1
Total Rejection:	5	100.00%										

Table 5-18: Shuffle cumulant values for the April 19, 2003 pipeline data for levels 3-8

		Mean										
	Actual	**Shuffle**		**Δ**							**P-**	
Cumulant	**Value**	**Value**	**STD**	**Value**	**Greater**		**Equal**		**Less**		**Value**	**Reject**
c_1	0.41	0.25	0.01	0.16	0	0.00%	0	0.00%	200	100.00%	0.000	1
c_2	-0.13	-0.03	0.00	-0.10	200	100.00%	0	0.00%	0	0.00%	0.000	1
c_3	0.00	0.00	0.00	0.00	2	1.00%	0	0.00%	198	99.00%	0.010	1
c_4	0.11	0.00	0.00	0.11	0	0.00%	0	0.00%	200	100.00%	0.000	1
c_5	-0.13	0.00	0.00	-0.13	200	100.00%	0	0.00%	0	0.00%	0.000	1
Total Rejection:	5	100.00%										

Table 5-19: IAAFT cumulant values for the April 19, 2003 pipeline data for levels 3-8

Cumulant	Actual Value	Mean IAAFT Value	STD	Δ Value	Greater		Equal		Less		P-Value	Reject
c_1	0.41	0.35	0.02	0.06	0	0.00%	0	0.00%	200	100.00%	0	1
c_2	-0.13	-0.05	0.01	-0.08	200	100.00%	0	0.00%	0	0.00%	0	1
c_3	0.00	-0.03	0.01	0.03	0	0.00%	0	0.00%	200	100.00%	0	1
c_4	0.11	-0.01	0.01	0.12	0	0.00%	0	0.00%	200	100.00%	0	1
c_5	-0.13	0.02	0.01	-0.15	200	100.00%	0	0.00%	0	0.00%	0	1
Total Rejection:	5	100.00%										

5.1.3 February 8, 2003

The mean K_p index value for the day is 3.0875, which is near the median mean daily value K_p index value for 2003 of 3.0417, with the three hour values given in Figure 5-21. The current on the pipeline is shown in Figure 5-22 with a maximum positive value of 0.67 amps and a maximum negative value of -1.08 amps. The automated range selection algorithm gave the largest lambda value (354.126) for wavelet levels 2-6 as shown in Table 5-20 with the tightness of fit among the cumulants given in Figure 5-24. The statistical tests on the signal in Table 5-21 and the scaling exponents and singularity spectrum in Figure 5-23 show that the signal has multifractal characteristics. The surrogate data analysis in Figure 5-25 shows that the multifractal characteristics of the surrogate signals are different from the original signal. This is confirmed for all but the third cumulants in the shuffle data test in Table 5-22 and the IAAFT data test in Table 5-23. The MFDFA results displayed in Figure 5-26 shows a good approximation to the singularity spectrum for the positive q values selected, however we were unable to generate a singularity spectrum for the negative q values selected.

Table 5-20: Lambda values and classifications for all ranges for February 8, 2003 pipeline data.

j_1	j_2	Length	λ	Classification	r_1	r_2	r_3	r_4	r_5
2	6	5	354.126	Multifractal	1	1	0	1	0
5	8	4	349.823	Monofractal	1	0	0	0	0
5	9	5	347.224	Multifractal	1	1	0	0	0
4	9	6	342.826	Multifractal	1	1	0	0	0
2	5	4	339.582	Multifractal	1	1	0	1	1
7	9	3	337.665	Multifractal	1	1	0	0	0
3	6	4	335.703	Multifractal	1	1	0	0	0
4	8	5	332.678	Multifractal	1	1	0	0	0
3	9	7	327.589	Multifractal	1	1	0	0	0
3	5	3	326.365	Multifractal	1	1	0	0	0
3	8	6	321.563	Multifractal	1	1	0	0	0
2	9	8	319.594	Multifractal	1	1	0	1	0
6	9	4	319.459	Multifractal	1	1	0	0	0
4	6	3	314.215	Multifractal	1	1	0	0	0
2	8	7	313.696	Multifractal	1	1	0	1	1
6	8	3	297.925	Monofractal	1	0	0	0	0
3	7	5	296.498	Multifractal	1	1	0	0	0
2	7	6	296.156	Multifractal	1	1	0	1	0
7	10	4	282.705	Multifractal	1	1	1	0	0
4	7	4	280.699	Multifractal	1	1	0	0	0
1	6	6	275.135	Multifractal	1	1	0	1	0
2	4	3	272.254	Multifractal	1	1	0	1	0
5	7	3	266.299	Monofractal	1	0	0	0	0
1	5	5	258.699	Multifractal	1	1	1	1	0
1	9	9	258.055	Multifractal	1	1	1	1	0
2	10	9	256.504	Multifractal	1	1	0	1	0
4	10	7	254.971	Multifractal	1	1	0	0	0
3	10	8	249.883	Multifractal	1	1	0	0	0
5	10	6	249.756	Multifractal	1	1	0	0	0
1	8	8	249.013	Multifractal	1	1	1	1	0
6	10	5	247.369	Multifractal	1	1	0	0	0
8	10	3	245.793	Multifractal	0	1	0	0	0
1	4	4	242.499	Multifractal	1	1	1	1	0
1	7	7	236.666	Multifractal	1	1	1	1	0
1	3	3	225.691	Multifractal	1	1	1	0	0
1	10	10	218.982	Multifractal	1	1	0	1	0

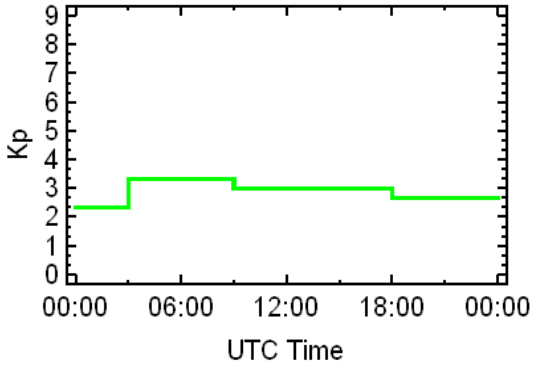

Figure 5-21: K_p index for February 8, 2003.

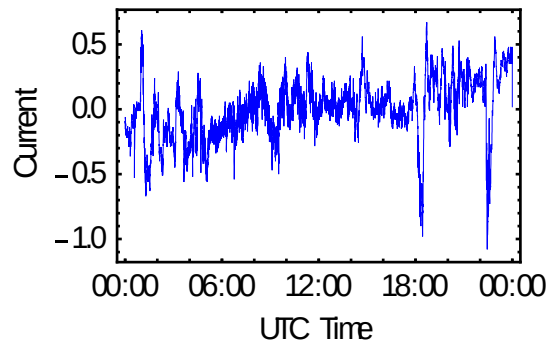

Figure 5-22: Pipeline data for February 8, 2003.

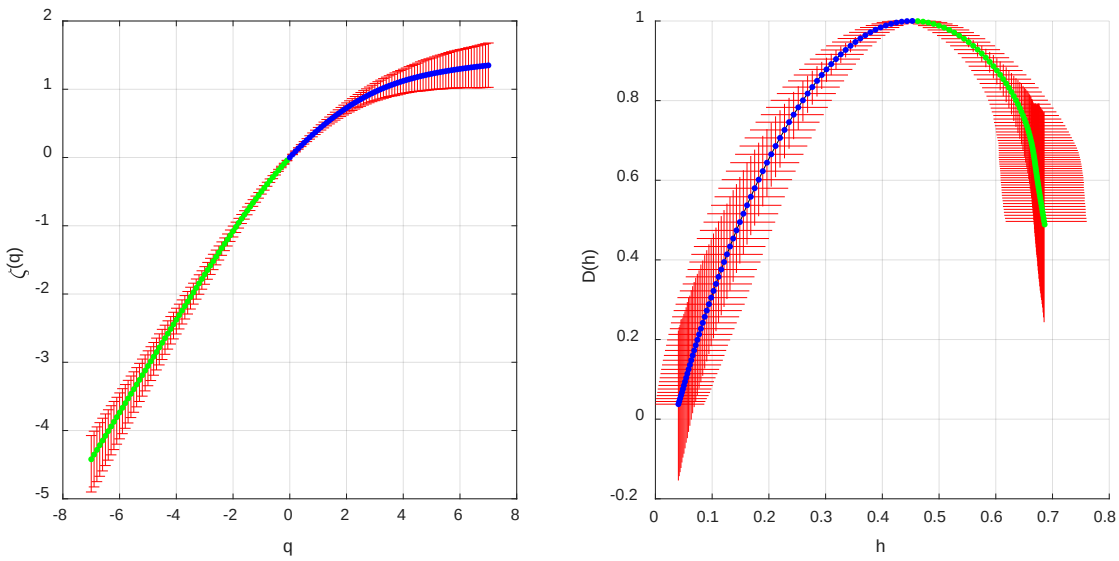

(a) (b)

Figure 5-23: (a) Scaling exponents and (b) singularity spectrum for the February 8, 2003 pipeline data for levels 2-6. Positive q values are blue, negative q values are green.

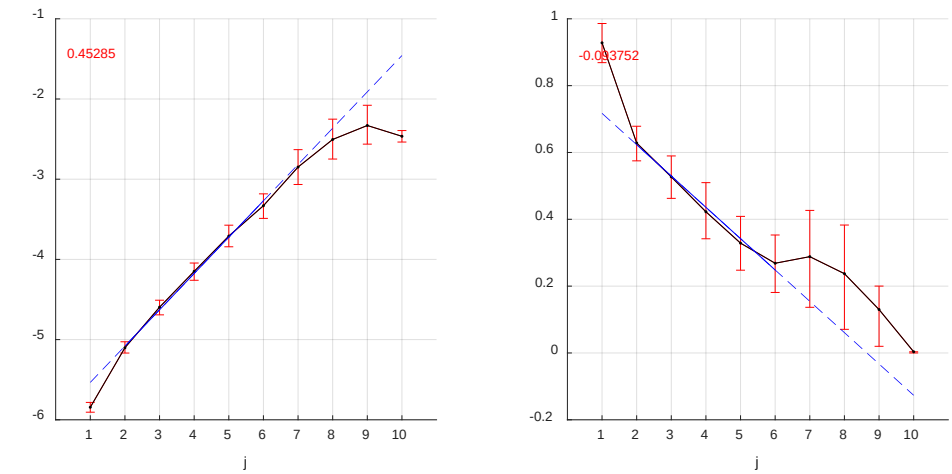

(a)

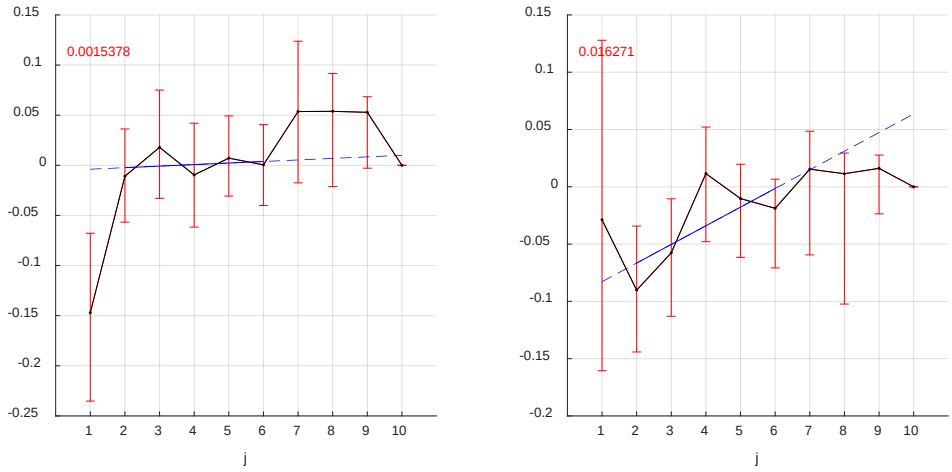

(b)

(c)

(d)

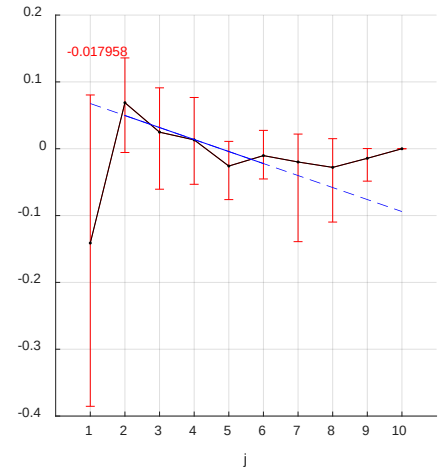

(e)

Figure 5-24: Cumulant graphs for levels 2-6 of the February 8, 2003 pipeline data. (a) c_1 (b) c_2 (c) c_3 (d) c_4 (e) c_5

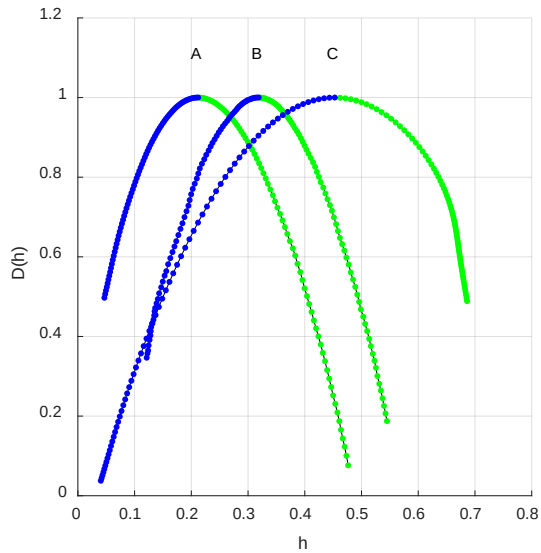

Figure 5-25: Median (a) shuffled and (b) IAAFT surrogate singularity spectrum graphs for February 8, 2003 data with the (c) singularity spectrum of the original signal for comparison for levels 2-6. Positive q values are blue, negative q values are green.

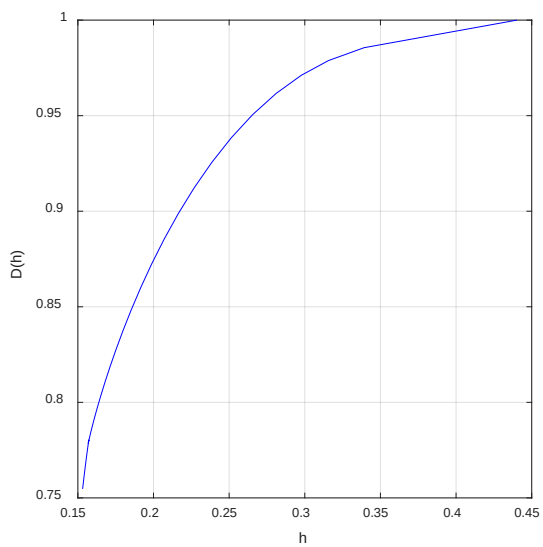

Figure 5-26: Singularity spectrum generated by MFDFA for levels 2-6 for the February 8, 2003 pipeline data, M=2, spectrum matches positive q values, negative ones were not generated

Table 5-21: Cumulant values for the February 8, 2003 pipeline data

Cumulant	Value	STD	P-Value	Reject
c_1	0.45	0.02	0.002	1
c_2	-0.09	0.01	0.002	1
c_3	0.00	0.01	0.813	0
c_4	0.02	0.01	0.102	0
c_5	-0.02	0.01	0.126	0

Table 5-22: Shuffle cumulant values for the February 8, 2003 pipeline data

Cumulant	Actual Value	Mean Shuffle Value	STD	Δ Value	Greater		Equal		Less		P-Value	Reject
c_1	0.45	0.21	0.01	0.24	0	0.00%	0	0.00%	200	100.00%	0.000	1
c_2	-0.09	-0.03	0.00	-0.06	200	100.00%	0	0.00%	0	0.00%	0.000	1
c_3	0.00	0.00	0.00	0.00	118	59.00%	0	0.00%	82	41.00%	0.410	0
c_4	0.02	0.00	0.00	0.02	0	0.00%	0	0.00%	200	100.00%	0.000	1
c_5	-0.02	0.00	0.00	-0.02	200	100.00%	0	0.00%	0	0.00%	0.000	1
Total Rejection:	4	80.00%										

Table 5-23: IAAFT cumulant values for the February 8, 2003 pipeline data

Cumulant	Actual Value	Mean IAAFT Value	STD	Δ Value	Greater		Equal		Less		P-Value	Reject
c_1	0.45	0.32	0.02	0.13	0	0.00%	0	0.00%	200	100.00%	0.000	1
c_2	-0.09	-0.03	0.01	-0.06	200	100.00%	0	0.00%	0	0.00%	0.000	1
c_3	0.00	0.00	0.01	0.00	87	43.50%	0	0.00%	113	56.50%	0.435	0
c_4	0.02	0.00	0.01	0.02	0	0.00%	0	0.00%	200	100.00%	0.000	1
c_5	-0.02	0.00	0.00	-0.02	200	100.00%	0	0.00%	0	0.00%	0.000	1
Total Rejection:	4	80.00%										

5.1.4 April 24, 2003

The mean K_p index value for the day is 3.8375, which is the 75 percentile of the total K_p index value for 2003, with the three-hour values given in Figure 5-27. The GIC of the pipeline is shown in Figure 5-28 with a maximum positive value of 1.87 amps and a maximum negative value of -1.71 amps. The automated range selection algorithm had the largest lambda value (401.378) for wavelet levels 3-7 which gave a multifractal response as shown in Table 5-24 with the tightness of the fit in the cumulant graphs given in Figure 5-30. The scaling exponents and singularity spectrum in Figure 5-29 and the statistical tests in Table 5-25 show that the signal has clear multifractal characteristics. The surrogate data analysis in Figure 5-31 show clear differences in the multifractal characteristics of the signal with this being confirmed for all cumulants for the shuffled data test in Table 5-26 and for cumulants c_1, c_2, and c_4 in the IAAFT data test in Table 5-27. MFDFA analysis for levels 3-7 generated a good singularity spectrum as shown in Figure 5-32. The difference between that one and the one generated by the wavelet leader is that the apex of the parabola for MFDFA is at 0.2 and the apex of the parabola for the

wavelet leader method is at 0.37. Also, the MFDFA singularity spectrum is slightly wider and more symmetrical.

Table 5-24: Lambda values and classifications for all ranges for April 24, 2003 pipeline data.

j_1	j_2	Length	λ	Classification	r_1	r_2	r_3	r_4	r_5
3	7	5	401.378	Multifractal	1	1	0	0	0
3	6	4	391.617	Multifractal	1	1	0	0	0
4	7	4	391.525	Monofractal	1	0	0	0	0
4	6	3	379.018	Monofractal	1	0	0	0	0
3	5	3	373.155	Monofractal	1	0	0	0	0
4	8	5	355.926	Multifractal	1	1	0	0	0
2	7	6	352.07	Multifractal	1	1	0	0	0
5	8	4	347.834	Monofractal	1	0	0	0	0
5	7	3	337.716	Monofractal	1	0	0	0	0
2	6	5	333.585	Multifractal	1	1	0	0	0
3	9	7	331.13	Multifractal	1	1	1	0	0
2	8	7	328.048	Multifractal	1	1	0	0	0
2	9	8	327.03	Multifractal	1	1	1	1	1
4	9	6	324.173	Multifractal	1	1	1	0	0
2	5	4	315.443	Multifractal	1	1	0	0	0
5	9	5	307.563	Multifractal	1	1	1	0	0
3	8	6	297.005	Multifractal	1	1	0	0	0
6	8	3	293.522	Monofractal	1	0	0	0	0
1	7	7	281.857	Multifractal	1	1	0	0	0
1	6	6	280.262	Multifractal	1	1	0	0	0
6	9	4	280.193	Multifractal	1	1	0	0	0
1	8	8	276.956	Multifractal	1	1	0	0	0
2	4	3	272.705	Multifractal	1	1	0	0	0
1	5	5	262.045	Multifractal	1	1	0	0	0
1	4	4	258.447	Multifractal	1	1	0	0	0
1	9	9	255.408	Multifractal	1	1	1	0	1
1	3	3	251.433	Multifractal	1	1	1	0	1
7	9	3	249.343	Multifractal	1	1	0	0	0
3	10	8	45.268	Monofractal	1	0	0	0	0
6	10	5	45.069	Monofractal	1	0	0	0	0
1	10	10	44.995	Monofractal	1	0	0	0	0
2	10	9	44.964	Monofractal	1	0	0	0	0
4	10	7	44.914	Monofractal	1	0	0	0	0
5	10	6	44.766	Monofractal	1	0	0	0	0
7	10	4	44.491	Monofractal	1	0	0	0	0
8	10	3	43.927	Monofractal	1	0	0	0	0

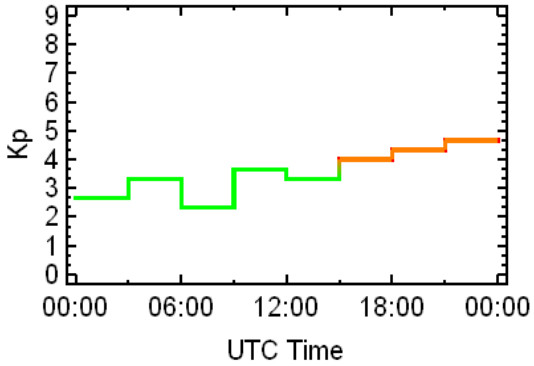

Figure 5-27: K_p index for April 24, 2003.

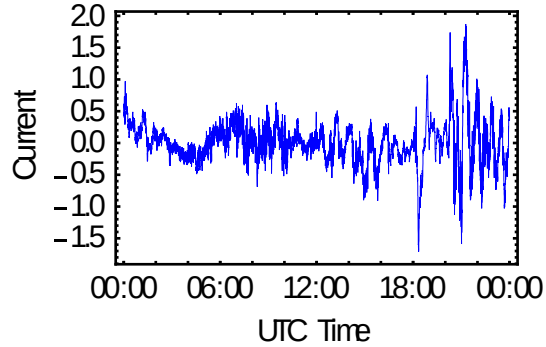

Figure 5-28: Pipeline data for April 24, 2003**.**

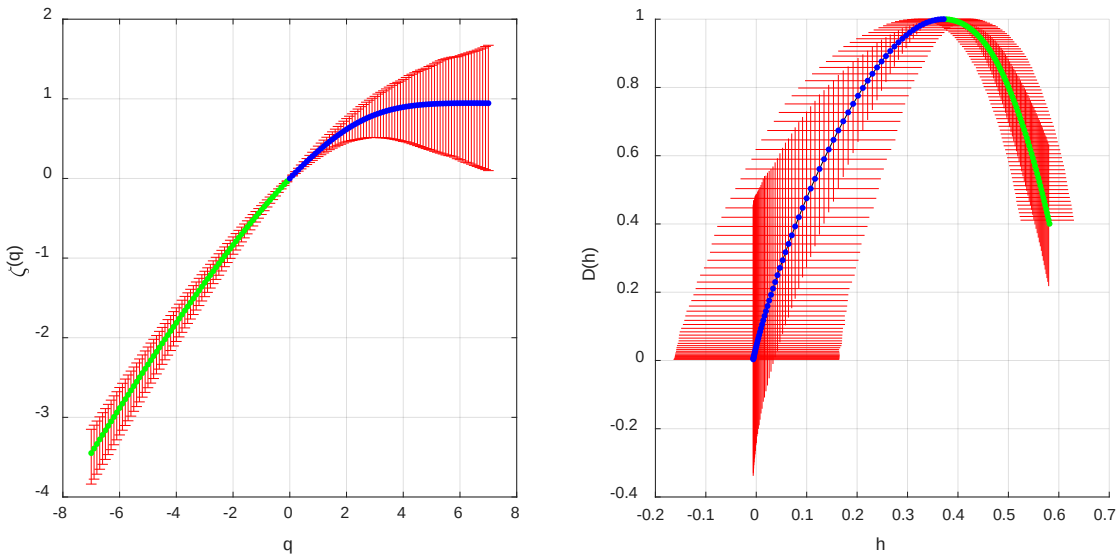

(a) (b)

Figure 5-29: (a) Scaling exponents, (b) singularity spectrum for April 24, 2003 pipeline data with the singularity spectrum of the original signal for comparison for levels 3-7. Positive q values are blue, negative q values are green.

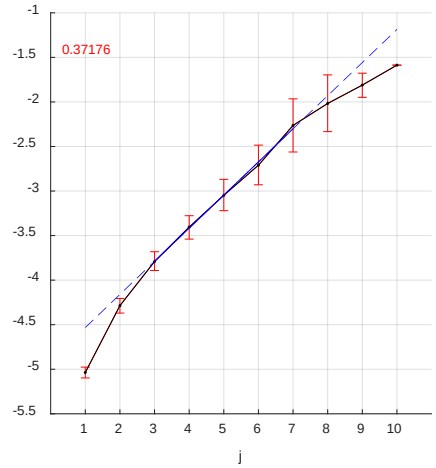

(a)

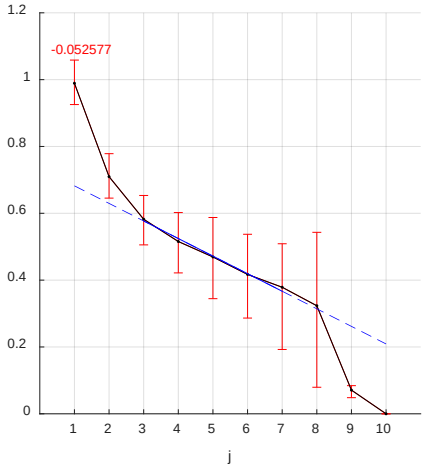

(b)

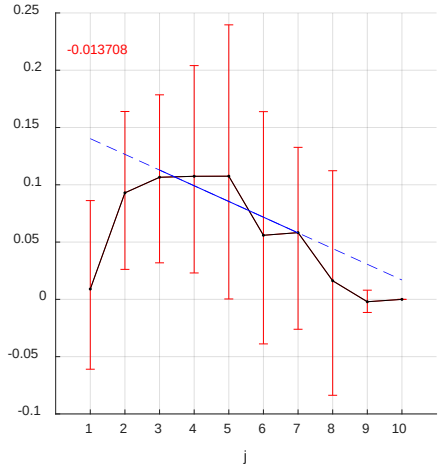

(d)

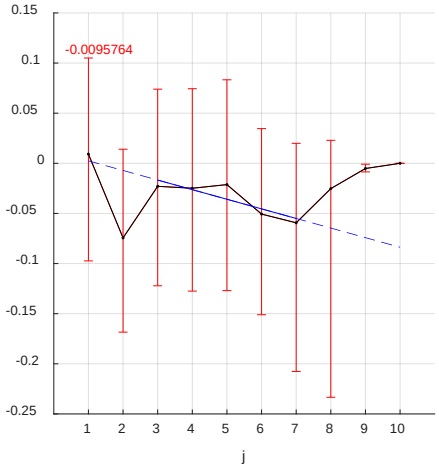

(d)

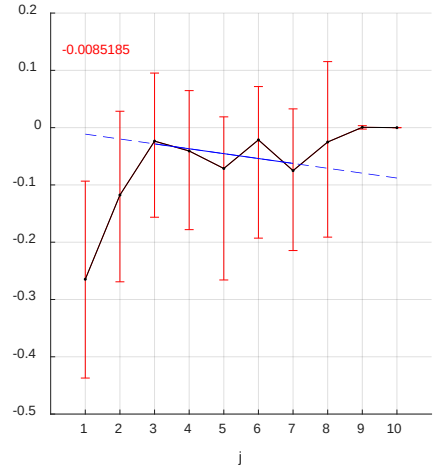

(e)

Figure 5-30: Cumulant graphs for levels 3-7 for the April 24, 2003 pipeline data. (a) c_1 (b) c_2 (c) c_3 (d) c_4 (e) c_5

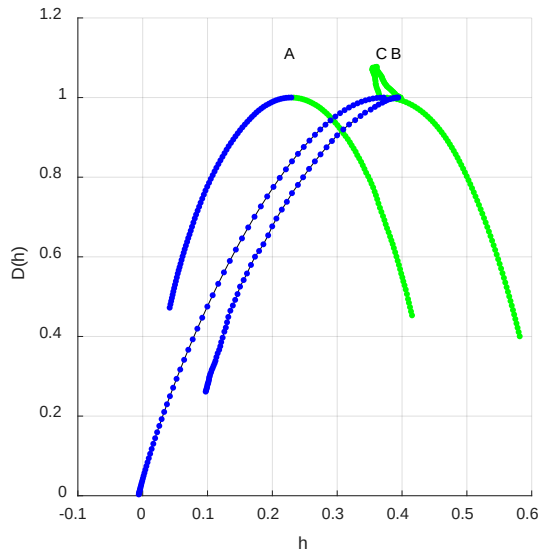

Figure 5-31: Median (a) shuffled and (b) IAAFT surrogate singularity spectrum graphs for April 24, 2003 data with the (c) singularity spectrum of the original signal for comparison for levels 3-7. Positive q values are blue, negative q values are green.

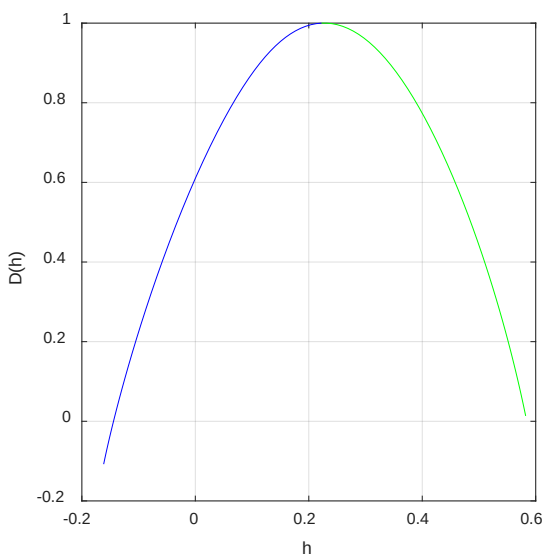

Figure 5-32: Singularity spectrum generated by MFDFA for levels 3-7 of the April 24, 2003 pipeline data. M = 3

Table 5-25: Cumulant values for April 24, 2003 pipeline data

Cumulant	Value	STD	P-Value	Reject
c_1	0.37	0.04	0.002	1
c_2	-0.05	0.02	0.008	1
c_3	-0.01	0.02	0.310	0
c_4	-0.01	0.02	0.609	0
c_5	-0.01	0.03	0.819	0

Table 5-26: Shuffle cumulant values for the April 24, 2003 pipeline data

Cumulant	Actual Value	Mean Shuffle Value	STD	Δ Value	Greater		Equal		Less		P-Value	Reject
c_1	0.37	0.23	0.01	0.14	0	0.00%	0	0.00%	200	100.00%	0.000	1
c_2	-0.05	-0.04	0.00	-0.01	200	100.00%	0	0.00%	0	0.00%	0.000	1
c_3	-0.01	0.00	0.00	-0.01	200	100.00%	0	0.00%	0	0.00%	0.000	1
c_4	-0.01	0.00	0.00	-0.01	200	100.00%	0	0.00%	0	0.00%	0.000	1
c_5	-0.01	0.00	0.00	-0.01	200	100.00%	0	0.00%	0	0.00%	0.000	1
Total Rejection: 5			100.00%									

Table 5-27: IAAFT cumulant values for the April 24, 2003 pipeline data

Cumulant	Actual Value	Mean IAAFT Value	STD	Δ Value	Greater		Equal		Less		P-Value	Reject
c_1	0.37	0.39	0.03	-0.02	156	78.00%	0	0.00%	44	22.00%	0.220	0
c_2	-0.05	-0.02	0.02	-0.03	197	98.50%	0	0.00%	3	1.50%	0.015	1
c_3	-0.01	-0.04	0.02	0.03	13	6.50%	0	0.00%	187	93.50%	0.065	1
c_4	-0.01	-0.02	0.02	0.01	33	16.50%	0	0.00%	167	83.50%	0.165	0
c_5	-0.01	0.02	0.02	-0.03	192	96.00%	0	0.00%	8	4.00%	0.040	1
Total Rejection: 3			60.00%									

5.1.5 October 29, 2003

The next three days are the Halloween storm of 2003. We start with October 29, 2003, which has a mean K_p index for the day of 7.2875, which is the maximum for 2003. The three-hour K_p values in Figure 5-33 show a dramatic increase to nine at 9:00 AM UTC, which indicates a severe storm. The GIC on the pipeline in Figure 5-34 shows significant current spikes with a maximum positive current of 51.48 amps and a maximum negative current of -57.05 amps. The automated range selection algorithm calculated that levels 4-6 had the highest lambda value of 409.483 as shown in Table 5-28 with the tightness of fit shown in Figure 5-36. The scaling exponents and singularity spectrum in Figure 5-35 and statistical tests in Table 5-29 show monofractal characteristics for levels 4-6. For this signal, the adjacent range of levels 6-8 also shows signs of a monofractal signal with a lambda value of 363.369 and the tightness of fit shown in Figure 5-39. The singularity spectrum is shown in Figure 5-40 and the results of the statistical tests are in Table 5-29. In this case, the c_1 cumulant of the level 6-8 singularity spectrum has been shifted to 0.59, with the c_1 cumulant of the level 4-6 singularity spectrum at 0.43, similar to the previous signals. The graphs of the surrogate spectrum in Figures 5-37 and 5-41 and the statistical tests in Tables 5-30 to 5-33 show that the surrogate signals differ from the

original signal for both levels 4-6 and levels 6-8 for all cumulant values. The MFDFA results displayed in Figure 5-38 show a singularity spectrum that is somewhat similar to the wavelet leader analysis for the selected positive q values and the results displayed in Figure 5-42 show a singularity spectrum that is very different from the wavelet leader analysis. The apex of the singularity spectrum for the MFDFA analysis for levels 4-6 is near the 0.43 apex of the singularity spectrum for the wavelet leader analysis for a polynomial trend suppression of 3 with a truncated negative q spectrum that is similar to that generated by the wavelet leader method.

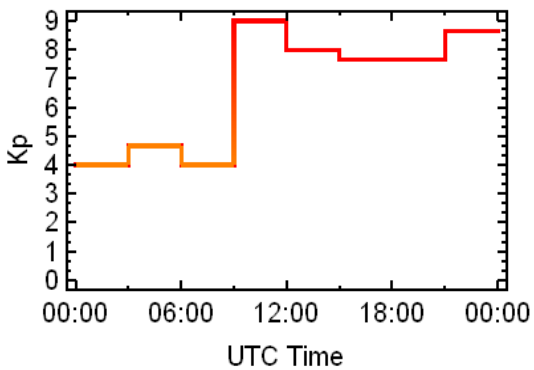

Figure 5-33: K_p index for October 29, 2003.

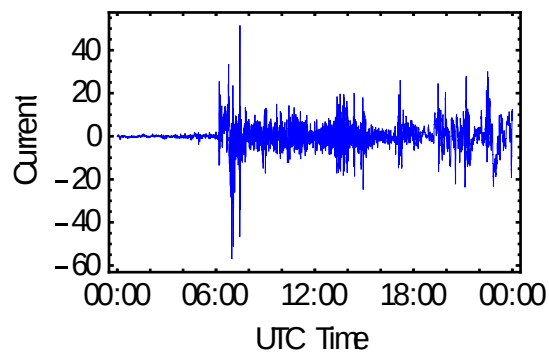

Figure 5-34: Pipeline data for October 29, 2003.

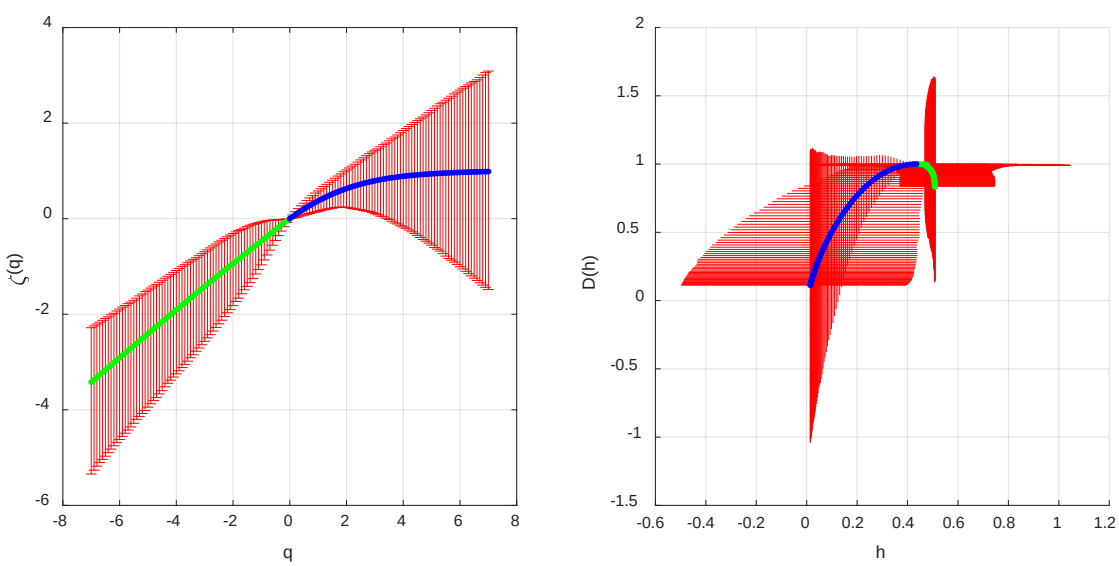

(a) (b)

Figure 5-35: (a) Scaling exponents, (b) singularity spectrum for October 29, 2003 pipeline data for levels 4-6. Positive q values are blue, negative q values are green.

Table 5-28: Lambda values and classifications for all ranges for October 29, 2003 pipeline data.

j_1	j_2	Length	λ	Classification	r_1	r_2	r_3	r_4	r_5
4	6	3	409.483	Monofractal	1	0	0	0	0
3	5	3	377.241	Monofractal	1	0	0	0	0
3	6	4	373.539	Monofractal	1	0	0	0	0
5	7	3	368.256	Monofractal	1	0	0	0	0
6	8	3	363.369	Monofractal	1	0	0	0	0
5	8	4	353.182	Monofractal	1	0	0	0	0
2	7	6	346.240	Multifractal	1	0	1	0	0
2	5	4	345.919	Multifractal	1	0	1	0	0
4	7	4	341.289	Monofractal	1	0	0	0	0
2	6	5	337.782	Multifractal	1	0	1	0	0
3	7	5	329.894	Monofractal	1	0	0	0	0
2	4	3	326.237	Multifractal	1	0	1	0	0
2	8	7	324.792	Multifractal	1	1	0	0	0
1	8	8	321.012	Multifractal	1	1	1	0	1
1	4	4	314.666	Multifractal	1	0	1	0	1
1	7	7	310.273	Multifractal	1	0	1	0	1
6	9	4	309.970	Multifractal	1	1	1	0	1
1	3	3	309.225	Multifractal	1	0	1	0	1
1	5	5	307.917	Multifractal	1	0	1	0	1
3	8	6	300.544	Multifractal	1	1	0	0	0
1	6	6	297.853	Multifractal	1	0	1	0	1
7	9	3	295.552	Multifractal	1	1	1	0	0
5	9	5	274.620	Multifractal	1	1	1	0	1
4	8	5	264.875	Multifractal	1	1	0	0	0
4	9	6	235.165	Multifractal	1	1	1	0	1
1	9	9	234.058	Multifractal	1	1	1	1	1
2	9	8	226.550	Multifractal	1	1	1	1	1
3	9	7	196.298	Multifractal	1	1	1	1	1
6	10	5	290.131	Multifractal	1	1	0	0	0
7	10	4	270.580	Multifractal	1	1	0	0	0
5	10	6	250.500	Multifractal	1	1	0	0	0
1	10	10	243.746	Multifractal	1	1	1	1	0
8	10	3	221.641	Monofractal	1	0	0	0	0
2	10	9	215.917	Multifractal	1	1	1	0	0
4	10	7	203.070	Multifractal	1	1	1	0	0
3	10	8	187.713	Multifractal	1	1	1	0	0

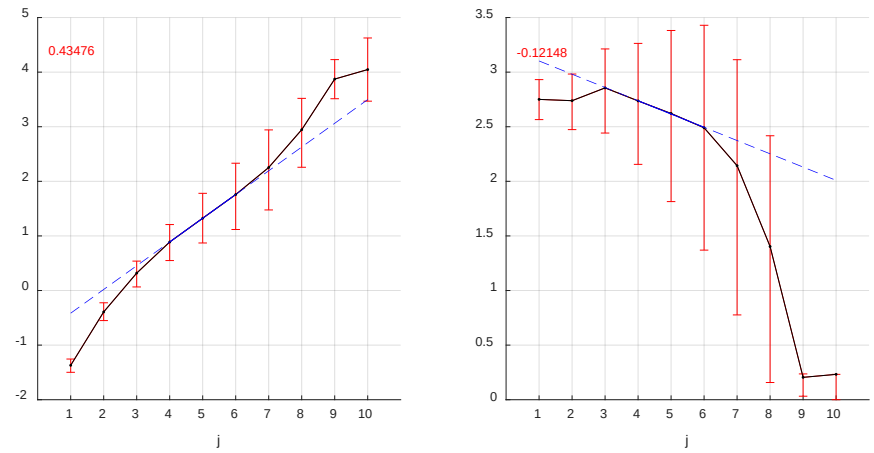

(a)

(b)

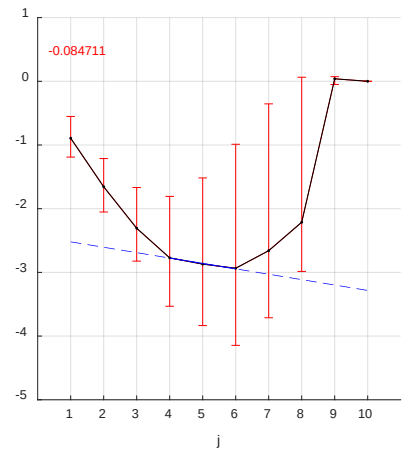

(c)

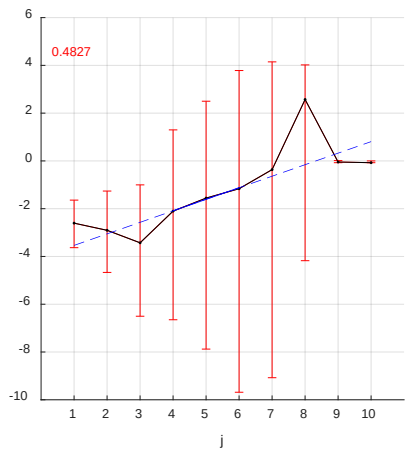

(d)

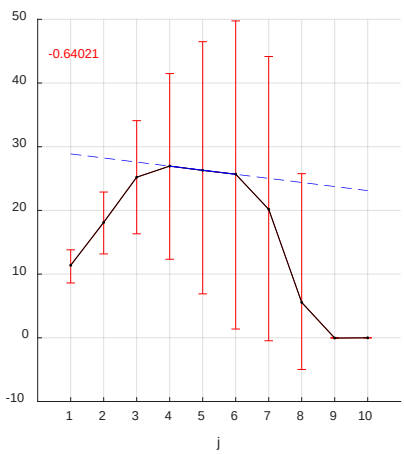

(e)

Figure 5-36: Cumulant graphs for levels 4-6 for the October 29, 2003 pipeline data. (a) c_1 (b) c_2 (c) c_3 (d) c_4 (e) c_5

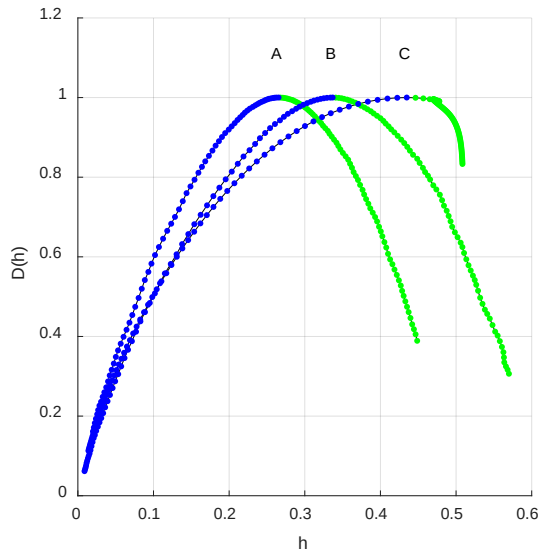

Figure 5-37: Median (a) shuffled and (b) IAAFT surrogate singularity spectrum graphs for October 29, 2003 pipeline data with the (c) singularity spectrum of the original signal for comparison for levels 4-6. Positive q values are blue, negative q values are green.

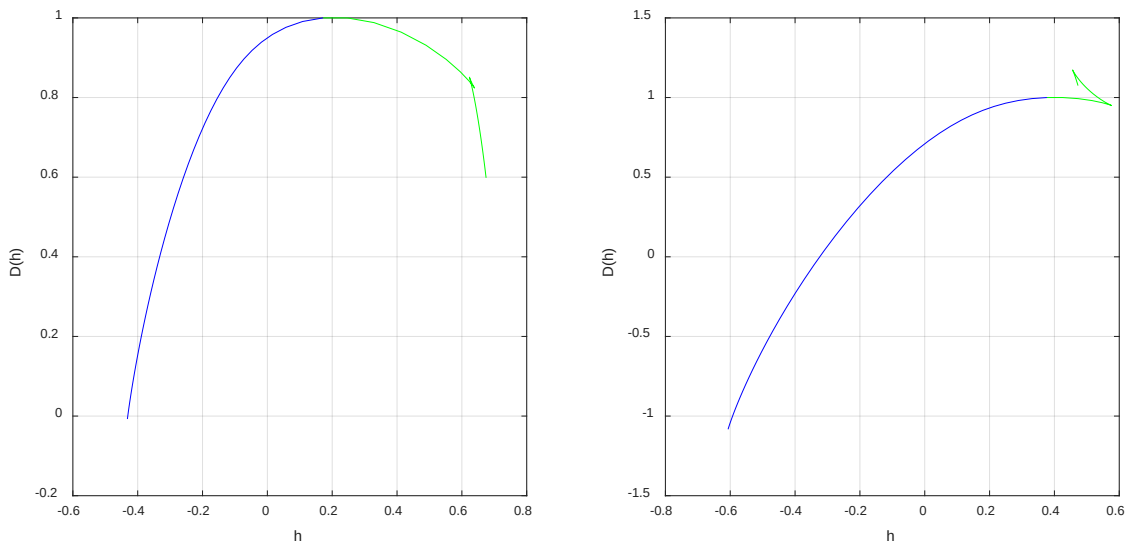

(a) (b)

Figure 5-38: Singularity spectrum generated by MFDFA for levels 4-6 (a) M=2 (b) M=3. Positive q values are blue, negative q values are green.

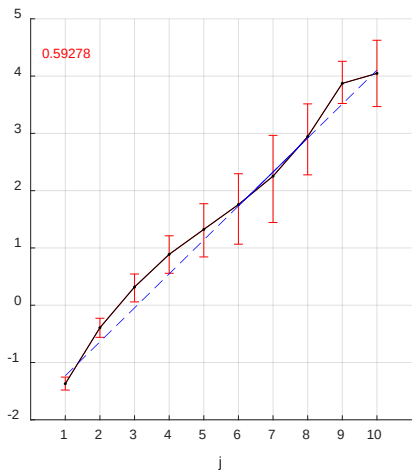

(a)

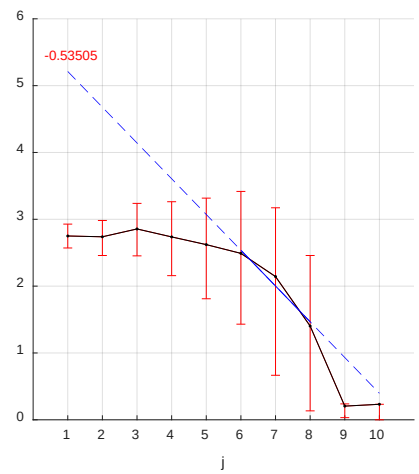

(b)

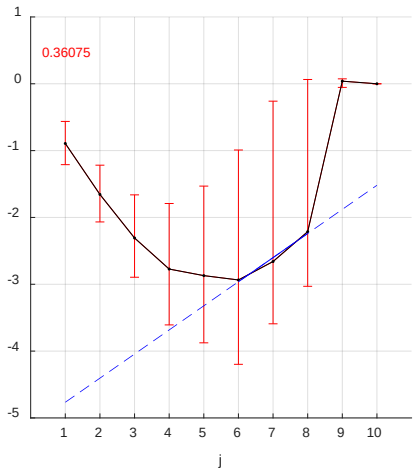

(c)

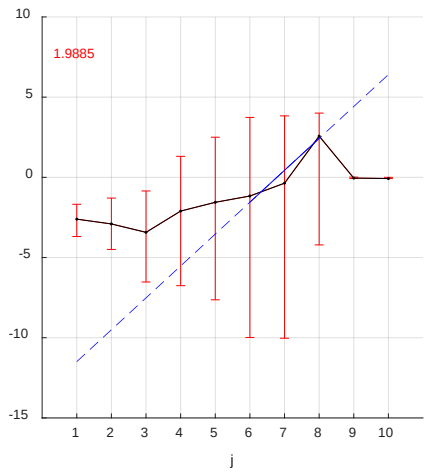

(d)

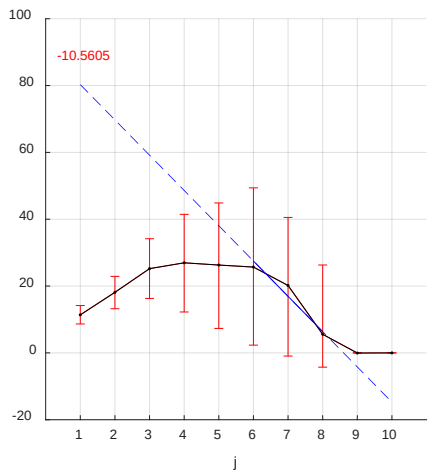

(e)

Figure 5-39: Cumulant graphs for levels 6-8 of the pipeline signal for October 29, 2009. (a) c_1 (b) c_2 (c) c_3 (d) c_4 (e) c_5

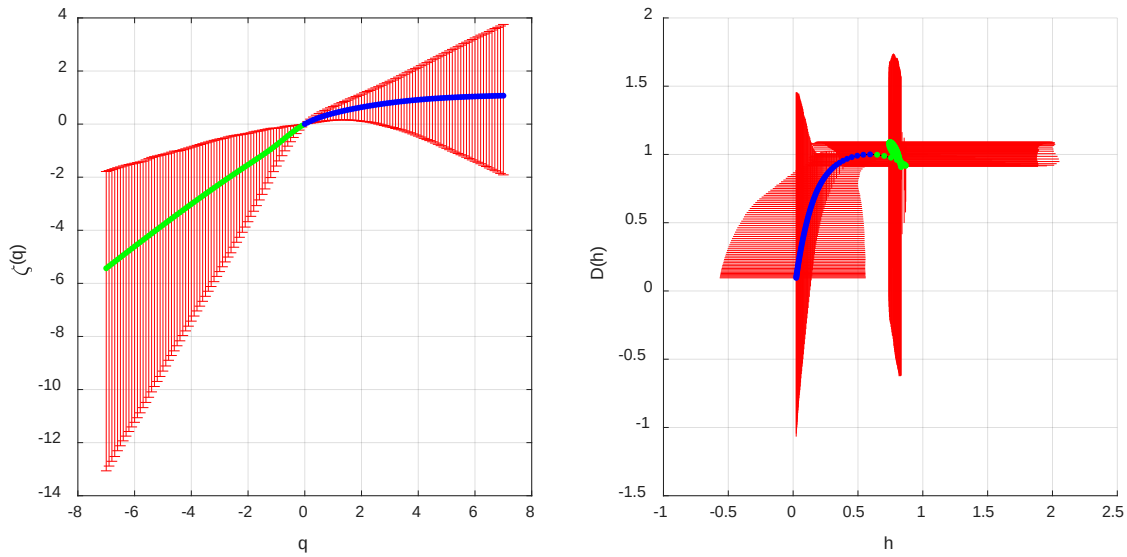

(a) (b)

Figure 5-40: (a) Scaling exponents and (b) singularity spectrum graphs for the October 29, 2003 pipeline data, levels 6-8. Positive q values are blue, negative q values are green.

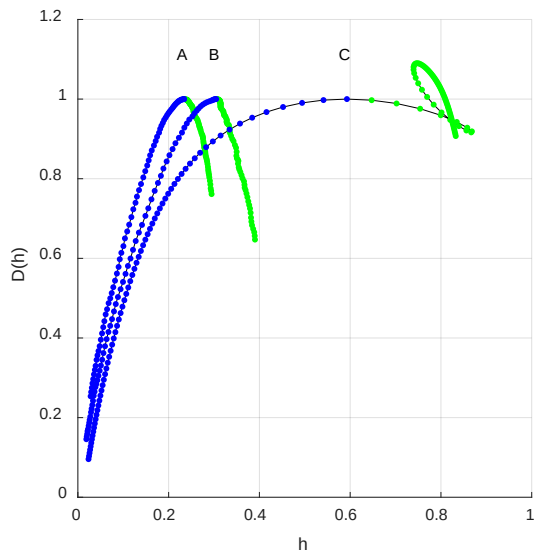

Figure 5-41: Median (a) shuffled and (b) IAAFT surrogate singularity spectrum graphs for the October 29, 2003 pipeline data with the (c) singularity spectrum of the original signal for comparison for levels 6-8. Positive q values are blue, negative q values are green.

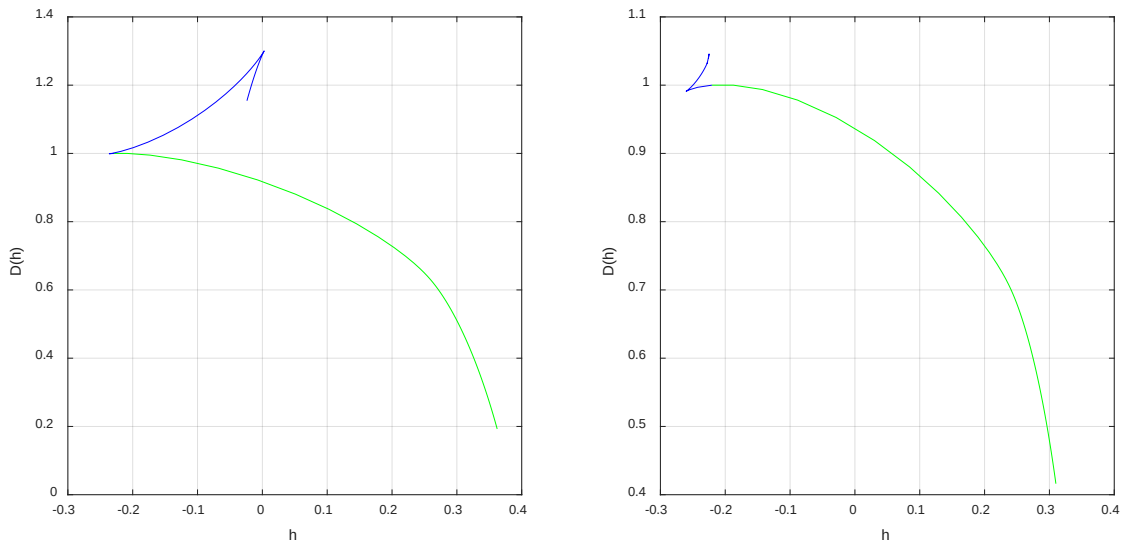

(a) (b)

Figure 5-42: Singularity spectrum generated by MFDFA for levels 6-8 for the October 29, 2003 pipeline data (a) M=2 (b) M=3. Positive q values are blue, negative q values are green.

Table 5-29: Cumulant values for October 29, 2003 pipeline data

	Levels 4-6				Levels 6-8			
Cumulant	**Value**	**STD**	**P-Value**	**Reject**	**Value**	**STD**	**P-Value**	**Reject**
c_1	0.43	0.20	0.042	1	0.59	0.26	0.028	1
c_2	-0.12	0.33	0.695	0	-0.54	0.46	0.224	0
c_3	-0.08	0.51	0.969	0	0.36	0.69	0.531	0
c_4	0.48	2.34	0.907	0	1.99	2.32	0.492	0
c_5	-0.64	8.26	0.849	0	-10.56	8.73	0.348	0

Table 5-30: Shuffle cumulant values for October 29, 2003 pipeline data for levels 4-6

	Actual	**Mean Shuffle**									**P-**	
Cumulant	**Value**	**Value**	**STD**	**Δ Value**	**Greater**		**Equal**		**Less**		**Value**	**Reject**
c_1	0.43	0.27	0.01	0.16	0	0.00%	0	0.00%	200	100.00%	0.000	1
c_2	-0.12	-0.03	0.01	-0.09	200	100.00%	0	0.00%	0	0.00%	0.000	1
c_3	-0.08	0.00	0.00	-0.08	200	100.00%	0	0.00%	0	0.00%	0.000	1
c_4	0.48	0.00	0.00	0.48	0	0.00%	0	0.00%	200	100.00%	0.000	1
c_5	-0.64	0.00	0.01	-0.64	200	100.00%	0	0.00%	0	0.00%	0.000	1
Total Rejection: 5			100.00%									

Table 5-31: IAAFT cumulant values for October 29, 2003 pipeline data for levels 4-6

Cumulant	Actual Value	Mean IAAFT Value	STD	Δ Value	Greater		Equal		Less		P-Value	Reject
c_1	0.43	0.34	0.02	0.09	0	0.00%	0	0.00%	200	100.00%	0.000	1
c_2	-0.12	-0.04	0.01	-0.08	200	100.00%	0	0.00%	0	0.00%	0.000	1
c_3	-0.08	0.00	0.01	-0.08	200	100.00%	0	0.00%	0	0.00%	0.000	1
c_4	0.48	-0.01	0.01	0.49	0	0.00%	0	0.00%	200	100.00%	0.000	1
c_5	-0.64	-0.01	0.01	-0.63	200	100.00%	0	0.00%	0	0.00%	0.000	1
Total Rejection: 5			100.00%									

Table 5-32: Shuffle cumulant values for October 29, 2003 pipeline data for levels 6-8

Cumulant	Actual Value	Mean Shuffle Value	STD	Δ Value	Greater		Equal		Less		P-Value	Reject
c_1	0.59	0.23	0.04	0.36	0	0.00%	0	0.00%	200	100.00%	0.000	1
c_2	-0.54	-0.01	0.01	-0.53	200	100.00%	0	0.00%	0	0.00%	0.000	1
c_3	0.36	-0.01	0.01	0.37	0	0.00%	0	0.00%	200	100.00%	0.000	1
c_4	1.99	-0.01	0.01	2.00	0	0.00%	0	0.00%	200	100.00%	0.000	1
c_5	-10.56	0.00	0.01	-10.56	200	100.00%	0	0.00%	0	0.00%	0.000	1
Total Rejection: 5			100.00%									

Table 5-33: IAAFT cumulant values for October 29, 2003 pipeline data for levels 6-8

Cumulant	Actual Value	Mean IAAFT Value	STD	Δ Value	Greater		Equal		Less		P-Value	Reject
c_1	0.59	0.30	0.05	0.29	0	0.00%	0	0.00%	200	100.00%	0	1
c_2	-0.54	-0.02	0.02	-0.52	200	100.00%	0	0.00%	0	0.00%	0	1
c_3	0.36	-0.02	0.01	0.38	0	0.00%	0	0.00%	200	100.00%	0	1
c_4	1.99	-0.02	0.01	2.01	0	0.00%	0	0.00%	200	100.00%	0	1
c_5	-10.56	0.01	0.01	-10.57	200	100.00%	0	0.00%	0	0.00%	0	1
Total Rejection: 5			100.00%									

5.1.6 October 30, 2003

In the second day of the three-day period, the mean K_p index is 7.0000, second highest for 2003. Figure 5-43 starts out at near nine and ends at nine with a lull in the middle. The GIC on the pipeline in Figure 5-44 shows disruptions in the beginning and the end with a lull period in the middle with a maximum positive current of 27.00 amps and a maximum negative current of -48.57 amps. The automated range selection algorithm had the largest lambda value of 383.04 for wavelet levels 4-6 as shown in Table 5-34. The scaling exponents and singularity spectrum for levels 4-6 are shown in Figure 5-46 with the statistical tests in Table 5-35 showing that the

signal is monofractal with only c_1 being not equal to 0. Figure 5-45 shows the tightness of fit among the cumulant graphs. The IAAFT singularity spectrum shows differences from the singularity spectrum of the original signal while the shuffled singularity spectrum seems similar to the original signal in Figure 5-47. However, the statistical tests in Tables 5-37 and 5-38 show that the cumulants values for both the shuffled and IAAFT singularity spectrum are different for all cumulants for the IAAFT and for all but the c_1 cumulant in the Shuffle case.

The first two ranges that are multifractal are also presented here. Levels 3-9 had a lambda value of 347.837 and levels 2-7 had a lambda value of 347.631 for a difference of 0.206. The tightness of fit for those range selections are shown in Figures 5-50 and 5-53. Levels 2-7 appear to have a tighter fit than 3-9 among the cumulants; however, the automated range selection algorithm also takes into account the fit about the q graphs as well (not shown). The scaling exponents and singularity spectrum is shown in Figure 5-49 for levels 3-9 and Figure 5-54 for levels 2-7 with the results of the statistical tests in Table 5-36. The surrogate tests in Tables 5-39 to 5-42 show rejection for almost all cumulants. The most visible exceptions are the c_1 cumulant for levels 3-9 in the shuffle case and in the IAAFT case for levels 2-7. You can see this in Figures 5-51 and 5-55 where the apex of the singularity spectrum is the same for the original signal and the shuffle case for levels 3-9 and for the IAAFT and the original case for levels 2-7. The MFDFA results displayed in Figure 5-48 shows a singularity spectrum that is similar to the one generated by the wavelet leader method for levels 4-6 and Figures 5-52 and 5-56 and show a different singularity spectrum than the one generated by the wavelet leader method for levels 3-9 and 2-7.

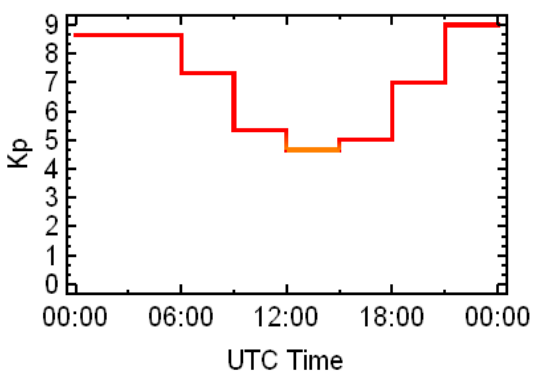

Figure 5-43: K_p index for October 30, 2003.

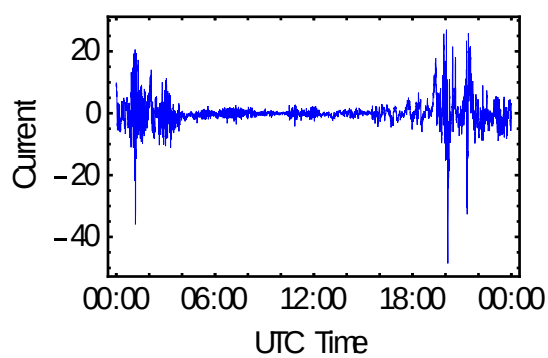

Figure 5-44: Pipeline data for October 30, 2003.

Table 5-34: Lambda values and classifications for all ranges for October 30, 2003 pipeline data.

j_1	j_2	Length	λ	Classification	r_1	r_2	r_3	r_4	r_5
4	6	3	383.404	Monofractal	1	0	0	0	0
3	8	6	373.004	Monofractal	1	0	0	0	0
4	8	5	371.086	Monofractal	1	0	0	0	0
3	6	4	364.614	Monofractal	1	0	0	0	0
3	7	5	359.045	Monofractal	1	0	0	0	0
3	9	7	347.837	Multifractal	1	1	1	0	1
2	7	6	347.631	Multifractal	1	1	0	0	0
4	9	6	346.296	Multifractal	1	1	1	0	1
5	7	3	345.045	Monofractal	1	0	0	0	0
2	8	7	343.294	Multifractal	1	1	0	0	0
5	8	4	338.110	Monofractal	1	0	0	0	0
2	6	5	335.026	Multifractal	1	1	0	0	0
2	9	8	333.574	Multifractal	1	1	0	1	1
5	9	5	326.966	Multifractal	1	1	1	0	1
1	8	8	325.921	Multifractal	1	1	0	1	0
4	7	4	324.926	Monofractal	1	0	0	0	0
1	7	7	324.600	Multifractal	1	1	0	1	0
1	9	9	320.402	Multifractal	1	1	0	1	1
1	6	6	316.428	Multifractal	1	1	0	1	0
1	5	5	307.324	Multifractal	1	1	0	1	0
1	4	4	307.273	Multifractal	1	1	0	1	0
3	5	3	307.060	Monofractal	1	0	0	0	0
2	5	4	304.641	Multifractal	1	1	0	0	0
6	9	4	293.923	Multifractal	0	1	1	0	1
7	9	3	285.727	Multifractal	0	1	0	0	0
6	8	3	280.756	None	0	0	0	0	0
2	4	3	279.053	Multifractal	1	1	0	0	0
1	3	3	265.379	Multifractal	1	1	0	1	0
8	10	3	112.256	None	0	0	0	0	0
7	10	4	107.534	None	0	0	0	0	0
6	10	5	97.813	None	0	0	0	0	0
5	10	6	86.714	None	0	0	0	0	0
4	10	7	80.848	None	0	0	0	0	0
3	10	8	76.947	None	0	0	0	0	0
2	10	9	72.873	None	0	0	0	0	0
1	10	10	70.934	None	0	0	0	0	0

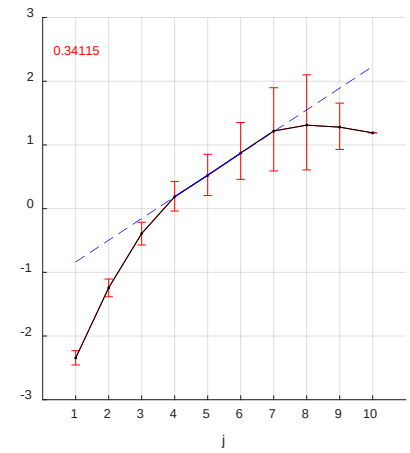

(a)

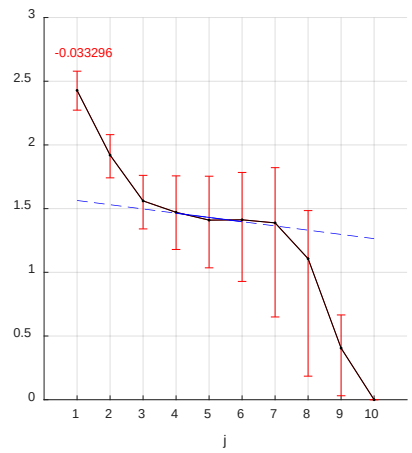

(b)

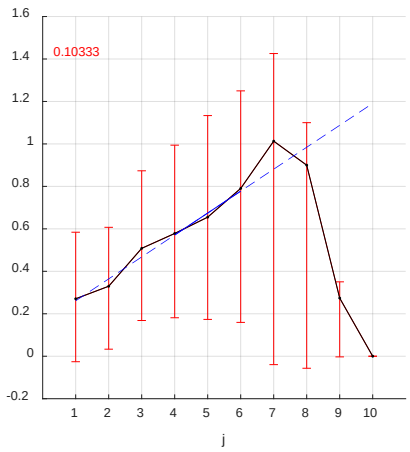

(c)

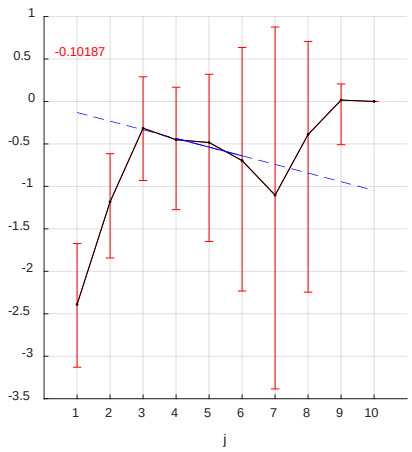

(d)

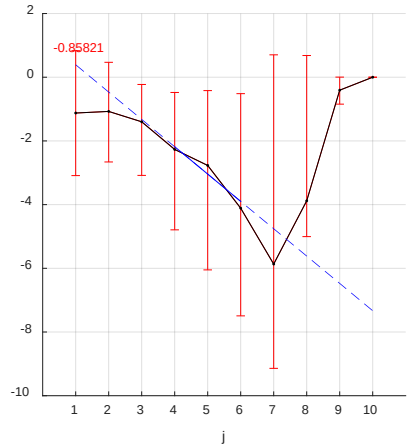

(e)

Figure 5-45: Cumulant graphs for levels 4-6 for the October 30, 2003 pipeline data. (a) c_1 (b) c_2 (c) c_3 (d) c_4 (e) c_5

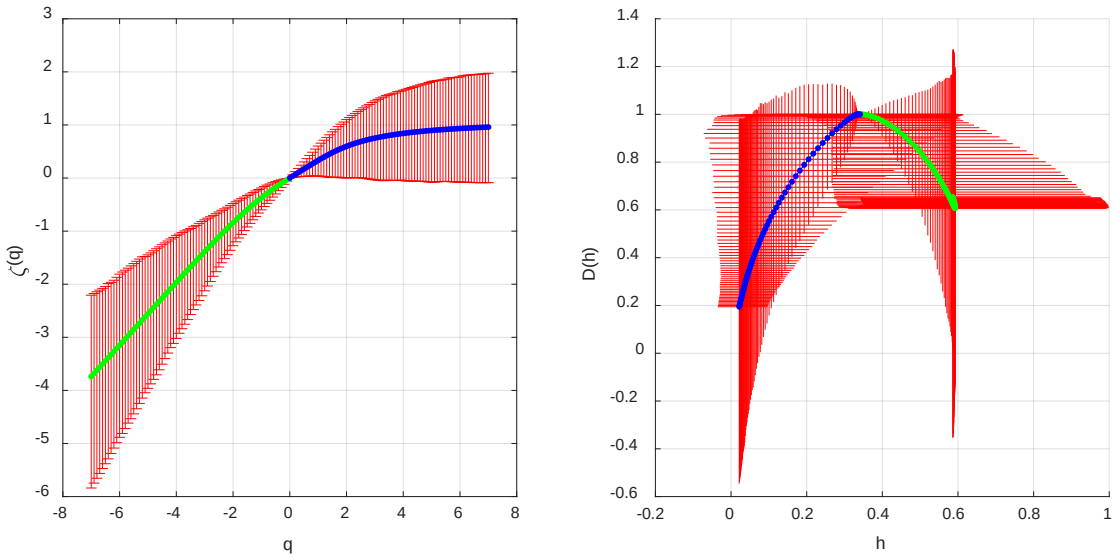

(a) (b)

Figure 5-46: (a) Scaling exponents, (b) singularity spectrum for the October 30, 2003 pipeline data for levels 4-6. Positive q values are blue, negative q values are green.

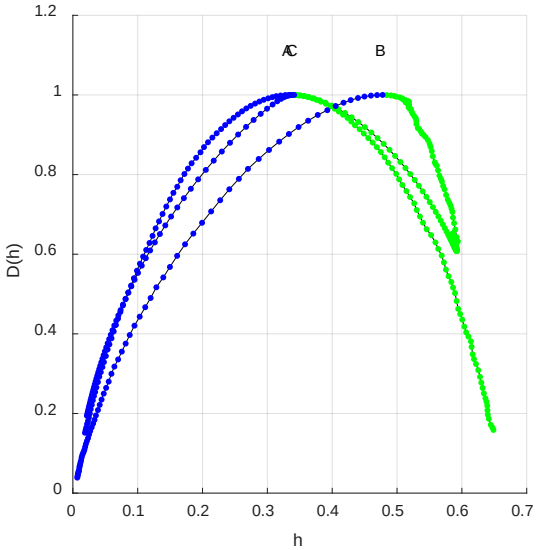

Figure 5-47: Median (a) shuffled and (b) IAAFT surrogate singularity spectrum graphs for the October 30, 2003 pipeline data with the (c) singularity spectrum of the original signal for comparison for levels 4-6. Positive q values are blue, negative q values are green.

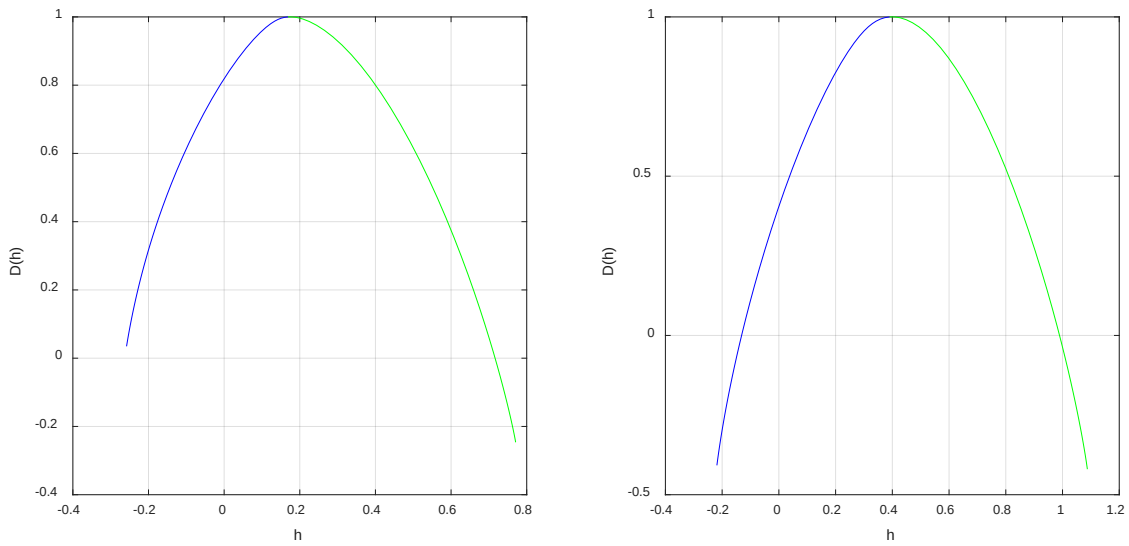

(a) (b)

Figure 5-48: Singularity spectrum generated by MFDFA for levels 4-6 for the October 30, 2003 pipeline data for (a) M=2 (b) M=3. Positive q values are blue, negative q values are green.

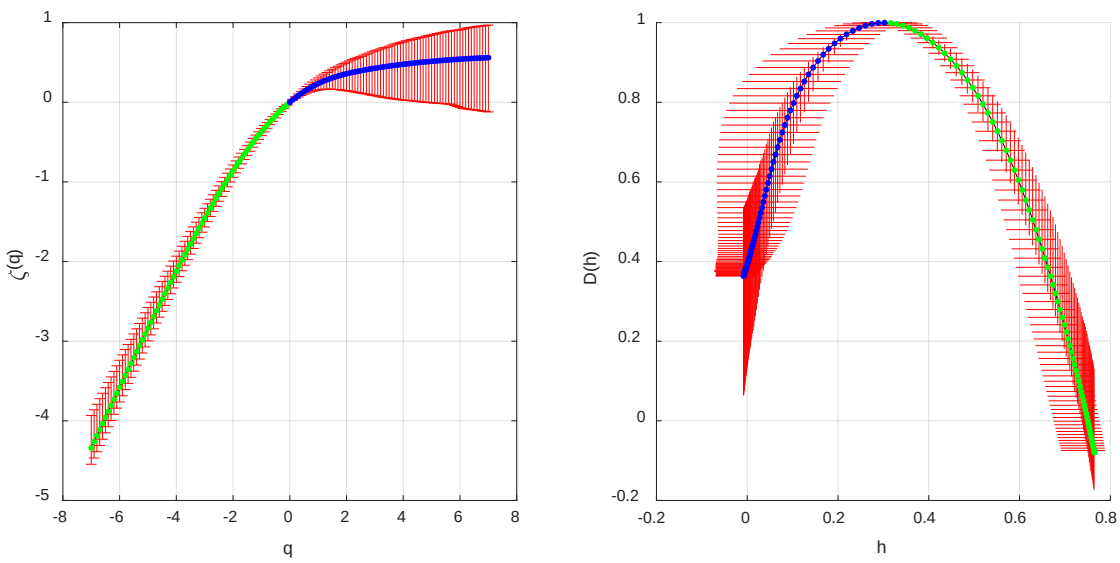

(a) (b)

Figure 5-49: (a) Scaling exponents, (b) singularity spectrum for the October 30, 2003 pipeline data for levels 3-9. Positive q values are blue, negative q values are green.

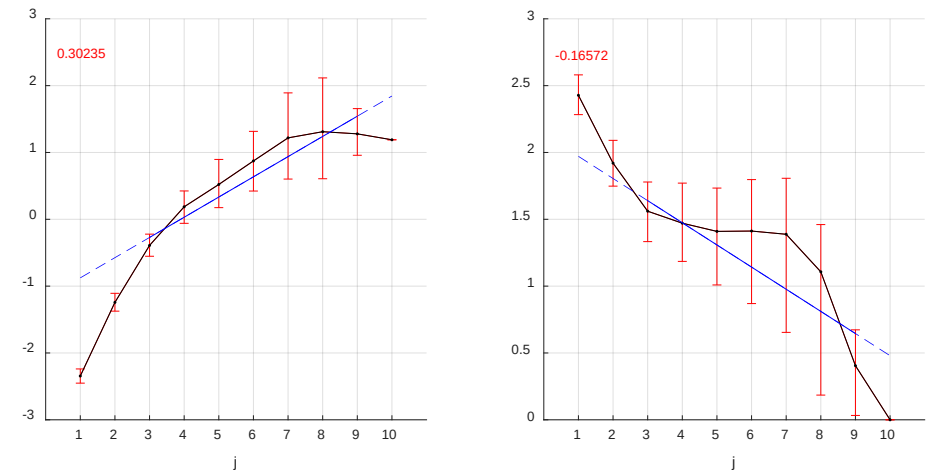

(a)

(b)

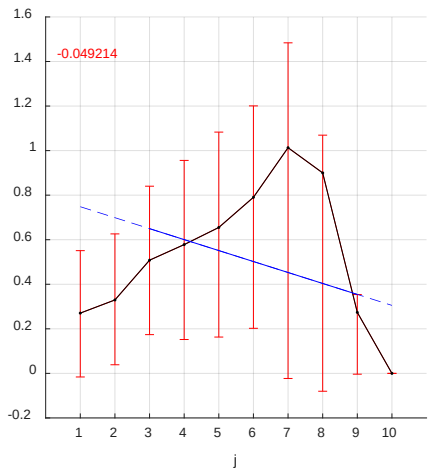

(c)

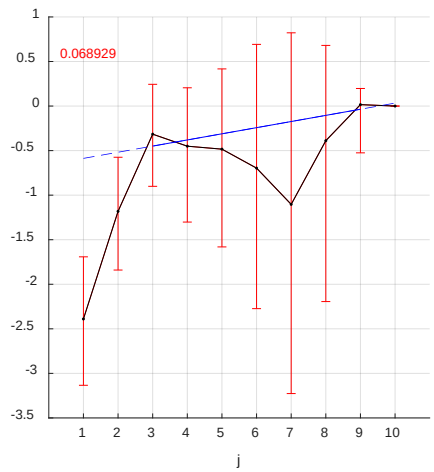

(d)

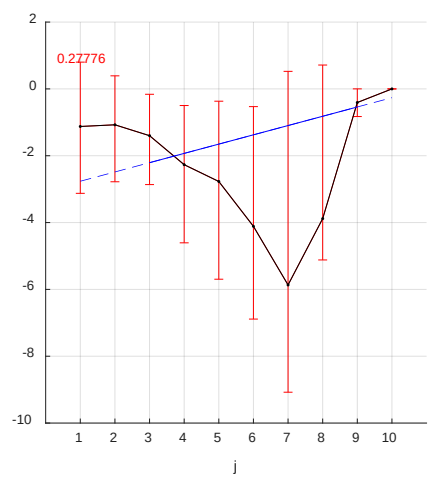

(e)

Figure 5-50: Cumulant graphs for levels 3-9 for the October 30, 2003 pipeline data. (a) c_1 (b) c_2 (c) c_3 (d) c_4 (e) c_5

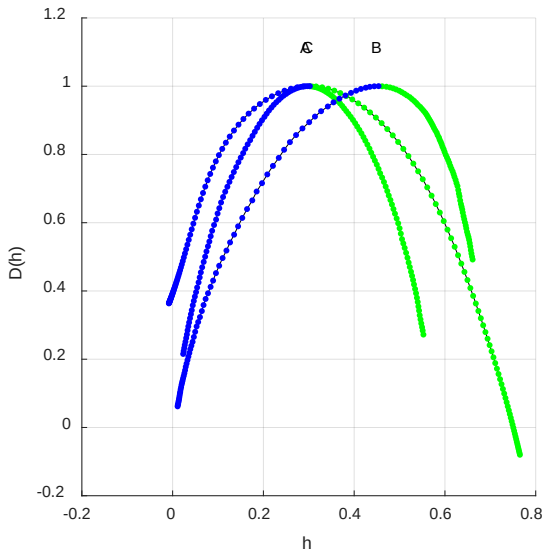

Figure 5-51: Median (a) shuffled and (b) IAAFT surrogate singularity spectrum graphs for the October 30, 2003 pipeline data with the (c) singularity spectrum of the original signal for comparison for levels 3-9. Positive q values are blue, negative q values are green.

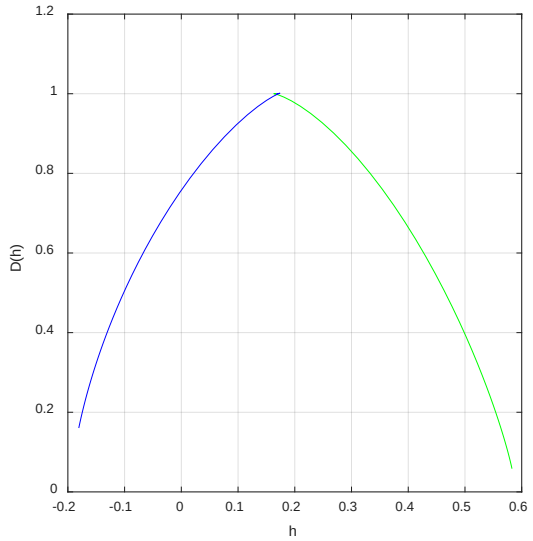

Figure 5-52: Singularity spectrum generated by MFDFA for levels 3-9 for graphs for the October 30, 2003 pipeline data for M=1. Positive q values are blue, negative q values are green.

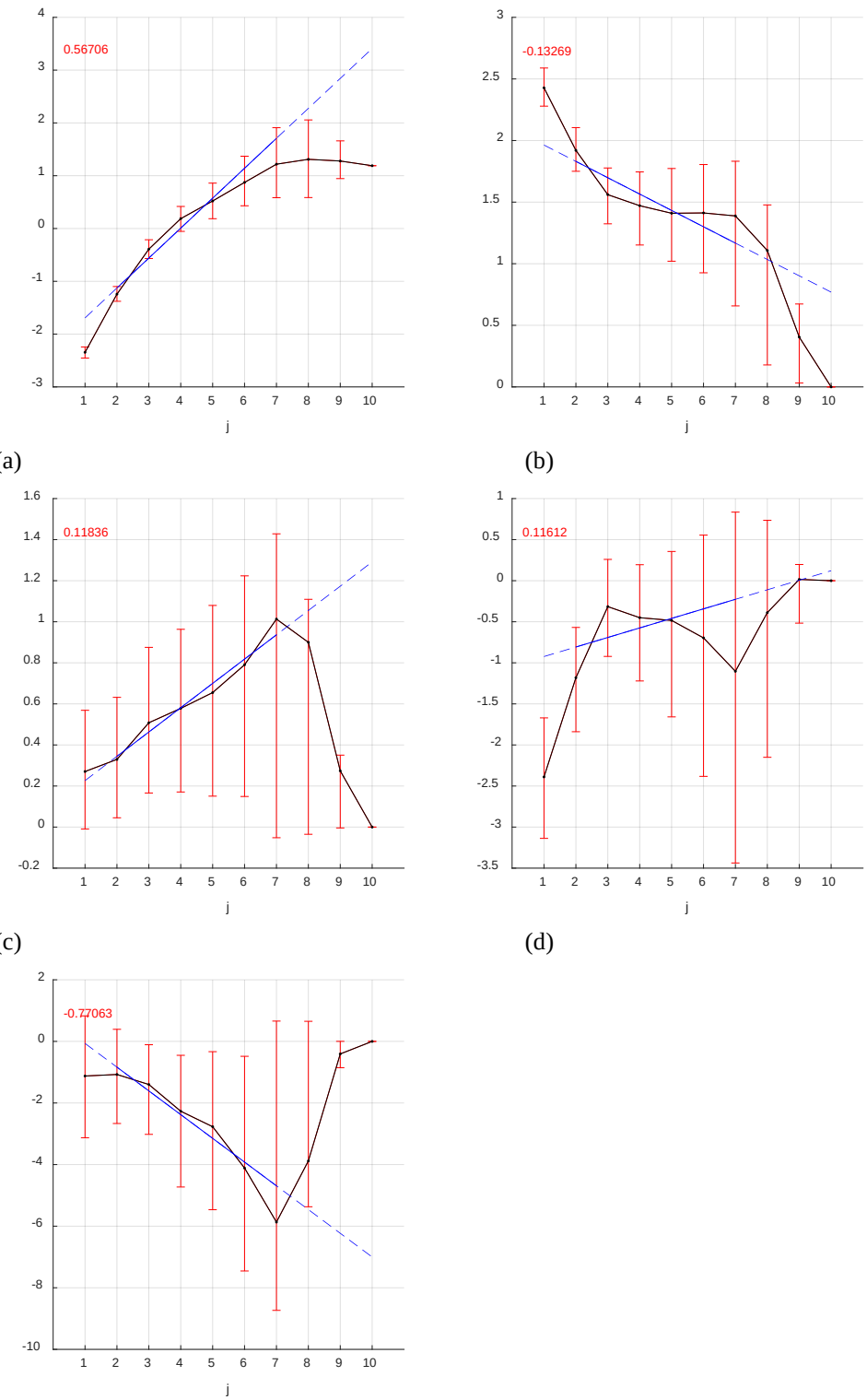

Figure 5-53: Cumulant graphs for levels 2-7 for the October 30, 2003 pipeline data. (a) c_1 (b) c_2 (c) c_3 (d) c_4 (e) c_5

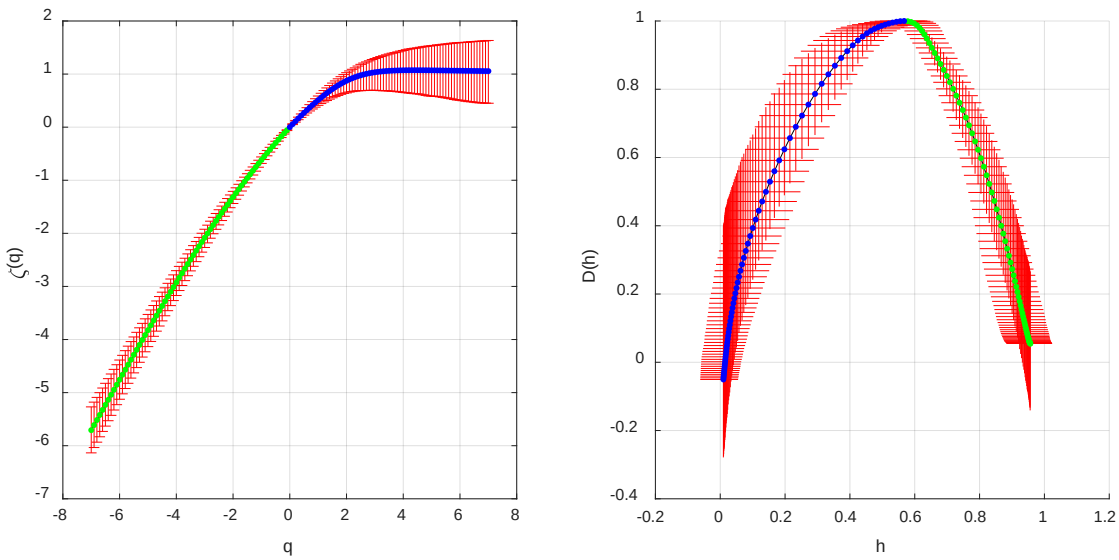

(a) (b)

Figure 5-54: (a) Scaling exponents, (b) singularity spectrum for the October 30, 2003 pipeline data for levels 2-7. Positive q values are blue, negative q values are green.

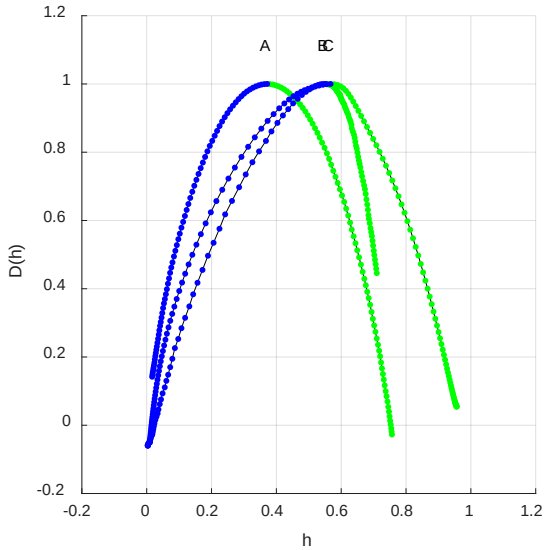

Figure 5-55: Median (a) shuffled and (b) IAAFT surrogate singularity spectrum graphs for the October 30, 2003 pipeline data with the (c) singularity spectrum of the original signal for comparison for levels 2-7. Positive q values are blue, negative q values are green.

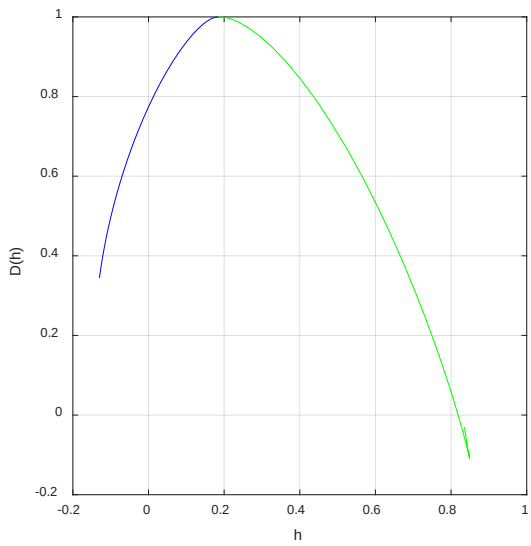

Figure 5-56: Singularity spectrum generated by MFDFA for the October 30, 2003 pipeline data for levels 2-7 for M=1, all others skewed. Positive q values are blue, negative q values are green.

Table 5-35: Cumulant values for October 30, 2003 pipeline data for levels 4-6

Cumulant	Value	STD	P-Value	Reject
c_1	0.34	0.15	0.012	1
c_2	-0.03	0.16	0.753	0
c_3	0.10	0.21	0.715	0
c_4	-0.10	0.46	0.835	0
c_5	-0.86	1.29	0.641	0

Table 5-36: Cumulant values for October 30, 2003 pipeline data for levels 3-9 and 2-7

	Level 3-9				Level 2-7			
Cumulant	Value	STD	P-Value	Reject	Value	STD	P-Value	Reject
c_1	0.30	0.03	0.002	1	0.57	0.04	0.002	1
c_2	-0.17	0.03	0.002	1	-0.13	0.05	0.002	1
c_3	-0.05	0.03	0.052	1	0.12	0.07	0.204	0
c_4	0.07	0.06	0.328	0	0.12	0.16	0.517	0
c_5	0.28	0.13	0.022	1	-0.77	0.39	0.158	0

Table 5-37: Shuffle cumulant values for October 30, 2003 pipeline data for levels 4-6

Cumulant	Actual Value	Mean Shuffle Value	STD	Δ Value	Greater		Equal		Less		P-Value	Reject
c_1	0.34	0.34	0.02	0.00	79	39.50%	0	0.00%	121	60.50%	0.395	0
c_2	-0.03	-0.07	0.01	0.04	0	0.00%	0	0.00%	200	100.00%	0.000	1
c_3	0.10	0.00	0.01	0.10	0	0.00%	0	0.00%	200	100.00%	0.000	1
c_4	-0.10	0.00	0.01	-0.10	200	100.00%	0	0.00%	0	0.00%	0.000	1
c_5	-0.86	0.00	0.01	-0.86	200	100.00%	0	0.00%	0	0.00%	0.000	1
Total Rejection: 4			80.00%									

Table 5-38: IAAFT cumulant values for October 30, 2003 pipeline data for levels 4-6

Cumulant	Actual Value	Mean IAAFT Value	STD	Δ Value	Greater		Equal		Less		P-Value	Reject
	0.34	0.48	0.03	-0.14	200	100.00%	0	0.00%	0	0.00%	0.000	1
c_2	-0.03	-0.08	0.03	0.05	9	4.50%	0	0.00%	191	95.50%	0.045	1
c_3	0.10	-0.09	0.03	0.19	0	0.00%	0	0.00%	200	100.00%	0.000	1
c_4	-0.10	-0.02	0.04	-0.08	196	98.00%	0	0.00%	4	2.00%	0.020	1
c_5	-0.86	0.11	0.06	-0.97	200	100.00%	0	0.00%	0	0.00%	0.000	1
Total Rejection: 5			100.00%									

Table 5-39: Shuffle cumulant values for October 30, 2003 pipeline data for levels 3-9

Cumulant	Actual Value	Mean Shuffle Value	STD	Δ Value	Greater		Equal		Less		P-Value	Reject
c_1	0.30	0.30	0.02	0.00	81	40.50%	0	0.00%	119	59.50%	0.405	0
c_2	-0.17	-0.05	0.01	-0.12	200	100.00%	0	0.00%	0	0.00%	0.000	1
c_3	-0.05	0.00	0.00	-0.05	200	100.00%	0	0.00%	0	0.00%	0.000	1
c_4	0.07	0.00	0.00	0.07	0	0.00%	0	0.00%	200	100.00%	0.000	1
c_5	0.28	0.00	0.00	0.28	0	0.00%	0	0.00%	200	100.00%	0.00	1
Total Rejection: 4			80.00%									

Table 5-40: IAAFT cumulant values for October 30, 2003 pipeline data for levels 3-9

Cumulant	Actual Value	Mean IAAFT Value	STD	Δ Value	Greater		Equal		Less		P-Value	Reject
c_1	0.30	0.45	0.03	-0.15	200	100.00%	0	0.00%	0	0.00%	0.000	1
c_2	-0.17	-0.09	0.02	-0.08	200	100.00%	0	0.00%	0	0.00%	0.000	1
c_3	-0.05	-0.05	0.01	0.00	121	60.50%	0	0.00%	79	39.50%	0.395	0
c_4	0.07	-0.01	0.01	0.08	0	0.00%	0	0.00%	200	100.00%	0.000	1
c_5	0.28	0.04	0.02	0.24	0	0.00%	0	0.00%	200	100.00%	0.000	1
Total Rejection: 4			80.00%									

Table 5-41: Shuffle cumulant values for October 30, 2003 pipeline data for levels 2-7

Cumulant	Actual Value	Mean Shuffle Value	STD	Δ Value	Greater		Equal		Less		P-Value	Reject
c_1	0.57	0.37	0.01	0.20	0	0.00%	0	0.00%	200	100.00%	0.000	1
c_2	-0.13	-0.09	0.01	-0.04	200	100.00%	0	0.00%	0	0.00%	0.000	1
c_3	0.12	0.00	0.00	0.12	0	0.00%	0	0.00%	200	100.00%	0.000	1
c_4	0.12	0.01	0.00	0.11	0	0.00%	0	0.00%	200	100.00%	0.000	1
c_5	-0.77	0.01	0.01	-0.78	200	100.00%	0	0.00%	0	0.00%	0.000	1
Total Rejection: 5			100.00%									

Table 5-42: IAAFT cumulant values for October 30, 2003 pipeline data for levels 2-7

Cumulant	Actual Value	Mean IAAFT Value	STD	Δ Value	Greater		Equal		Less		P-Value	Reject
c_1	0.57	0.55	0.02	0.02	35	17.50%	0	0.00%	165	82.50%	0.175	0
c_2	-0.13	-0.06	0.02	-0.07	200	100.00%	0	0.00%	0	0.00%	0.000	1
c_3	0.12	-0.06	0.01	0.18	0	0.00%	0	0.00%	200	100.00%	0.000	1
c_4	0.12	-0.06	0.03	0.18	0	0.00%	0	0.00%	200	100.00%	0.000	1
c_5	-0.77	-0.01	0.04	-0.76	200	100.00%	0	0.00%	0	0.00%	0.000	1
Total Rejection: 4			80.00%									

5.1.7 October 31, 2003

In the third day of the Halloween storm, the mean K_p index is 6.2875, the third highest for 2003. The three-hour values of the K_p index in Figure 5-57 start at nine and then decrease as the storm subsides. The pipeline GIC signal of October 31, 2003 is displayed in Figure 5-58 with a maximum positive current of 30.13 amps and a maximum negative current of -27.87 amps. This shows rather significant disruptions at the beginning with a lull period at the end. From the lambda values in Table 5-43, we can see that the automated range selection algorithm had the largest lambda value of 377.906 for wavelet levels 4-6 with the tightness of fit among the cumulants shown in Figure 5-60. While the singularity spectrum and scaling exponents in Figure 5-59 seem to show a multifractal, the statistical tests in Table 5-44 shows that it is classified as a monofractal. The surrogate singularity spectrum in Figure 5-61 shows a lot of similarities with the median IAAFT, however the surrogate statistical tests in Tables 5-45 and 5-46 show rejection for all cumulants for the shuffle test and all but c_2 for the IAAFT.

The MFDFA results displayed in Figure 5-62 shows a singularity spectrum that is similar to the one generated by the wavelet leader spectrum. The apex of both parabolas is near 0.4. The difference is that the one generated by the MFDFA is wider than the one generated by the wavelet leader method and has negative h values, whereas the h values for the wavelet leader method are all greater than 0 for the selected q values. Table 5-43 listed levels 2-8 being a multifractal, and its lambda value is near the one for levels 4-6. That was analyzed and it did not generate a good singularity spectrum.

Table 5-43: Lambda values and classifications for all ranges for the October 31, 2003 pipeline data.

j_1	j_2	Length	λ	Classification	r_1	r_2	r_3	r_4	r_5
4	6	3	381.174	Monofractal	1	0	0	0	0
2	8	7	372.081	Multifractal	1	1	1	0	1
4	7	4	364.279	Monofractal	1	0	0	0	0
3	6	4	360.902	Monofractal	1	0	0	0	0
3	7	5	355.209	Monofractal	1	0	0	0	0
2	9	8	354.680	Multifractal	1	1	0	1	0
5	7	3	354.187	None	0	0	0	0	0
6	8	3	347.358	None	0	0	0	0	0
3	8	6	342.255	Multifractal	1	1	0	0	0
2	7	6	340.452	Multifractal	1	0	1	0	1
5	9	5	338.874	Multifractal	1	1	0	1	1
2	6	5	337.197	Multifractal	1	0	1	0	1
6	9	4	335.999	Multifractal	1	1	0	1	0
5	8	4	328.845	Monofractal	1	0	0	0	0
7	9	3	323.569	Multifractal	1	1	0	0	0
3	5	3	305.796	Monofractal	1	0	0	0	0
3	9	7	305.530	Multifractal	1	1	0	1	1
2	4	3	299.032	Multifractal	1	0	1	0	1
1	9	9	298.024	Multifractal	1	1	1	1	1
4	8	5	296.726	Multifractal	1	1	0	0	0
2	5	4	295.896	Multifractal	1	0	1	0	1
1	8	8	292.252	Multifractal	1	0	1	0	1
4	9	6	279.352	Multifractal	1	1	1	1	1
1	7	7	268.924	Multifractal	1	0	1	0	1
1	6	6	259.710	Multifractal	1	0	1	0	1
1	5	5	245.511	Multifractal	1	0	1	0	1
1	4	4	239.347	Multifractal	1	0	1	0	1
1	3	3	221.998	Multifractal	1	0	1	0	1
8	10	3	48.338	Monofractal	1	0	0	0	0
7	10	4	47.227	Monofractal	1	0	0	0	0
6	10	5	45.712	Monofractal	1	0	0	0	0
5	10	6	44.041	Monofractal	1	0	0	0	0
4	10	7	43.552	Monofractal	1	0	0	0	0
3	10	8	42.802	None	0	0	0	0	0
2	10	9	42.656	Monofractal	1	0	0	0	0
1	10	10	42.218	Monofractal	1	0	0	0	0

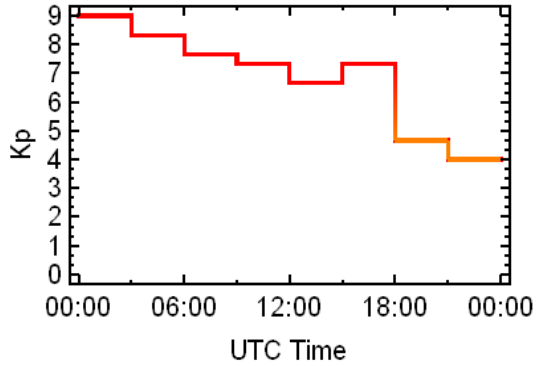

Figure 5-57: K_p index for October 31, 2003.

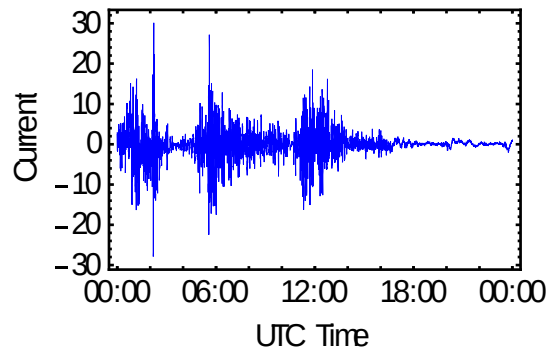

Figure 5-58: Pipeline data for October 31, 2003.

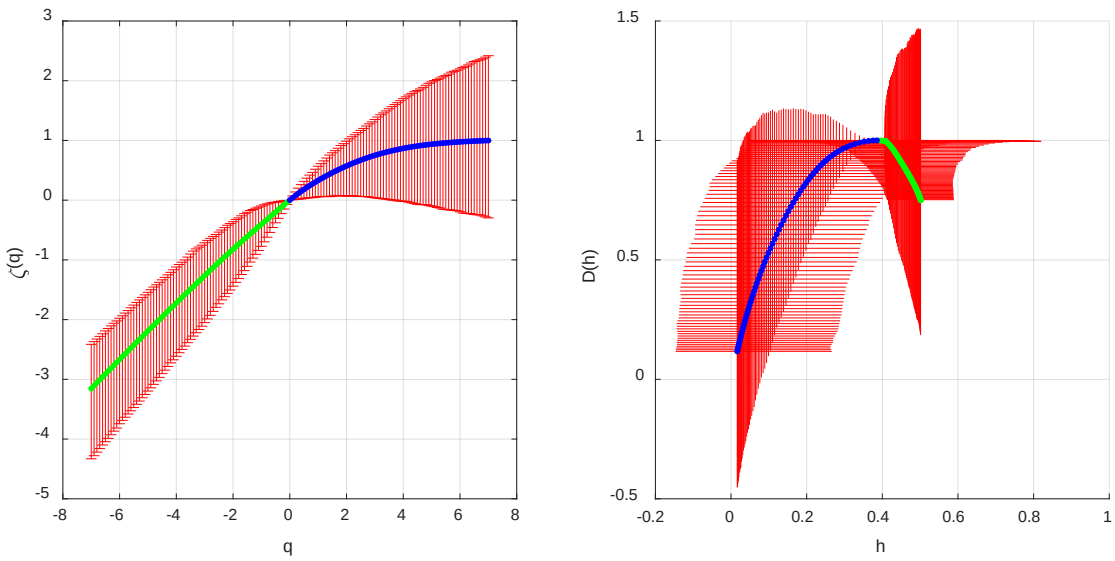

(a) (b)

Figure 5-59: (a) Scaling exponents and (b) singularity spectrum for the October 31, 2003 pipeline data for levels 4-6. Positive q values are blue, negative q values are green.

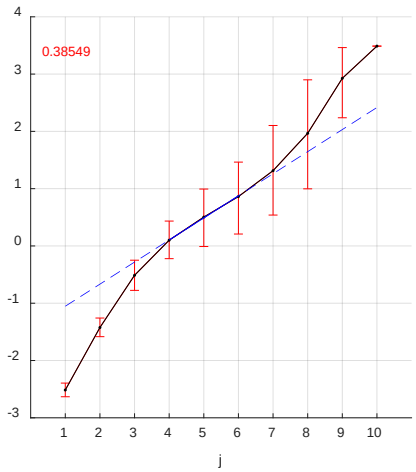

(a)

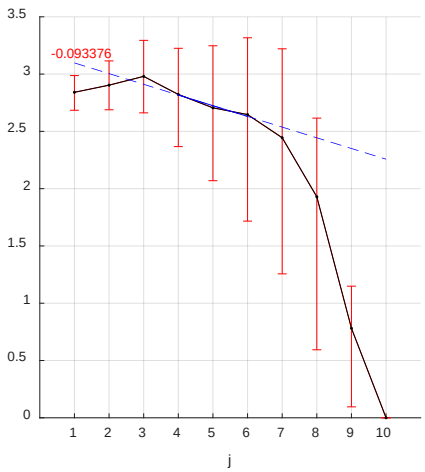

(b)

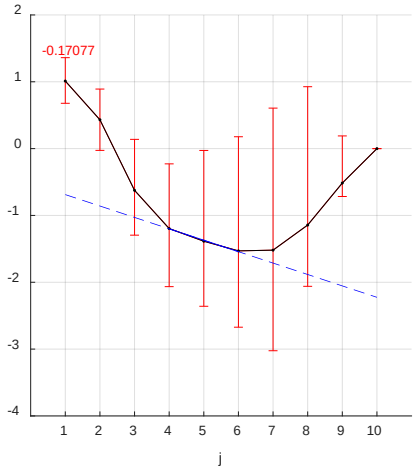

(c)

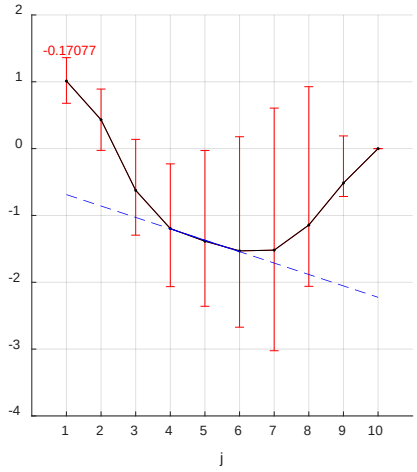

(d)

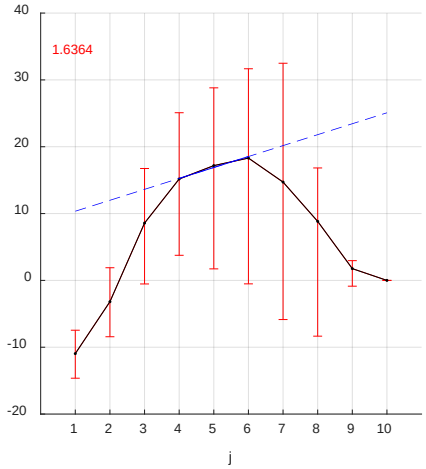

(e)

Figure 5-60: Cumulant graphs for levels 4-6 for the October 31, 2003 pipeline data. (a) c_1 (b) c_2 (c) c_3 (d) c_4 (e) c_5

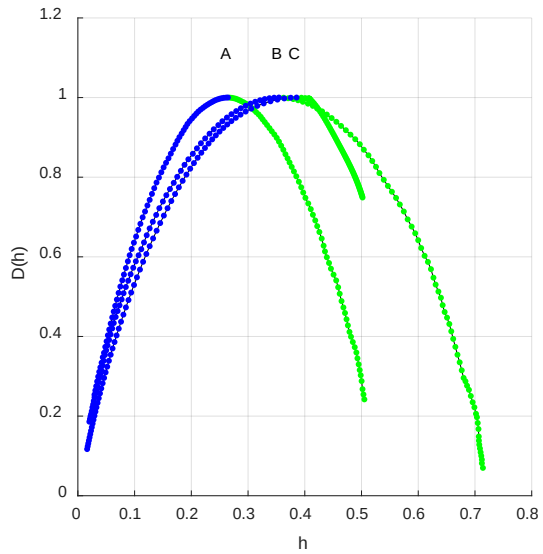

Figure 5-61: Median (a) shuffled and (b) IAAFT surrogate singularity spectrum graphs for the October 31, 2003 pipeline data with the (c) singularity spectrum of the original signal for comparison for levels 4-6. Positive q values are blue, negative q values are green.

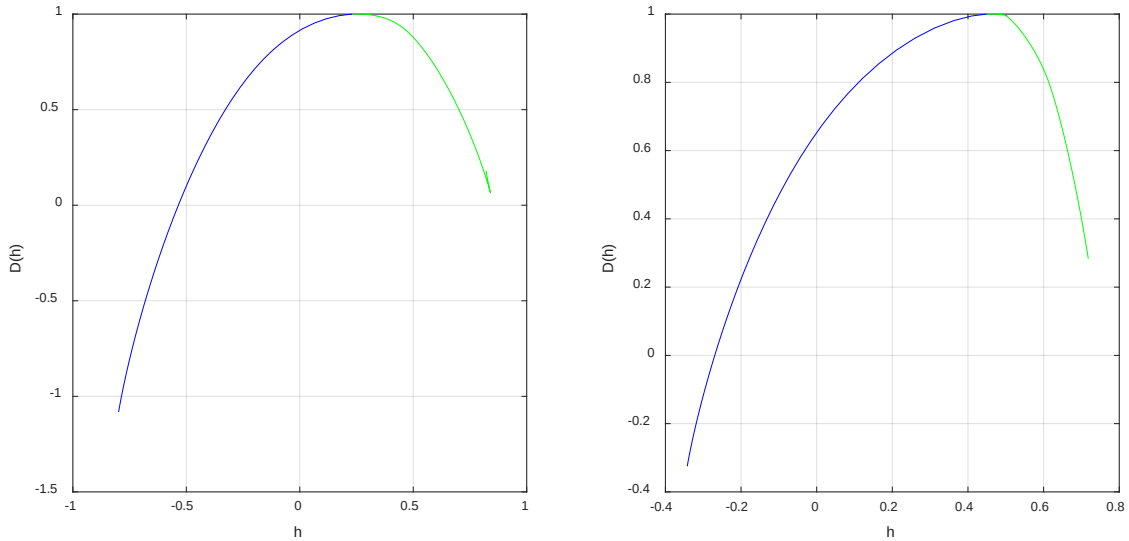

(a) (b)

Figure 5-62: Singularity spectrum generated by MFDFA for the October 31, 2003 pipeline data for levels 4-6 for (a) M=2 (b) M=3. Positive q values are blue, negative q values are green.

Table 5-44: Cumulant values for the October 31, 2003 pipeline data

Cumulant	Value	STD	P-Value	Reject
c_1	0.39	0.20	0.058	1
c_2	-0.09	0.26	0.621	0
c_3	-0.17	0.50	0.883	0
c_4	0.44	1.89	0.773	0
c_5	1.64	5.91	0.983	0

Table 5-45: Shuffle cumulant values for the October 31, 2003 pipeline data

Cumulant	Actual Value	Mean Shuffle Value	STD	Δ Value	Greater		Equal		Less		P-Value	Reject
c_1	0.39	0.26	0.01	0.13	0	0.00%	0	0.00%	200	100.00%	0.000	1
c_2	-0.09	-0.04	0.01	-0.05	200	100.00%	0	0.00%	0	0.00%	0.000	1
c_3	-0.17	0.00	0.00	-0.17	200	100.00%	0	0.00%	0	0.00%	0.000	1
c_4	0.44	0.00	0.00	0.44	0	0.00%	0	0.00%	200	100.00%	0.000	1
c_5	1.64	0.00	0.00	1.64	0	0.00%	0	0.00%	200	100.00%	0.000	1
Total Rejection: 5			100.00%									

Table 5-46: IAAFT cumulant values for the October 31, 2003 pipeline data

Cumulant	Actual Value	Mean IAAFT Value	STD	Δ Value	Greater		Equal		Less		P-Value	Reject
c_1	0.39	0.35	0.02	0.04	12	6.00%	0	0.00%	188	94.00%	0.060	1
c_2	-0.09	-0.09	0.01	0.00	155	77.50%	0	0.00%	45	22.50%	0.225	0
c_3	-0.17	0.00	0.01	-0.17	200	100.00%	0	0.00%	0	0.00%	0.000	1
c_4	0.44	0.01	0.01	0.43	0	0.00%	0	0.00%	200	100.00%	0.000	1
c_5	1.64	0.00	0.01	1.64	0	0.00%	0	0.00%	200	100.00%	0.000	1
Total Rejection: 4			80.00%									

5.2 Overall results by K_p Index

The distribution of the K_p index for 2003 is given in Table 5-47 and Figure 5-63. 25% of the values were 2 or less, 50% were 3 or less, and 75% were 4 or less. This analysis will look at how the singularity spectrum properties of the pipeline data for each 3-hour interval change as the K_p index value changes. The resolution of the K_p index is in thirds, so the results will be sorted by the floor of that value so that it is an integer as given in Table 5-47. At 10 second sampling, the number of values for a three-hour interval will be 1080. Q values were set the same as in the previous section from -7 to 7 by 0.1. Bootstrap resamples for the automated range selection algorithm was set to 1000. No surrogate analysis was done in this case. As with the previous analysis, the Daubechies wavelet family was used with 3 vanishing moments, which gives a maximum discrete wavelet transform level of 8.

Table 5-47: Distribution of the K_p index for the pipeline data for 2003.

K_p Index	Number	Percentage
0	175	5.99%
1	429	14.69%
2	696	23.84%
3	777	26.61%
4	545	18.66%
5	219	7.50%
6	48	1.64%
7	18	0.62%
8	10	0.34%
9	3	0.10%

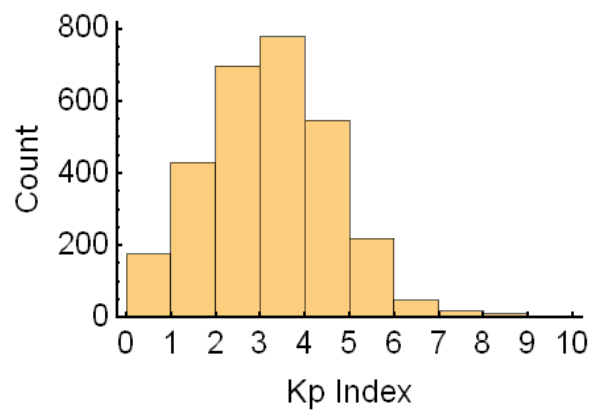

Figure 5-63: Histogram of the distribution of K_p index for the pipeline data for 2003.

5.2.1 K_p index 0

K_p index 0 values occurred for 5.99% of the pipeline data available for 2003, for a total of 175 intervals. Index values 0-2 correspond to the quiet states of the magnetosphere. The results for each individual range of the data are given in Table 5-48. From that we can see that range 3-6 had the greatest lambda value. The median scaling exponents and singularity spectrum with the 5%-95% error bars are given in Figure 5-64. From this, we can see a clear singularity spectrum with considerable variance in the error bars. The cumulant values are shown in Table 5-49.

Table 5-48: Results for each individual range for K_p index 0 for 2003 pipeline data.

			Median			
j_1	**j_2**	**Length**	**Lambda**	**Multifractal**	**Monofractal**	**None**
3	6	4	343.7910	130	7	1
3	5	3	332.5480	86	49	3
2	6	5	332.0050	134	4	0
2	5	4	326.3575	122	16	0
4	6	3	316.8325	117	18	3
2	4	3	304.5785	96	42	0
3	7	5	296.2140	87	20	31
2	7	6	283.9695	87	20	31
4	7	4	274.4080	87	20	31
1	6	6	273.0445	138	0	0
1	5	5	269.6300	138	0	0
1	4	4	260.4820	137	1	0
5	7	3	246.9325	82	22	34
1	3	3	242.9480	135	3	0
1	7	7	239.1325	87	20	31

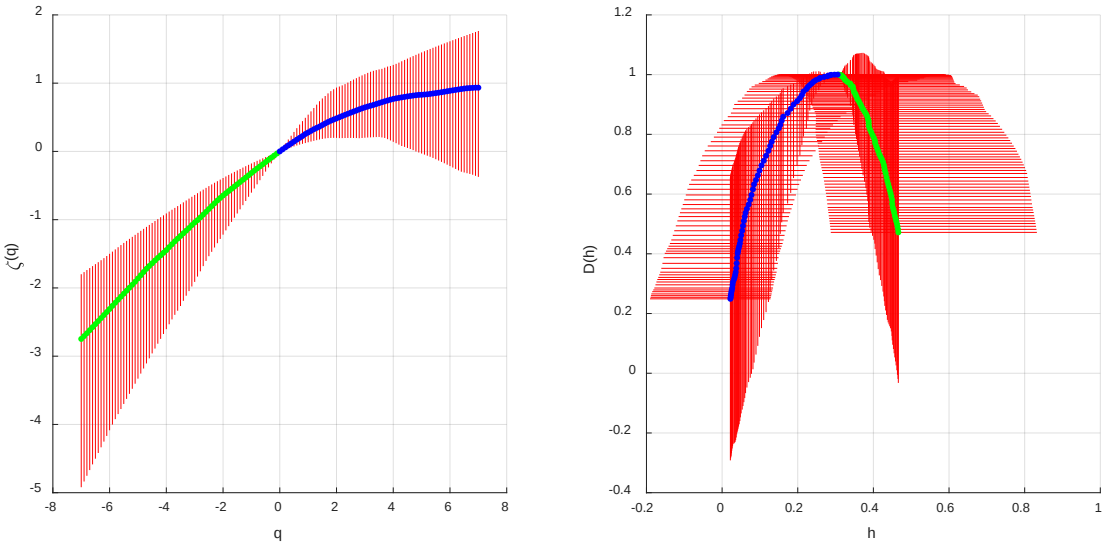

(a) (b)

Figure 5-64: (a) Scaling exponents, and (b) singularity spectrum for median values for levels 3-6 for the pipeline data corresponding to K_p index 0. Positive q values are blue, negative q values are green.

Table 5-49: Cumulant values for K_p index 0 for 2003 pipeline data for levels 3-6.

Cumulant	5%	50%	95%
c_1	0.1556	0.3054	0.5915
c_2	-0.1300	-0.0403	0.0722
c_3	-0.1139	-0.0054	0.0383
c_4	-0.2566	-0.0007	0.0284
c_5	-0.2118	-0.0001	0.0789

5.2.2 K_p index 1

K_p index 1 values occurred for 14.69% of the pipeline data available for 2003, for a total of 429 intervals. The results for each individual range of the data are given in Table 5-50. From that we can see that range 3-6 had the greatest lambda value. The median scaling exponents and singularity spectrum with the 5%-95% error bars are given in Figure 5-65. As with K_p index 0, we can see a clear singularity spectrum with considerable variance in the error bars. The cumulant values are shown in Table 5-51.

Table 5-50: Results for each individual range for K_p index 1 for 2003 pipeline data.

j_1	j_2	Length	Median Lambda	Multifractal	Monofractal	None
3	6	4	332.9020	292	13	0
3	5	3	324.6800	194	101	10
2	5	4	324.0110	273	32	0
2	6	5	322.8870	299	6	0
4	6	3	304.8100	262	36	7
2	4	3	298.7570	210	95	0
1	6	6	275.0300	304	1	0
1	5	5	270.0020	301	4	0
1	4	4	261.4070	295	10	0
1	3	3	241.4910	290	15	0
3	7	5	215.9330	154	77	74
4	7	4	210.1700	154	77	74
2	7	6	204.7640	154	77	74
5	7	3	188.9140	144	82	79
1	7	7	183.1380	154	77	74

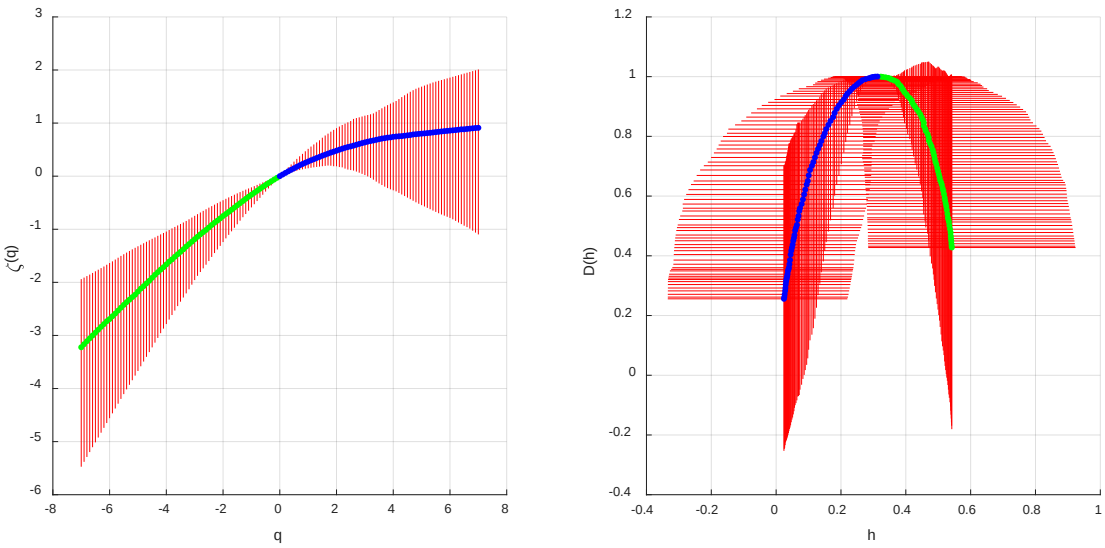

(a) (b)

Figure 5-65: (a) Scaling exponents, and (b) singularity spectrum for median values for levels 3-6 for the pipeline data corresponding to K_p index 1. Positive q values are blue, negative q values are green.

Table 5-51: Cumulant values for K_p index 1 for 2003 pipeline data for levels 3-6.

Cumulant	5%	50%	95%
c_1	0.1816	0.3125	0.5698
c_2	-0.1821	-0.0601	0.0035
c_3	-0.1180	-0.0059	0.0256
c_4	-0.0791	0.0009	0.0584
c_5	-0.0513	0.0007	0.1697

5.2.3 K_p index 2

K_p index 2 values occurred for 23.84% of the pipeline data available for 2003, for a total of 696 intervals. The results for each individual range of the data are given in Table 5-52. From that we can see that range 3-6 had the greatest lambda value. The median scaling exponents and singularity spectrum with the 5%-95% error bars are given in Figure 5-66. As with the previous index values, we can see a clear singularity spectrum with considerable variance in the error bars. The cumulant values are shown in Table 5-53.

Table 5-52: Results for each individual range for K_p index 2 for 2003 pipeline data.

j_1	j_2	Length	Median Lambda	Multifractal	Monofractal	None
3	6	4	333.2305	431	30	1
3	5	3	327.3395	289	164	9
2	6	5	326.2370	453	9	0
2	5	4	325.4435	399	63	0
4	6	3	307.9245	376	73	13
2	4	3	306.6155	303	159	0
1	6	6	284.5745	460	2	0
1	5	5	277.4870	455	7	0
1	4	4	266.4350	442	20	0
2	7	6	255.8740	250	103	109
3	7	5	253.1800	249	104	109
1	3	3	245.1790	431	31	0
4	7	4	240.0535	244	107	111
1	7	7	225.6990	250	103	109
5	7	3	215.6240	238	108	116

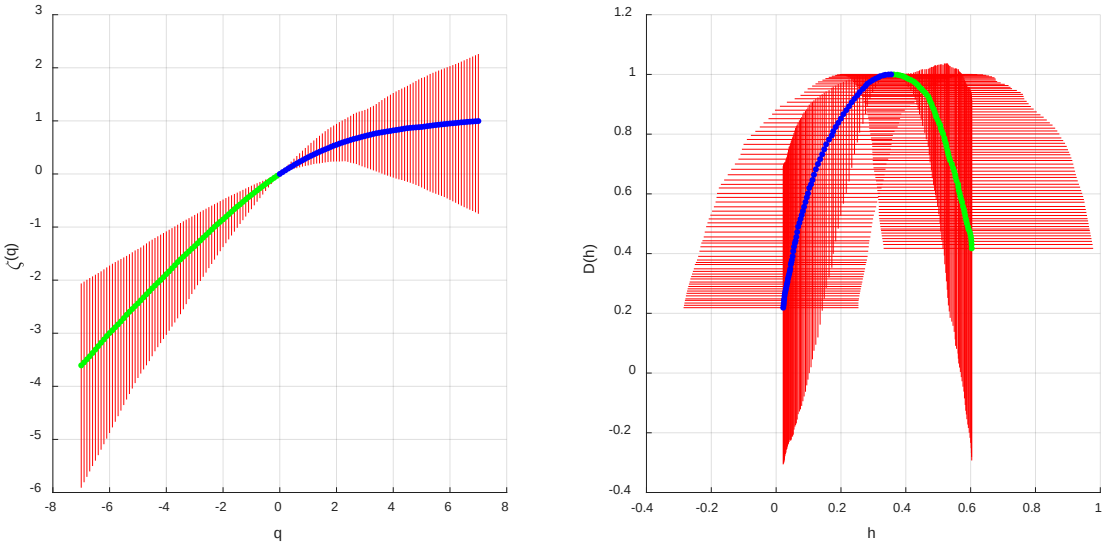

(a) (b)

Figure 5-66: (a) Scaling exponents, and (b) singularity spectrum for median values for levels 3-6 for the pipeline data corresponding to K_p index 2. Positive q values are blue, negative q values are green.

Table 5-53: Cumulant values for K_p index 2 for 2003 pipeline data for levels 3-6.

Cumulant	5%	50%	95%
c_1	0.2008	0.3548	0.6052
c_2	-0.2070	-0.0696	0.0150
c_3	-0.1740	-0.0084	0.0417
c_4	-0.1491	0.0010	0.0791
c_5	-0.1010	0.0025	0.2860

5.2.4 K_p index 3

K_p index 3 values occurred for 26.61% of the pipeline data available for 2003, for a total of 777 intervals. We are moving from the quiet state of magnetosphere for the index values 0-2 to unsettled. The results for each individual range of the data are given in Table 5-54. From that we can see that range 3-6 had the greatest lambda value. The median scaling exponents and singularity spectrum with the 5%-95% error bars are given in Figure 5-67. From this, we can see a clear singularity spectrum with considerable variance in the error bars. The cumulant values are shown in Table 5-55.

Table 5-54: Results for each individual range for K_p index 3 for 2003 pipeline data.

j_1	j_2	Length	Median Lambda	Multifractal	Monofractal	None
3	6	4	334.0445	536	37	1
2	6	5	329.7505	563	11	0
2	5	4	326.3375	508	66	0
3	5	3	321.1225	377	184	13
4	6	3	309.2645	456	97	21
2	4	3	306.4890	366	208	0
1	6	6	286.5105	571	3	0
1	5	5	276.3030	561	13	0
1	4	4	266.8320	539	35	0
1	3	3	242.8260	514	60	0
2	7	6	241.9570	298	146	130
3	7	5	236.0435	297	147	130
4	7	4	225.8515	296	148	130
1	7	7	219.8850	298	146	130
5	7	3	207.9350	287	153	134

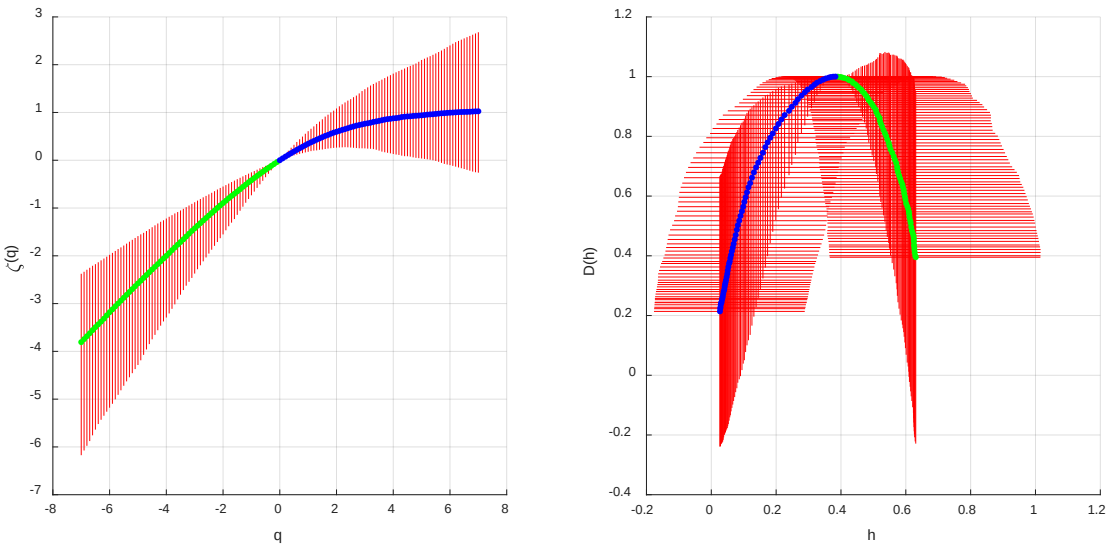

(a) (b)

Figure 5-67: (a) Scaling exponents, and (b) singularity spectrum for median values for levels 3-6 for the pipeline data corresponding to K_p index 3. Positive q values are blue, negative q values are green.

Table 5-55: Cumulant values for K_p index 3 for 2003 pipeline data for levels 3-6.

Cumulant	5%	50%	95%
c_1	0.2222	0.3829	0.6836
c_2	-0.2057	-0.0749	0.0271
c_3	-0.1930	-0.0088	0.0391
c_4	-0.2149	0.0020	0.1247
c_5	-0.1359	0.0027	0.4164

5.2.5 K_p index 4

K_p index 4 values occurred for 18.66% of the pipeline data available for 2003, for a total of 545 intervals. This corresponds to the state of active for the magnetosphere. The results for each individual range of the data are given in Table 5-56. From that we can see that range 3-6 had the greatest lambda value. The median scaling exponents and singularity spectrum with the 5%-95% error bars are given in Figure 5-68. From this, we can see a clear singularity spectrum with considerable variance in the error bars. The cumulant values are shown in Table 5-57.

Table 5-56: Results for each individual range for K_p index 4 for 2003 pipeline data.

j_1	j_2	Length	Median Lambda	Multifractal	Monofractal	None
3	6	4	328.0065	349	25	0
2	5	4	323.9210	325	49	0
2	6	5	322.8700	362	12	0
3	5	3	318.6560	223	149	2
2	4	3	308.4735	224	150	0
4	6	3	300.9845	302	65	7
1	6	6	288.8725	374	0	0
1	5	5	279.1770	364	10	0
1	4	4	266.6935	343	31	0
2	7	6	263.3990	208	76	90
3	7	5	261.7835	208	76	90
4	7	4	245.6120	204	80	90
1	3	3	242.4715	323	51	0
1	7	7	238.5710	208	76	90
5	7	3	223.3965	198	80	96

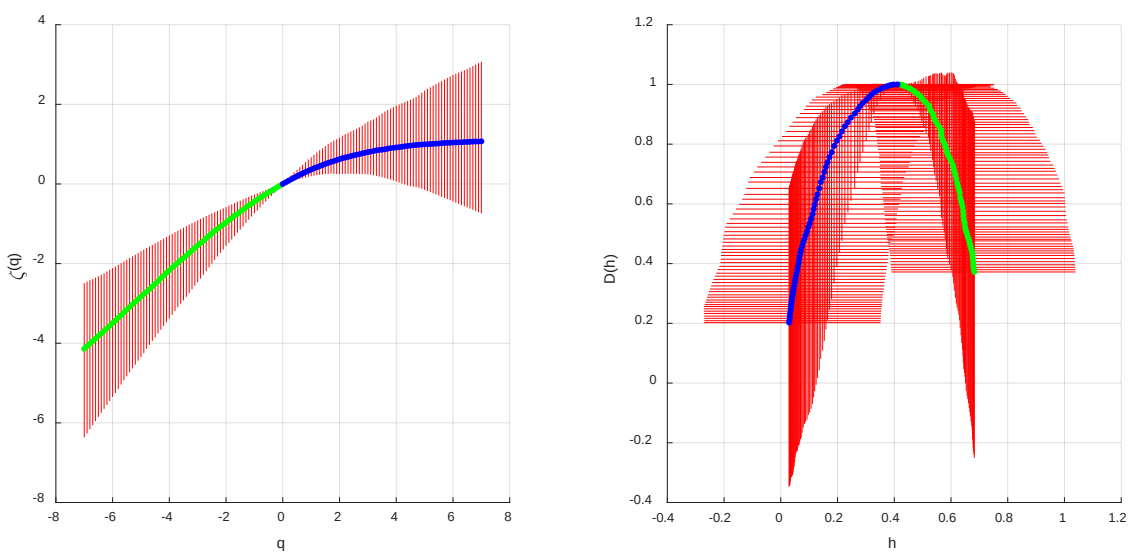

(a) (b)

Figure 5-68: (a) Scaling exponents, and (b) singularity spectrum for median values for levels 3-6 for the pipeline data corresponding to K_p index 4. Positive q values are blue, negative q values are green.

Table 5-57: Cumulant values for K_p index 4 for 2003 pipeline data for levels 3-6.

Cumulant	5%	50%	95%
c_1	0.2314	0.4111	0.7434
c_2	-0.2460	-0.0772	0.0312
c_3	-0.1880	-0.0066	0.0464
c_4	-0.1414	0.0014	0.0986
c_5	-0.1611	0.0010	0.4187

5.2.6 K_p index 5

K_p index 5 values occurred for 7.50% of the pipeline data available for 2003, for a total of 219 intervals. This index value corresponds to a minor storm. The results for each individual range of the data are given in Table 5-58. From that we can see that range 2-6 had the greatest lambda value. The median scaling exponents and singularity spectrum with the 5%-95% error bars are given in Figure 5-69. From this, we can see a clear singularity spectrum with considerable variance in the error bars. The cumulant values are shown in Table 5-59.

Table 5-58: Results for each individual range for K_p index 5 for 2003 pipeline data.

j_1	j_2	Length	Median Lambda	Multifractal	Monofractal	None
2	6	5	325.3825	143	5	0
2	5	4	324.6510	117	31	0
3	6	4	321.7430	136	12	0
3	5	3	306.4890	77	68	3
2	4	3	304.0725	75	73	0
4	6	3	303.2090	116	27	5
1	6	6	283.9250	145	3	0
1	5	5	275.7635	141	7	0
1	4	4	266.7250	131	17	0
2	7	6	259.4685	84	35	29
3	7	5	256.1735	84	35	29
4	7	4	246.8715	84	34	30
1	3	3	246.5500	122	26	0
5	7	3	229.0790	80	35	33
1	7	7	227.7870	84	35	29

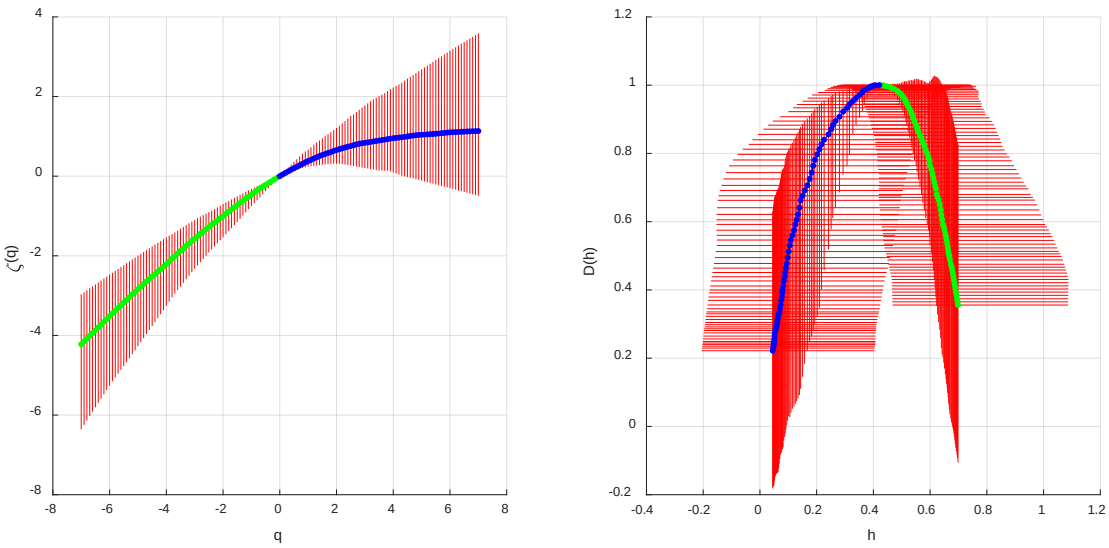

(a) (b)

Figure 5-69: (a) Scaling exponents, and (b) singularity spectrum for median values for levels 2-6 for the pipeline data corresponding to K_p index 5. Positive q values are blue, negative q values are green.

Table 5-59: Cumulant values for K_p index 5 for 2003 pipeline data for levels 2-6.

Cumulant	5%	50%	95%
c_1	0.2871	0.4206	0.7430
c_2	-0.2396	-0.0777	0.0093
c_3	-0.2418	-0.0092	0.0329
c_4	-0.2792	0.0002	0.0996
c_5	-0.1608	0.0019	0.5519

5.2.7 K_p index 6

K_p index 6 values occurred for 1.64% of the pipeline data available for 2003, for a total of 48 intervals. This corresponds to a moderate storm. The results for each individual range of the data are given in Table 5-60. From that we can see that range 3-6 had the greatest lambda value. The median scaling exponents and singularity spectrum with the 5%-95% error bars are given in Figure 5-70. The cumulant values are shown in Table 5-61. The median singularity spectrum is not as clear as the previous ones. It still retains a parabolic shape, but is jagged. This could be due to the fact that there are a much smaller number of intervals for this than for the previous ones.

Table 5-60: Results for each individual range for K_p index 6 for 2003 pipeline data.

			Median			
j_1	**j_2**	**Length**	**Lambda**	**Multifractal**	**Monofractal**	**None**
3	6	4	333.0380	25	3	0
2	6	5	322.5000	28	0	0
2	5	4	322.0650	18	10	0
3	5	3	319.6610	11	16	1
2	4	3	309.0640	15	13	0
4	6	3	302.3255	20	6	2
1	6	6	291.1785	28	0	0
2	7	6	283.3205	17	5	6
1	4	4	282.7660	27	1	0
1	5	5	280.9335	28	0	0
3	7	5	277.4125	17	5	6
4	7	4	265.7035	16	6	6
1	3	3	249.4775	23	5	0
5	7	3	249.4345	16	4	8
1	7	7	239.7030	17	5	6

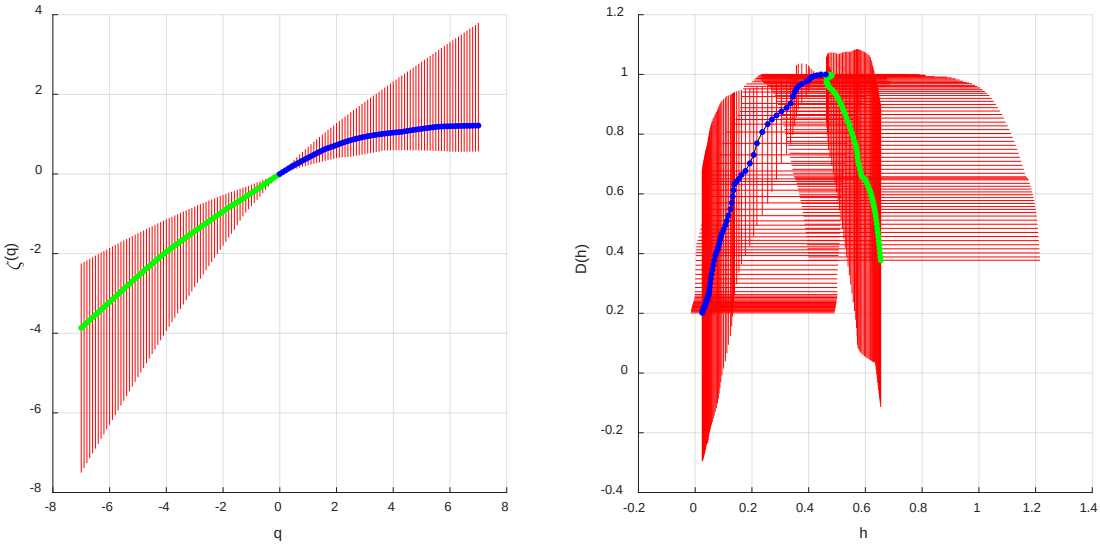

(a) (b)

Figure 5-70: (a) Scaling exponents, and (b) singularity spectrum for median values for levels 3-6 for the pipeline data corresponding to K_p index 6. Positive q values are blue, negative q values are green.

Table 5-61: Cumulant values for K_p index 6 for 2003 pipeline data for levels 3-6.

Cumulant	5%	50%	95%
c_1	0.2414	0.4604	0.7529
c_2	-0.2074	-0.0553	0.1087
c_3	-0.2567	-0.0218	0.2971
c_4	-0.4925	-0.0012	0.2298
c_5	-1.0102	0.0192	1.0576

5.2.8 K_p index 7

K_p index 7 values occurred for 0.62% of the pipeline data available for 2003, for a total of 18 intervals. This index value corresponds to a strong storm. The results for each individual range of the data are given in Table 5-62. From that we can see that range 3-6 had the greatest lambda value. The median scaling exponents and singularity spectrum with the 5%-95% error bars are given in Figure 5-71. The cumulant values are shown in Table 5-63. The median singularity spectrum isn't as clear as the previous ones. It still retains a parabolic shape, but is jagged. As with the K_p index 6 median singularity spectrum, this could be due to the fact that there are a much smaller number of intervals for this than for the previous ones. It is smoother than the K_p index 6 median singularity spectrum. This could mean that the K_p index 7 values are closer to each other than the K_p index 6 values.

Table 5-62: Results for each individual range for K_p index 7 for 2003 pipeline data.

j_1	j_2	Length	Median Lambda	Multifractal	Monofractal	None
3	6	4	321.7900	14	0	0
3	5	3	314.7950	7	7	0
3	7	5	312.1565	10	1	3
2	6	5	308.8370	14	0	0
4	7	4	303.2000	10	1	3
4	6	3	302.4495	12	1	1
2	5	4	299.9120	11	3	0
2	7	6	294.4200	10	1	3
1	3	3	290.1185	11	3	0
1	6	6	287.9285	14	0	0
1	5	5	277.9790	13	1	0
1	7	7	263.9930	10	1	3
1	4	4	262.4520	12	2	0
2	4	3	261.7820	8	6	0
5	7	3	237.9450	10	1	3

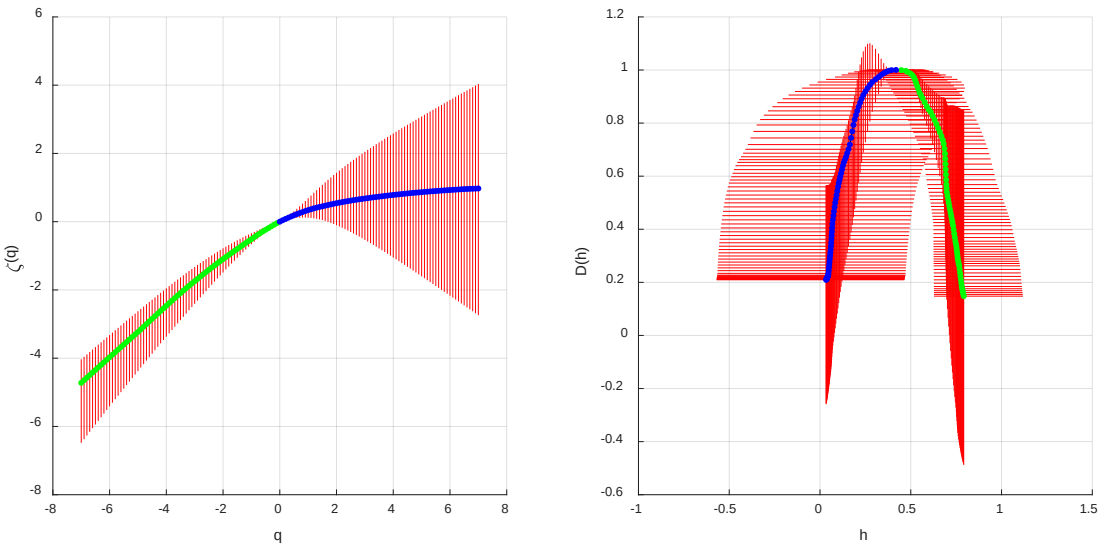

(a) (b)

Figure 5-71: (a) Scaling exponents, and (b) singularity spectrum for median values for levels 3-6 for the pipeline data corresponding to K_p index 7. Positive q values are blue, negative q values are green.

Table 5-63: Cumulant values for K_p index 7 for 2003 pipeline data for levels 3-6.

Cumulant	5%	50%	95%
c_1	0.2646	0.4183	0.5707
c_2	-0.4338	-0.1617	0.1654
c_3	-0.3673	0.0033	0.5892
c_4	-0.1396	0.0343	0.5981
c_5	-4.5397	-0.0127	2.3935

5.2.9 K_p index 8

K_p index 8 values occurred for 0.34% of the pipeline data available for 2003, for a total of 10 intervals. This index value is for a severe storm. The results for each individual range of the data are given in Table 5-64. From that we can see that range 2-6 had the greatest lambda value. The median scaling exponents and singularity spectrum with the 5%-95% error bars are given in Figure 5-72. The cumulant values are shown in Table 5-65. As with the K_p index 6 and 7 intervals, the median singularity spectrum isn't as smooth as the intervals that had more samples. It still retains a parabolic shape, but has some jaggedness.

Table 5-64: Results for each individual range for K Index 8 for 2003 pipeline data.

			Median			
j_1	j_2	Length	Lambda	Multifractal	Monofractal	None
2	6	5	339.9135	10	0	0
3	6	4	322.8275	10	0	0
2	5	4	317.8630	9	1	0
3	5	3	313.6105	7	3	0
4	6	3	309.4840	9	1	0
1	6	6	306.3930	10	0	0
1	5	5	299.7665	10	0	0
2	4	3	295.0955	9	1	0
1	4	4	290.1685	9	1	0
1	3	3	264.4885	7	3	0
5	7	3	50.4035	1	4	5
4	7	4	49.4430	1	3	6
3	7	5	47.7860	1	4	5
2	7	6	46.3460	1	4	5
1	7	7	45.1635	1	4	5

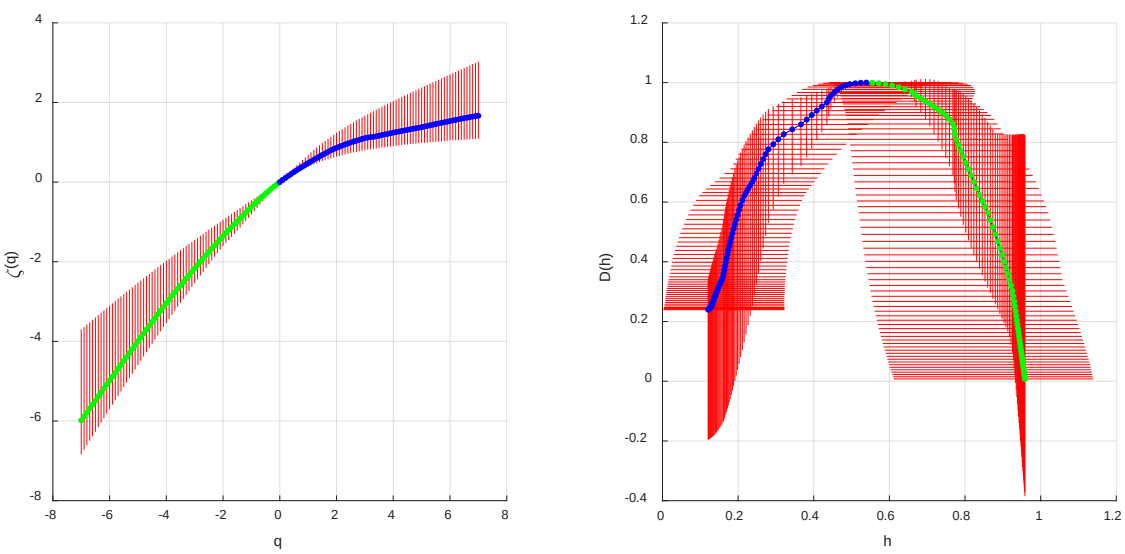

(a) (b)

Figure 5-72: (a) Scaling exponents, and (b) singularity spectrum for median values for levels 2-6 for the pipeline data corresponding to K_p index 8. Positive q values are blue, negative q values are green.

Table 5-65: Cumulant values for K_p index 8 for 2003 pipeline data for levels 2-6.

Cumulant	5%	50%	95%
c_1	0.4442	0.5392	0.7654
c_2	-0.2249	-0.1154	-0.0307
c_3	-0.2024	-0.0071	0.0781
c_4	-0.3010	-0.0017	0.2754
c_5	-0.2080	-0.0002	0.5158

5.2.10 K_p index 9

K_p index 9 has the least amount of values of all of them, with 3 intervals that compromised 0.10% of the pipeline data available for 2003. This index value correspond to an extreme storm. The results for each individual range of the data are given in Table 5-66. From that we can see that range 4-6 had the greatest lambda value. The median scaling exponents and singularity spectrum with the 5%-95% error bars are given in Figure 5-73. The cumulant values are shown in Table 5-67. Due to the very small number of K_p index 9 intervals, the median singularity spectrum is very asymmetric and has some jaggedness.

Table 5-66: Results for each individual range for K_p index 9 for 2003 pipeline data.

j_1	j_2	Length	Median Lambda	Multifractal	Monofractal	None
4	6	3	327.2700	2	0	1
3	6	4	314.4640	3	0	0
2	6	5	307.8400	3	0	0
2	5	4	305.2330	1	2	0
3	5	3	298.3150	0	3	0
1	4	4	293.2240	2	1	0
1	6	6	291.7780	3	0	0
1	5	5	290.7370	3	0	0
2	4	3	285.8970	1	2	0
1	3	3	274.7530	2	1	0
5	7	3	110.0690	1	0	2
4	7	4	101.3130	1	0	2
3	7	5	93.8230	1	0	2
2	7	6	84.8590	1	0	2
1	7	7	79.6200	1	0	2

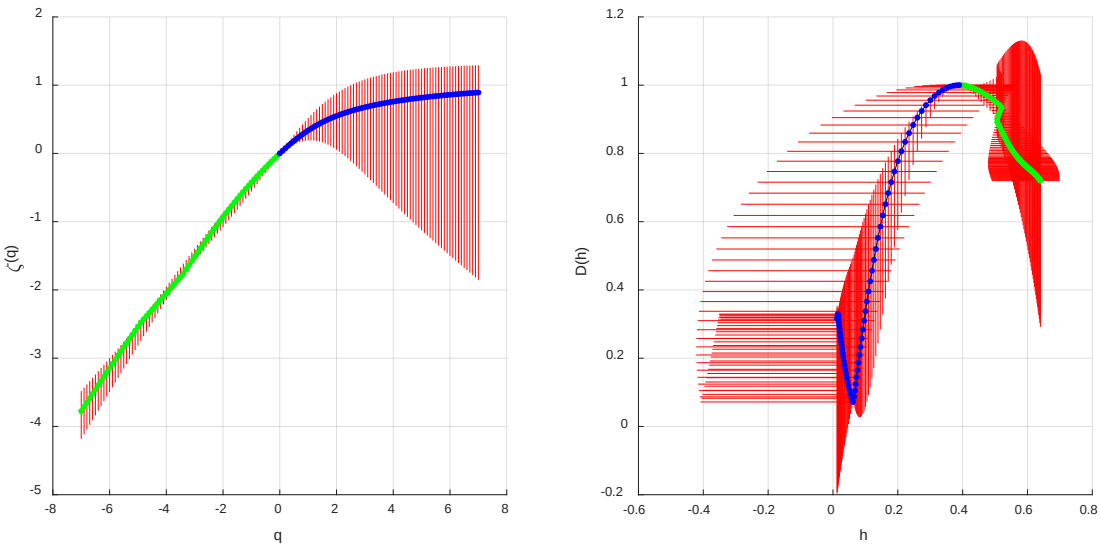

(a) (b)

Figure 5-73: (a) Scaling exponents, and (b) singularity spectrum for median values for levels 4-6 for the pipeline data corresponding to K_p index 9. Positive q values are blue, negative q values are green.

Table 5-67: Cumulant values for K_p index 9 for 2003 pipeline data for levels 4-6.

Cumulant	5%	50%	95%
c_1	0.3193	0.3894	0.5613
c_2	-0.2044	-0.0718	-0.0638
c_3	-0.1699	-0.1490	-0.0895
c_4	-0.1192	-0.0729	-0.0288
c_5	0.2045	0.3155	0.4625

5.2.11 K_p results

Most of the levels selected by the automated range selection algorithm were from 3-6. The median cumulant values for that range are in Table 5-68 and the graphs of that are in Figure 5-74 with 5% and 95% error bars. The c_1 values correspond to the apex of the singularity spectrum. From the graphs, we can see that there is an overall trend towards greater c_1 values as the K_p index increases. What this means is that the dimension increases as the K_p index increases, yielding increasing system order, with significant variance of course.

Table 5-68: Median cumulant values by K_p index for 2003 data for levels 3-6.

	K_p index									
	0	**1**	**2**	**3**	**4**	**5**	**6**	**7**	**8**	**9**
c_1	0.3054	0.3125	0.3548	0.3829	0.4111	0.3949	0.4604	0.4183	0.4904	0.5140
c_2	-0.0403	-0.0601	-0.0696	-0.0749	-0.0772	-0.0731	-0.0553	-0.1617	-0.1263	-0.1310
c_3	-0.0054	-0.0059	-0.0084	-0.0088	-0.0066	-0.0128	-0.0218	0.0033	-0.0079	-0.0407
c_4	-0.0007	0.0009	0.0010	0.0020	0.0014	-0.0004	-0.0012	0.0343	0.0006	-0.1077
c_5	-0.0001	0.0007	0.0025	0.0027	0.0010	0.0021	0.0192	-0.0127	-0.0002	0.0853

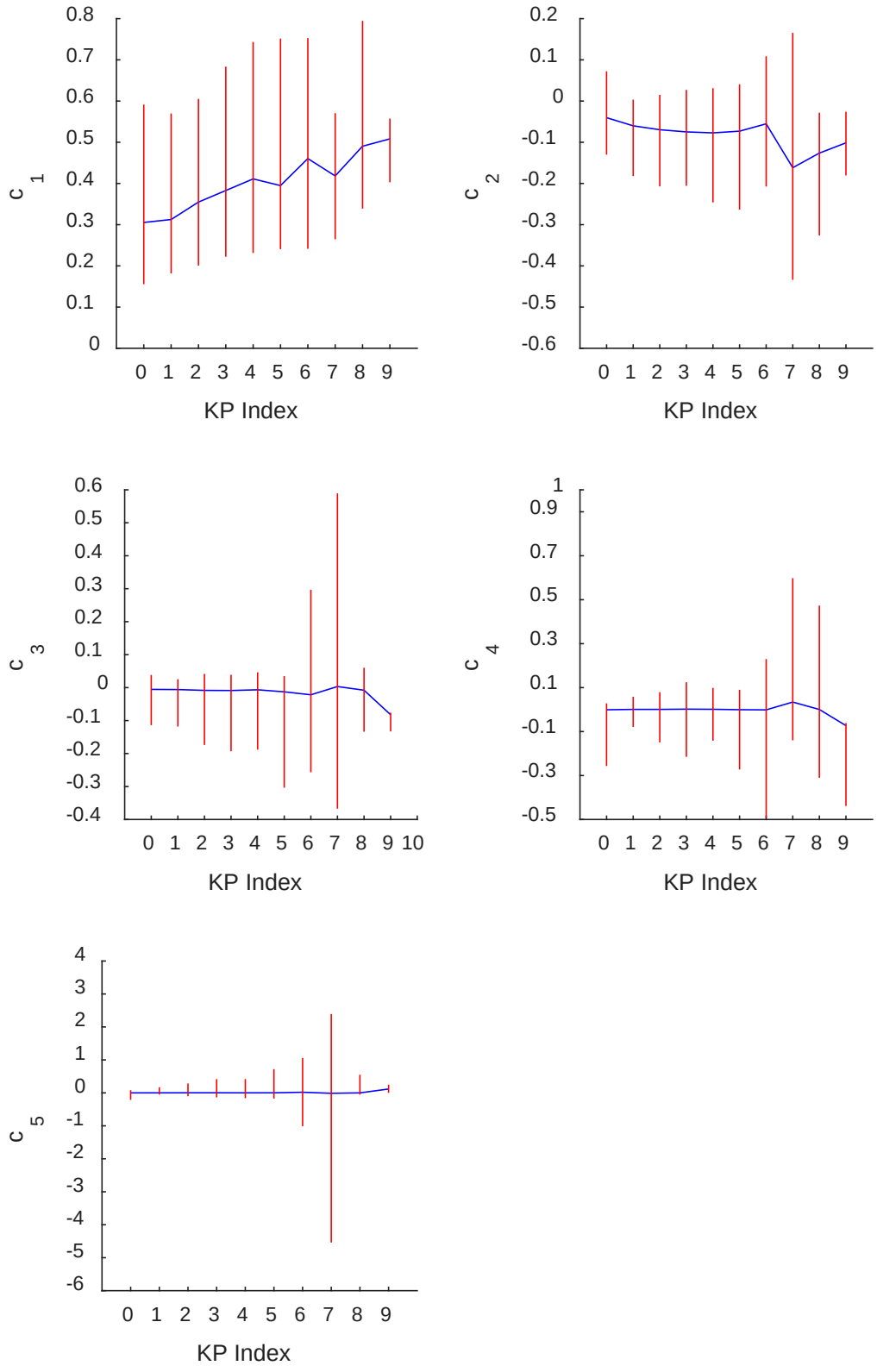

Figure 5-74: Median cumulants and 5%-95% error bars by K_p index for levels 3-6

Chapter 6 Conclusions and Future Work

Signals were analyzed both as individual days and as individual 3-hour segments correlated to their K_p index values. We showed that they many of them exhibit multifractal characteristics using the bootstrap method and surrogate data analysis with others having monofractal characteristics. They are the end result of a chain of interactions of the sun with Earth's magnetosphere, many of which are multifractal. The challenge is to understand the characteristics of these interactions and predict their impact on the ground. The singularity spectrum of GIC current at one location has been analyzed over several different times. In the future different GIC currents at different latitudes should be analyzed at the same time, along with space-based observations. Their singularity spectrums can be compared individually and a joint singularity spectrum can be calculated. In addition, days can be combined and a sliding window implemented to capture how multifractality can change over other time periods. This would require much more computation power and thus take longer to process. The advantage is that it would give us analysis for prestorm, storm, and recovery periods. Surrogate analysis also showed that the characteristics for most of the signals analyzed are independent of their Fourier properties or the individual data points themselves.

Different days had different singularity spectrums. This could be due to the combination of various monofractal and multifractal processes present in the magnetosphere, the ionosphere, and the heliosphere. This can give us some idea about how these various processes combine and it turn, gives us information about the structure and dynamics of the heliosphere-magnetosphere-ionosphere and how it changes with time.

Each 3-hour interval of the pipeline data series was correlated with an integer K_p index value and the median singularity spectrum and cumulants values were computed for that interval. What was found was that the range with the largest lambda value was range 3-6 at the upper levels of the discrete wavelet transform, and that the first cumulant value showed a trend towards higher values as the K_p index increased, with a large amount of variance. This seems that a geomagnetic storm pushes the system towards greater amounts of order and long-range memory, which could mean that as solar activity increases, its effects overpower the effects of other multifractal processes that are present in the magnetosphere and ionosphere. This was not really

observed in the individual day analysis due to the few instances that were computed and analyzed.

In this dissertation, only one year has been analyzed in the 11-year solar cycle. In the future, all the years will be analyzed and a comparison between them will be carried out at different parts of the solar cycle, from minimum to maximum. The magnetism of the sun reverses every 11-year solar cycle, so another 11-year cycle will be analyzed as well to compare results of the interaction of different orientations of the magnetized plasma of the solar wind with Earth's magnetosphere.

Current methods to mitigate GIC are insufficient. For pipelines, as stated in the introduction, the current needs to be maintained between -850 and -1150 mA with respect to ground. Let us assume that we apply current to the pipeline that is at the mid-point of that which is -1000 mA. Current from GIC exceeding ± 150 mA will take the total current out of the desired range for the pipeline. This was exceeded in the pipeline current data 45.75% of the time in the 257 days measured, with the current exceeding one amp 3.57% of the time. Multifractal analysis can give us better modeling capabilities so that we can provide a counter current to mitigate GIC and keep the current on the pipeline in the desired range. Power networks often treat GIC as DC currents and install blocking capacitors. However, they are really very low frequency currents with multifractal characteristics and blocking capacitors have at least in certain cases made the problem worse. In addition, the effects of fractal current on components are unknown. It could have no impact, or it could increase component failure. This needs to be researched further. Understanding the multifractal characteristics of these currents can aid in building better filters for them and mitigating their effects.

Currently, the automated range selection algorithm selects the range with the largest lambda. However, certain datasets seem to have different multifractality over adjacent wavelet levels. In the future, the algorithm will be provided with the ability to find these extra ranges of wavelet levels. Certain days had better singularity spectrums with wavelet levels that were not at the maximum but near it. The automated range selection algorithm needs to take into account how well formed the singularity spectrum is as well.

Wavelet leaders make use of the discrete wavelet transform with the decimation step. One potential future area of research is to analyze the effects of removing the decimation step,

which allows us to use the stationary wavelet transform. One advantage of the stationary wavelet transform is that it yields improved noise filtering.

The selection of the vanishing moment of the wavelet can have an effect on the singularity spectrum that is estimated. In the cases that were analyzed in this dissertation, the singularity spectrum was mostly consistent across all the vanishing moments that were selected. However, the automated range selection algorithm selected different ranges of wavelet levels and produced differences in the singularity spectrum. One potential avenue of research is to update the range selection algorithm to not only consider the wavelet levels to be selected but the vanishing moments as well. The same lambda metrics can be considered as well as maximum length for each vanishing moment.

Wavelet leaders with bootstrap proved to be a good tool to use for singularity spectrum analysis of GIC data. There are other techniques that also estimate the singularity spectrum of a signal. Among these are Rank Ordering Multifractal Analysis (ROMA) and Multifractal Detrended Fluctuation Analysis (MFDFA) that was used in this dissertation. A full-scale comparison of all known techniques needs to be performed. In addition, the bootstrap methods should be implemented with MFDFA and ROMA in order to do statistical hypothesis testing as is now done with the wavelet leader method. Surrogate analysis testing beyond just IAAFT and shuffle data points needs to be implemented with these methods as well. MFDFA provided confirmation in some instances of multifractal behavior of GIC data, but in other instances the results differed in either the positive q or negative q values or both. This needs to be analyzed further.

When dealing with signals that come from outside sources, there is usually a noise component encountered. Usually all or part of it is assumed to be white Gaussian noise. The white noise model may be used as an approximation for some of the actual realizations encountered in nature. The name comes from the fact that in the ideal case it occurs equally at all frequencies (white) and follows a random Gaussian distribution. Each sample is independent of all the other samples, which makes its autocorrelation function have an instant decay to 0, making it the Dirac delta impulse.

The wavelet transform can be used to remove white gaussian noise, however this was found to distort the singularity spectrum that corresponds to the negative q values, which represent the smallest fluctuations. In the future, the performance of all the multifractal

estimators need to be analyzed for a synthetic signal both in the presence of noise and after the removal of that noise with filtering to determine how to deal with noise in real life multifractal datasets.

The ultimate goal is to be able to forecast space weather as we do terrestrial weather, which would be helpful to prediction and dealing with the impacts of GIC. Multifractal analysis along with other methods of analysis can provide insights in these processes and increase our understanding of them to achieve that goal. However, there are several challenges, including a lack of understanding of the processes in the heliosphere, magnetosphere, and ionosphere, and a smaller number of sensor data than we have for terrestrial weather due to considerable distances involved. We are just at the beginning of understanding space weather.

References

[1] W. Gonzalez and E. N. Parker, *Magnetic Reconnection : Concepts and Applications* (Astrophysics and Space Science Library). Cham: Springer, 2016.

[2] J. T. Gosling, "The solar flare myth," *Journal of Geophysical Research: Space Physics*, vol. 98, no. A11, pp. 18937-18949, 1993.

[3] D. H. Boteler, "The super storms of August/September 1859 and their effects on the telegraph system," *Advances in Space Research*, vol. 38, no. 2, pp. 159-172, 2006.

[4] P. C. Frisch, *Solar journey: the significance of our galactic environment for the heliosphere and earth* (Astrophysics and space science library). Dordrecht: Springer, 2006.

[5] Y. Kamide and A. C. L. Chian, *Handbook of the solar-terrestrial environment*. Berlin ; New York: Springer, 2007, pp. xiv, 539 p.

[6] K. Brown. (2019, October 12, 2019). *NASA Spacecraft Launches on Mission to Explore Frontier of Space* Available: https://www.nasa.gov/press-release/nasa-spacecraft-launches-on-mission-to-explore-frontier-of-space

[7] J. Bartels, N. H. Heck, and H. F. Johnston, "The three-hour-range index measuring geomagnetic activity," *Terrestrial Magnetism and Atmospheric Electricity*, vol. 44, no. 4, pp. 411-454, 1939.

[8] W. M. Macek, "Chaos and multifractals in the solar wind," *Advances in Space Research*, vol. 46, no. 4, pp. 526-531, 2010.

[9] P. Bak, *How nature works : the science of self-organized criticality / Per Bak* (no. Accessed from https://nla.gov.au/nla.cat-vn2804763). New York, NY, USA: Copernicus, 1996.

[10] A. Haar, "Zur Theorie der orthogonalen Funktionensysteme," *Mathematische Annalen*, vol. 69, no. 3, pp. 331-371, 1910.

[11] J. B. J. Fourier, *Théorie analytique de la chaleur*. 1822.

[12] M. T. Heideman, D. H. Johnson, and C. S. Burrus, "Gauss and the History of the Fast Fourier Transform," *Archive for History of Exact Sciences*, vol. 34, no. 3, pp. 265-277, 1985.

[13] A. T. Y. Lui, "Multiscale phenomena in the near-Earth magnetosphere," *Journal of Atmospheric and Solar-Terrestrial Physics*, vol. 64, no. 2, pp. 125-143, 2002/01/01/ 2002.

[14] S. Ohtani, T. Higuchi, A. T. Y. Lui, and K. Takahashi, "Magnetic fluctuations associated with tail current disruption: Fractal analysis," *Journal of Geophysical Research: Space Physics*, vol. 100, no. A10, pp. 19135-19145, 1995.

[15] I. Daubechies, "The wavelet transform, time-frequency localization and signal analysis," *Information Theory, IEEE Transactions on*, vol. 36, no. 5, pp. 961-1005, 1990.

[16] I. Daubechies and J. C. Lagarias, "Two-Scale Difference Equations. I. Existence and Global Regularity of Solutions," *SIAM Journal on Mathematical Analysis*, vol. 22, no. 5, pp. 1388-1410, 1991.

[17] I. Daubechies and J. C. Lagarias, "Two-Scale Difference Equations II. Local Regularity, Infinite Products of Matrices and Fractals," *SIAM Journal on Mathematical Analysis*, vol. 23, no. 4, pp. 1031-1079, 1992.

[18] I. Daubechies, *Ten lectures on wavelets* (CBMS-NSF regional conference series in applied mathematics, no. 61). Philadelphia, Pa.: Society for Industrial and Applied Mathematics, 1992, pp. xix, 357 p.

[19] B. Adhikari, *Analysis of Geomagnetic Storms Using Wavelet Transforms*. 2017, pp. 119-124.

[20] M. J. A. Bolzan, R. R. Rosa, and Y. Sahai, "Multifractal analysis of low-latitude geomagnetic fluctuations," *Ann. Geophys.*, vol. 27, no. 2, pp. 569-576, 2009.

[21] M. Bolzan and R. Rosa, *Multifractal analysis of interplanetary magnetic field obtained during CME events*. 2012, pp. 1107-1112.

[22] M. J. A. Bolzan, A. Tardelli, V. G. Pillat, P. R. Fagundes, and R. R. Rosa, "Multifractal analysis of vertical total electron content (VTEC) at equatorial region and low latitude, during low solar activity," *Ann. Geophys.*, vol. 31, no. 1, pp. 127-133, 2013.

[23] S. Gopinath, "Multifractal features of magnetospheric dynamics and their dependence on solar activity," *Astrophysics and Space Science*, journal article vol. 361, no. 9, p. 290, 2016.

[24] P. Abry, S. p. Jaffard, and B. Lashermes, "Revisiting scaling, multifractal, and multiplicative cascades with the wavelet leader lens," in *Proc. SPIE*, 2004, vol. 5607, no. Wavelet Applications in Industrial Processing II, pp. 103-117.

[25] B. Lashermes, S. Jaffard, and P. Abry, "Wavelet leader based multifractal analysis," in *Acoustics, Speech, and Signal Processing, 2005. Proceedings. (ICASSP '05). IEEE International Conference on*, 2005, vol. 4, pp. iv/161-iv/164 Vol. 4.

[26] S. Jaffard, B. Lashermes, and P. Abry, "Wavelet Leaders in Multifractal Analysis," in *Wavelet Analysis and Applications*, T. Qian, M. I. Vai, and Y. Xu, Eds. Basel: Birkhäuser Basel, 2007, pp. 201-246.

[27] H. Wendt and P. Abry, "Multifractality Tests Using Bootstrapped Wavelet Leaders," *Signal Processing, IEEE Transactions on*, vol. 55, no. 10, pp. 4811-4820, 2007.

[28] B. Efron, "Bootstrap Methods: Another Look at the Jackknife," *The Annals of Statistics*, vol. 7, no. 1, pp. 1-26, 1979.

[29] G. Lancaster, D. Iatsenko, A. Pidde, V. Ticcinelli, and A. Stefanovska, "Surrogate data for hypothesis testing of physical systems," *Physics Reports*, vol. 748, pp. 1-60, 2018/07/18/ 2018.

[30] L. F. Richardson, *Weather Prediction by Numerical Process*, 2 ed. (Cambridge Mathematical Library). Cambridge: Cambridge University Press, 2007.

[31] J. Lilensten, Ed. *Space Weather: Research Towards Applications in Europe*. Springer, 2007.

[32] A. Pulkkinen and R. Kataoka, "S-transform view of geomagnetically induced currents during geomagnetic superstorms," *Geophysical Research Letters*, vol. 33, no. 12, pp. n/a-n/a, 2006.

[33] A. Pulkkinen, A. Klimas, D. Vassiliadis, V. Uritsky, and E. Tanskanen, "Spatiotemporal scaling properties of the ground geomagnetic field variations," *Journal of Geophysical Research: Space Physics*, vol. 111, no. A3, pp. n/a-n/a, 2006.

[34] K. Wirsing and L. Mili, "Multifractal analysis of geomagnetically induced currents using wavelet leaders," *Journal of Applied Geophysics*, vol. 173, p. 103920, 2020/02/01/ 2020.

[35] Houghton Mifflin Company., *The American Heritage College Dictionary*, 3rd ed. Boston: Houghton Mifflin, 1993, pp. xxxiv, 1630 p.

[36] W. B. Cade and C. Chan-Park, "The Origin of "Space Weather"," *Space Weather*, vol. 13, no. 2, pp. 99-103, 2015.

[37] J. F. W. Herschel, *Results of astronomical observations made during the years 1834, 5, 6, 7, 8, at the Cape of Good Hope; being the completion of a telescopic survey of the whole surface of the visible heavens, commenced in 1825*. London,: Smith, Elder and Co., 1847, pp. 1 p. l., xx, 452, 2 p.

[38] J. Phillips, "On Isoclinal Magnetic Lines in Yorkshire," *Report of the British Association for the Advancement of Science*, vol. 20th Meeting (1850), no. Report of the British Association for the Advancement of Science, 1850.
[39] "Probe Space "Weather"," *The Science News-Letter*, vol. 71, no. 26, pp. 403-403, 1957.
[40] E. Parker, "Extension of the solar corona into interplanetary space," *Journal of Geophysical Research*, vol. 64, no. 11, pp. 1675-1681, 1959.
[41] "Chart Space "Weather"," *The Science News-Letter*, vol. 76, no. 15, pp. 229-229, 1959.
[42] R. M. Robinson and R. A. Behnke, "The U.S. National Space Weather Program: A Retrospective," in *Space Weather*: American Geophysical Union, 2013, pp. 1-10.
[43] W. Walter, "Flares Menace Astronauts," *The Science News-Letter*, vol. 85, no. 7, pp. 99-99, 1964.
[44] *Storms from the Sun: The Emerging Science of Space Weather*. Washington, DC: The National Academies Press, 2002, p. 256.
[45] M. G. Kivelson and C. T. Russell, *Introduction to space physics*. Cambridge ; New York: Cambridge University Press, 1995, pp. xv, 568 p.
[46] E. Chaisson and S. McMillan, *Astronomy today*, 3rd ed. Upper Saddle River, N.J.: Prentice Hall, 1999.
[47] H. Schwabe, "Sonnenbeobachtungen im Jahre 1843. Von Herrn Hofrath Schwabe in Dessa," *Astronomische Nachrichten*, vol. 21, p. 233, 1844.
[48] E. Sabine, "On Periodical Laws Discoverable in the Mean Effects of the Larger Magnetic Disturbances. No. II," *Philosophical Transactions of the Royal Society of London*, vol. 142, pp. 103-124, January 1, 1852 1852.
[49] T. Phillips. (2008, March 21, 2017). *Solar Cycle 24 Begins*. Available: https://science.nasa.gov/science-news/science-at-nasa/2008/10jan_solarcycle24/
[50] T. Howard, "Introduction," in *Coronal Mass Ejections: An Introduction*New York, NY: Springer New York, 2011, pp. 1-18.
[51] A. J. Hundhausen, "Sizes and locations of coronal mass ejections: SMM observations from 1980 and 1984-1989," *Journal of Geophysical Research: Space Physics (1978–2012)*, vol. 98, no. A8, pp. 13177-13200, 1993.
[52] A. J. Hundhausen, J. T. Burkepile, and O. C. St. Cyr, "Speeds of coronal mass ejections: SMM observations from 1980 and 1984-1989," *Journal of Geophysical Research: Space Physics*, vol. 99, no. A4, pp. 6543-6552, 1994.
[53] R. A. Harrison, E. Hildner, A. J. Hundhausen, and D. G. Sime, "The launch of solar coronal mass ejections: Results from the coronal mass ejection onset program," *Journal of geophysical research. A, Space physics*, vol. 95, no. a2, p. 917, 1990.
[54] H. Zell. (2014, February 6, 2018). *CME Week: The Difference Between Flares and CMEs*. Available: https://www.nasa.gov/content/goddard/the-difference-between-flares-and-cmes
[55] S. W. Kahler, "Solar Flares and Coronal Mass Ejections," *Annual Review of Astronomy and Astrophysics*, vol. 30, no. 1, pp. 113-141, 1992.
[56] D. H. Hathaway. (2014, February 5, 2018). *Coronal Mass Ejections*. Available: https://solarscience.msfc.nasa.gov/CMEs.shtml
[57] I. A. Daglis, "Space Storms, Ring Current and Space-Atmosphere Coupling," in *Space Storms and Space Weather Hazards*, I. A. Daglis, Ed. Dordrecht: Springer Netherlands, 2001, pp. 1-42.
[58] S. Chapman, "The equatorial electrojet as detected from the abnormal electric current distribution above Huancayo, Peru, and elsewhere," *Archiv für Meteorologie, Geophysik und Bioklimatologie, Serie A*, journal article vol. 4, no. 1, pp. 368-390, August 01 1951.
[59] S. Chapman and J. Bartels, *Geomagnetism*. New York: Oxford University Press, 1940.
[60] J. A. Fejer, "Theory of auroral electrojets," *Journal of Geophysical Research*, vol. 68, no. 8, pp. 2147-2157, 1963.
[61] B. Zolesi and L. R. Cander, "The General Structure of the Ionosphere," in *Ionospheric Prediction and Forecasting*Berlin, Heidelberg: Springer Berlin Heidelberg, 2014, pp. 11-48.
[62] Google, "Locations of Magnetic Observatories," ed, 2020.
[63] IAGA. (1986). *IAGA Bulletin Number 40*. Available: http://wdc.kugi.kyoto-u.ac.jp/dstdir/dst2/onDstindex.html
[64] M. Sugiura, "Hourly values of equatorial Dst for the IGY," 1963, Available: http://hdl.handle.net/2060/19650020355.
[65] B. V. Kiselev, "R/S analysis of the Dst index," *Geomagnetism and Aeronomy*, vol. 57, no. 3, pp. 326-334, 2017// 2017.
[66] (2015, November 2, 2017). *Auroral Electrojet (AE, AL, AO, AU) - A Global Measure of Auroral Zone Magnetic Activity*. Available: https://catalog.data.gov/dataset/auroral-electrojet-ae-al-ao-au-a-global-measure-of-auroral-zone-magnetic-activity
[67] T. N. Davis and M. Sugiura, "Auroral electrojet activity index AE and its universal time variations," *Journal of Geophysical Research*, vol. 71, no. 3, pp. 785-801, 1966.
[68] (January 20, 2020). *The Kp-index*. Available: https://www.spaceweatherlive.com/en/help/the-kp-index
[69] T. I. Gombosi, D. N. Baker, A. Balogh, P. J. Erickson, J. D. Huba, and L. J. Lanzerotti, "Anthropogenic Space Weather," *Space Science Reviews*, 2017/04/13 2017.
[70] State Department. (1963). *Treaty Banning Nuclear Weapon Tests in the Atmosphere, in Outer Space and Under Water*. Available: https://2009-2017.state.gov/t/isn/4797.htm
[71] NASA. (1964). *NASA TN D-2402 Effects of High Altitude Explosions*.
[72] T. Phillips. (2017, November 5, 2017). *What's up in space, May 18, 2017*. Available: http://spaceweather.com/archive.php?view=1&day=18&month=05&year=2017
[73] W. H. Barlow, "On the Spontaneous Electrical Currents Observed in the Wires of the Electric Telegraph," *Philosophical Transactions of the Royal Society of London*, vol. 139, pp. 61-72, 1849.
[74] A. G. McNish, "The magnetic storm of March 24, 1940," *Terrestrial Magnetism and Atmospheric Electricity*, vol. 45, no. 3, pp. 359-364, 1940.
[75] S. Guillon, P. Toner, L. Gibson, and D. Boteler, "A Colorful Blackout: The Havoc Caused by Auroral Electrojet Generated Magnetic Field Variations in 1989," *IEEE Power and Energy Magazine*, vol. 14, no. 6, pp. 59-71, 2016.
[76] J. G. Kappenman, "An Introduction to Power Grid Impacts and Vulnerabilities from Space Weather," in *Space Storms and Space Weather Hazards*, I. A. Daglis, Ed. Dordrecht: Springer Netherlands, 2001, pp. 335-361.
[77] R. Pirjola, K. Kauristie, H. Lappalainen, A. Viljanen, and A. Pulkkinen, "Space weather risk," *Space Weather*, vol. 3, no. 2, p. S02A02, 2005.
[78] "IEEE Guide for Establishing Power Transformer Capability while under Geomagnetic Disturbances," *IEEE Std C57.163-2015*, pp. 1-50, 2015.

[79] I. A. Erinmez, J. G. Kappenman, and W. A. Radasky, "Management of the geomagnetically induced current risks on the national grid company's electric power transmission system," *Journal of Atmospheric and Solar-Terrestrial Physics,* vol. 64, no. 5–6, pp. 743-756, 2002.
[80] R. A. Gummow and P. Eng, "GIC effects on pipeline corrosion and corrosion control systems," *Journal of Atmospheric and Solar-Terrestrial Physics,* vol. 64, no. 16, pp. 1755-1764, 2002.
[81] D. H. Boteler, "Geomagnetic effects on the pipe-to-soil potentials of a continental pipeline," *Advances in Space Research,* vol. 26, no. 1, pp. 15-20, 2000/01/01/ 2000.
[82] N. G. Ptitsyna, V. V. Kasinskii, G. Villoresi, N. N. Lyahov, L. I. Dorman, and N. Iucci, "Geomagnetic effects on mid-latitude railways: A statistical study of anomalies in the operation of signaling and train control equipment on the East-Siberian Railway," *Advances in Space Research,* vol. 42, no. 9, pp. 1510-1514, 2008.
[83] E. A. Eroshenko *et al.*, "Effects of strong geomagnetic storms on Northern railways in Russia," *Advances in Space Research,* vol. 46, no. 9, pp. 1102-1110, 2010.
[84] A. Geist, "Supercomputing's monster in the closet," *IEEE Spectrum,* vol. 53, no. 3, pp. 30-35, 2016.
[85] D. J. Knipp, B. J. Fraser, M. A. Shea, and D. F. Smart, "On the Little-Known Consequences of the 4 August 1972 Ultra-Fast Coronal Mass Ejecta: Facts, Commentary, and Call to Action," *Space Weather,* vol. 0, no. 0.
[86] G. Prölss and M. K. Bird, *Physics of the Earth's Space Environment: An Introduction*. Springer, 2004.
[87] W. D. Compton and C. D. Benson, *Living and working in space : a history of Skylab* (The NASA history series, no. 4208). Washington, D.C.: Scientific and Technical Information Branch For sale by the Supt. of Docs., U.S. G.P.O., 1983, pp. xiii, 449 p.
[88] B. B. Mandelbrot, *Les objets fractals : forme, hasard et dimension / Benoit Mandelbrot* (Nouvelle bibliotheque scientifique, no. Accessed from http://nla.gov.au/nla.cat-vn2216320). Paris: Flammarion, 1975.
[89] G. Peano, "Sur une courbe, qui remplit toute une aire plane," *Mathematische Annalen,* vol. 36, pp. 157-160, 1890.
[90] D. Hilbert, "Ueber die stetige Abbildung einer Line auf ein Flächenstück," *Mathematische Annalen,* vol. 38, no. 3, pp. 459-460, 1891.
[91] H. Koch, "Une méthode géométrique élémentaire pour l'étude de certaines questions de la théorie des courbes planes," (in French), *Acta Mathematica,* vol. 30, no. 1, pp. 145-174, 1906/12/01 1906.
[92] K. J. Falconer, *Fractal geometry : mathematical foundations and applications*, 2nd ed. Chichester, England: Wiley, 2003, pp. xxvii, 337 p.
[93] T. Gowers, J. Barrow-Green, I. Leader, and Princeton University., *The Princeton companion to mathematics*. Princeton: Princeton University Press, 2008, pp. xx, 1034 p.
[94] S. Jaffard and C. Mélot, "Wavelet Analysis of Fractal Boundaries. Part 1: Local Exponents," *Communications in Mathematical Physics,* journal article vol. 258, no. 3, pp. 513-539, 2005.
[95] K. Knopp and F. Bagemihl, *Theory of functions*. New York,: Dover publications, 1945.
[96] S. Mallat and W. L. Hwang, "Singularity detection and processing with wavelets," *IEEE Trans. Inf. Theor.,* vol. 38, no. 2, pp. 617-643, 1992.
[97] B. B. Mandelbrot, *The fractal geometry of nature*. San Francisco: W.H. Freeman, 1982.
[98] M. R. Schroeder, *Fractals, chaos, power laws : minutes from an infinite paradise*. New York: W.H. Freeman, 1991, pp. xviii, 429 p., 8 p. of plates.
[99] T. C. Halsey, M. H. Jensen, L. P. Kadanoff, I. Procaccia, and B. I. Shraiman, "Fractal measures and their singularities: The characterization of strange sets," *Nuclear Physics B - Proceedings Supplements,* vol. 2, no. 0, pp. 501-511, 1987.
[100] S. G. Mallat, *A wavelet tour of signal processing : the sparse way*. Amsterdam; Boston: Elsevier/Academic Press, 2009.
[101] U. Frisch, "Fully Developed Turbulence and Intermittency," *Annals of the New York Academy of Sciences,* vol. 357, no. 1, pp. 359-367, 1980.
[102] J. Y. Stein, *Digital signal processing : a computer science perspective* (Wiley series in telecommunications and signal processing). New York: Wiley, 2000, pp. xx, 859 p.
[103] K. Wirsing, "Application of Wavelets to Filtering and Analysis of Self-Similar Signals," Master of Science, Electrical and Computer Engineering, Virginia Polytechnic Institute and State University, 2014.
[104] A. Grossmann and J. Morlet, "Decomposition of Hardy Functions into Square Integrable Wavelets of Constant Shape," *SIAM Journal on Mathematical Analysis,* vol. 15, no. 4, pp. 723-736, 1984.
[105] C. Valens, "A Really Friendly Guide to Wavelets," Available: http://www.robots.ox.ac.uk/~parg/mlrg/papers/arfgtw.pdf
[106] A. Scipioni, P. Rischette, and J.-P. Préaux, "Pascal's triangle: An origin of Daubechies polynomials and an analytic expression for associated filter coefficients," *Signal Processing,* vol. 92, no. 1, pp. 276-280, 2012/01/01/ 2012.
[107] P. Abry, P. Flandrin, M. S. Taqqu, and D. Veitch, "Self-Similarity and Long-Range Dependence Through the Wavelet Lens," 2000.
[108] H. Wendt, P. Abry, and S. Jaffard, "Bootstrap for Empirical Multifractal Analysis," *Signal Processing Magazine, IEEE,* vol. 24, no. 4, pp. 38-48, 2007.
[109] R. F. Leonarduzzi, M. E. Torres, and P. Abry, "Scaling range automated selection for wavelet leader multifractal analysis," *Signal Processing,* vol. 105, pp. 243-257, 2014.
[110] E. Ihlen, "Introduction to Multifractal Detrended Fluctuation Analysis in Matlab," (in English), *Frontiers in Physiology,* Methods vol. 3, no. 141, 2012-June-04 2012.
[111] A. Pulkkinen, A. Viljanen, K. Pajunpää, and R. Pirjola, "Recordings and occurrence of geomagnetically induced currents in the Finnish natural gas pipeline network," *Journal of Applied Geophysics,* vol. 48, no. 4, pp. 219-231, 2001.
[112] A. Viljanen, A. Pulkkinen, R. Pirjola, K. Pajunpää, P. Posio, and A. Koistinen, "Recordings of geomagnetically induced currents and a nowcasting service of the Finnish natural gas pipeline system," *Space Weather,* vol. 4, no. 10, pp. n/a-n/a, 2006.
[113] H. Wendt and P. Abry, "Bootstrap for Multifractal Analysis," in *Acoustics, Speech and Signal Processing, 2006. ICASSP 2006 Proceedings. 2006 IEEE International Conference on*, 2006, vol. 3, pp. III-III.